

On ice mechanics in ice-induced vibrations

Owen, C.C.

DOI

[10.4233/uuid:b8954e95-15d9-430d-b026-71f4cf99ef23](https://doi.org/10.4233/uuid:b8954e95-15d9-430d-b026-71f4cf99ef23)

Publication date

2024

Document Version

Final published version

Citation (APA)

Owen, C. C. (2024). *On ice mechanics in ice-induced vibrations*. [Dissertation (TU Delft), Delft University of Technology]. <https://doi.org/10.4233/uuid:b8954e95-15d9-430d-b026-71f4cf99ef23>

Important note

To cite this publication, please use the final published version (if applicable).
Please check the document version above.

Copyright

Other than for strictly personal use, it is not permitted to download, forward or distribute the text or part of it, without the consent of the author(s) and/or copyright holder(s), unless the work is under an open content license such as Creative Commons.

Takedown policy

Please contact us and provide details if you believe this document breaches copyrights.
We will remove access to the work immediately and investigate your claim.

On ice mechanics in ice-induced vibrations

On ice mechanics in ice-induced vibrations

Dissertation

for the purpose of obtaining the degree of doctor
at Delft University of Technology
by the authority of the Rector Magnificus prof. dr. ir. T.H.J.J. van der Hagen;
Chair of the Board for Doctorates
to be defended publicly on
Monday 29 April 2024 at 15:00 o'clock

by

Cody Carlton OWEN

Master of Science in Offshore and Dredging Engineering, Delft University of Technology,
Netherlands

Master of Science in Wind Energy, Norwegian University of Science and Technology,
Norway

born in Southampton, New York, United States of America

This dissertation has been approved by the promotor.

Composition of the doctoral committee:

Rector Magnificus,	chairperson
Prof. dr. A.V. Metrikine,	Delft University of Technology, promotor
Dr. ir. H. Hendrikse,	Delft University of Technology, copromotor

Independent members:

Prof. dr. ir. E. Schlangen,	Delft University of Technology
Prof. dr. A. Bekker,	Stellenbosch University, South Africa
Dr. D.M. Cole,	US Army Corp of Engineers, United States of America
Prof. dr. K.V. Høyland,	Norwegian University of Science & Technology, Norway
Dr. A. Shestov,	University Centre in Svalbard, Norway
Prof. dr. ir. M.A.N. Hendriks,	Delft University of Technology, reserve member

This thesis was made possible by the participating organizations in the SHIVER project: Delft University of Technology, Siemens Gamesa Renewable Energy, and Aalto University. The SHIVER project is co-financed by Siemens Gamesa Renewable Energy and TKI-Energy by the 'Toeslag voor Topconsortia voor Kennis en Innovatie (TKI's)' of the Dutch Ministry of Economic Affairs and Climate Policy under grant reference TKITOE_WOZ_1906_TUD_SHIVER.



Keywords: dynamic ice-structure interaction, ice-induced vibrations, frequency lock-in, *c*-axis, interference coloration, ice microstructure, ice fabric, ice texture, image processing, birefringence, grain boundary, controlled oscillation, ice failure length, anelasticity, ice crushing, model tests, compliance effect, velocity effect

Printed by: Gildeprint - Enschede

Front & Back: Photograph of ice thin section in crossed-polarized light; Julia set plot with interference colors matching those of the ice thin section.

Copyright © 2024 by C.C. Owen

ISBN 978-94-6366-819-4

An electronic version of this dissertation is available at
<https://repository.tudelft.nl/>.

Antifragility is beyond resilience or robustness. The resilient resists shocks and stays the same; the antifragile gets better . . . The antifragile loves randomness and uncertainty, which also means—crucially—a love of errors, a certain class of errors.

Nassim Nicholas Taleb

CONTENTS

Summary	xi
Samenvatting	xiii
Preface	xvii
1 Introduction	1
1.1 Ice engineering in a capricious climate	1
1.2 Offshore wind in icy waters	2
1.3 The phenomenon of ice-induced vibrations	2
1.4 Offshore wind support structure design for ice-induced vibrations	6
1.5 Theories of ice-induced vibrations	7
1.5.1 Global failure length theory	8
1.5.2 Negative damping theory	10
1.5.3 Zonal approach to contact area variation	11
1.5.4 Contact area variation and rate-dependent local failure length theory	12
1.6 Knowledge gaps in the ice mechanics of ice-induced vibrations	14
1.7 Thesis objective and scope	15
1.8 Thesis outline	16
2 An initial study of interference coloration for quantifying the texture and fabric of ice	19
2.1 Introduction	20
2.2 Theory	21
2.2.1 Ice birefringence in linearly polarized light	21
2.2.2 Interference coloration of ice in crossed-polarized light	25
2.2.3 Effect of light source color temperature on interference coloration	28
2.2.4 Multi-level Voronoi tessellation for simulated ice fabrics	31
2.3 Methodology	32
2.3.1 Image registration	33
2.3.2 Grain boundary segmentation	34
2.3.3 Grain azimuth extinction and orientation of brightest color	35
2.3.4 Grain inclination angle	35
2.3.5 <i>ColorIce</i> MATLAB toolbox	35
2.4 Application	36
2.4.1 Validation against Rigsby stage technique	36
2.4.2 Laboratory-grown freshwater ice	37
2.4.3 IJsselmeer lake ice	37

2.5	Discussion	38
2.5.1	Rigsby stage technique	39
2.5.2	Limitations	40
2.5.3	Recommendations	42
2.6	Conclusion	43
2.A	Refractive indices for ice	43
3	Hysteresis and dichotomous mechanics in cyclic crushing failure of confined freshwater columnar ice	47
3.1	Introduction	48
3.2	Experimental setup and procedure	51
3.2.1	Ice preparation	51
3.2.2	Experimental setup	52
3.2.3	Experimental procedure and test matrix	54
3.2.4	Method of data post-processing	55
3.2.5	Impact of test setup on measurements	56
3.3	General observations from experiments	56
3.3.1	Load and motion signals	56
3.3.2	Videos	57
3.4	Results	59
3.4.1	Ice deformation and failure behavior during a crushing cycle	60
3.4.2	Effect of velocity on load peaks during a crushing cycle	61
3.4.3	Effect of velocity on critical deformation between fracture events	63
3.4.4	Effect of frequency and velocity on stress relaxation duration and peak load	63
3.4.5	Effect of deviation from haversine velocity waveform on load signal	64
3.5	Discussion	67
3.5.1	Effect of lack of test setup stiffness on results	68
3.5.2	Comparison to controlled-oscillation in model-scale ice tank tests	68
3.5.3	Reflection on literature and anelasticity of ice	68
3.5.4	Application to the frequency lock-in regime	71
3.6	Conclusion	72
4	Peak loads during dynamic ice-structure interaction caused by rapid ice strengthening at near-zero relative velocity	75
4.1	Introduction	76
4.2	Test campaign description	78
4.2.1	Test setup	78
4.2.2	Model ice	79
4.2.3	Tests included in the analysis	80
4.3	The load-velocity dependence from rigid structure tests	81
4.4	The peak load-velocity dependence from controlled-oscillation tests	83
4.5	The velocity and compliance effect during ice-induced vibrations	87
4.6	Discussion	89
4.6.1	The peak load-velocity dependence during penetration and ice-induced vibrations	89

4.6.2	Compliance and velocity effects in ice peak loads	90
4.6.3	Rapid strengthening at low relative velocity as a property of ice or model ice only	91
4.6.4	Comment on spalling as a mechanism for ice-induced vibrations	93
4.7	Conclusion	94
4.A	Experimental data from test campaign	94
5	Discussion and conclusion	99
5.1	Discussion	99
5.1.1	Contact processes at the ice-structure interface	99
5.1.2	Constitutive ice behavior	100
5.1.3	Ice fracture mechanics under compression	101
5.1.4	Ice damage and strengthening	101
5.1.5	Reflection on ice mechanics in ice modeling	102
5.2	Summary and conclusions	103
5.3	Outlook	105
	References	109
	Acknowledgements	129
	Curriculum Vitae	133
	List of Publications	135

SUMMARY

The imminence of anthropogenic climate change has motivated a global energy transition towards sustainable power generation. Offshore wind—an important contributor to the energy transition—is expanding, not only in turbine size and number of installations, but also into regions with harsher environmental conditions. One of those conditions in places such as the Baltic Sea is drift ice. Offshore wind turbine support structures, with vertical sides at the waterline, must be designed to survive dynamic ice-structure interaction when ice fails in crushing against the structure. For a safe and efficient design of the support structure, dynamic ice-structure interaction resulting in ice-induced vibrations must be considered. Therefore, both an understanding of the problem and accurate modeling for the prediction of the development of ice-induced vibrations are required.

Significant progress has been made in recent years on the topic of ice-induced vibrations, and a numerical model for prediction of ice-induced vibrations has been developed based on the principles of velocity-dependent deformation and failure behavior of ice, and contact area variation between ice and structure during interaction. However, uncertainty remains regarding physical mechanisms within the ice which govern ice-induced vibrations. The ice mechanics involved in the development of ice-induced vibrations is therefore the main topic of this thesis.

The main objective was to investigate and identify the ice mechanics involved in the development of ice-induced vibrations, especially in the regime of frequency lock-in as historically defined. It was hypothesized that dynamic recrystallization played a relevant role in the ice mechanics involved in ice-induced vibrations. To test the hypothesis, ice mechanics experiments were performed at the ice laboratory specifically developed at Delft University of Technology for this purpose.

To identify grain-scale mechanisms in ice, such as dynamic recrystallization, a method was devised to elucidate ice thin section textures and (quarter) fabrics by means of crossed-polarized transmitted light and interference coloration of ice. An attempt was made to apply the method to the laboratory experiments which applied compressive loading to the edge of a thin freshwater columnar-grained ice plate, laterally confined by glass plates. Crossed-polarized transmitted light was shone through the glass plates to observe the grain structure of the ice during cyclic compression with a haversine velocity waveform. The loading and confinement scenario was intended to reproduce a vertical section of the ice edge during frequency lock-in vibrations. The experimental design demonstrated that the grain-scale mechanics of dynamic recrystallization did not obviously contribute to the peak load-velocity relation associated with frequency lock-in vibrations. As expected, fracture initiated on the grain scale was responsible for load drops. But, more interestingly, stress relaxation during periods of low relative velocity between ice and structure occurred rapidly. Following the stress relaxation, when velocity

increased, the peak load was higher than previous brittle peak loads. The results indicated that the mechanisms involved in the stress relaxation were occurring on a scale smaller than the grain size. A loading path dependency was also observed with respect to the peak load-velocity relation.

Ice penetration experiments at the Aalto Ice and Wave Tank in ethanol-doped cold model ice were performed with a rigid structure, controlled oscillation, and a single-degree-of-freedom structure, and comparison of results showed that the peak global ice loads depended on the amount of time spent at low relative velocities where an ice strengthening effect developed. This has implications for the so-called velocity effect and compliance effect in design of structures subject to dynamic ice-structure interaction.

Overall, the load signals from the ice mechanics experiments on freshwater ice resembled the load signals obtained from the controlled-oscillation experiments from the model-scale ice tank tests. The qualitatively similar velocity and resulting load patterns give confidence in the idea that the mechanisms involved in both types of experiments were similar, even for different ice types and loading scenarios.

These similar results demonstrate a link in the ice mechanics across different ice types and loading scenarios, which may be explained with further research on path-dependent constitutive ice behavior, and with scrutiny regarding ice dislocation and grain boundary mechanics. Suggestions for future research are proposed, including the testing of strain-rate-varying uniaxial compression of ice and ice penetration experiments with haversine velocity waveforms.

SAMENVATTING

De naderende dreiging van door mensen veroorzaakte klimaatverandering heeft de wereldwijde energietransitie naar duurzame stroomopwekking gestimuleerd. Offshore windenergie, een belangrijke bijdrager aan deze energietransitie, breidt zich uit, niet alleen wat betreft turbinegrootte en het aantal installaties, maar ook naar gebieden met zwaardere omgevingscondities. Een van die omstandigheden, zoals in de Baltische Zee, is drijfijis. Draagconstructies voor offshore windturbines, met verticale zijden op de waterlijn, moeten ontworpen worden om de dynamische interacties tussen het ijs en de constructie te weerstaan wanneer het ijs bezwijkt als het tegen de constructie wordt samengedrukt. Voor een veilig en efficiënt ontwerp van de draagconstructie moet deze dynamische interactie die kan leiden tot trillingen in de constructie worden meegenomen. Daarom is zowel begrip van het probleem, als de nauwkeurige modellering voor het voorspellen van de ontwikkeling van door ijs veroorzaakte trillingen noodzakelijk.

Er is de afgelopen jaren aanzienlijke vooruitgang geboekt op het gebied van door ijs veroorzaakte trillingen en er is een numeriek model ontwikkeld voor het voorspellen van deze trillingen op basis van de snelheidsafhankelijke vervorming en bezwijkmechanismen van ijs en het wisselende contactoppervlak tussen het ijs en de constructie tijdens de interactie. Er blijft echter onzekerheid bestaan over de leidende fysische mechanismen in het ijs die van belang zijn voor het ontwikkelen van door ijs veroorzaakte trillingen. Het hoofdonderwerp van dit proefschrift is daarom de ijsmechanica die belangrijk is voor de ontwikkeling van deze trillingen.

Het hoofddoel was om de ijsmechanica te identificeren en te onderzoeken die betrokken is bij de ontwikkeling van door ijs veroorzaakte trillingen, vooral in het regime van frequentie lock-in zoals dat historisch gedefinieerd is. De hypothese was dat dynamische herkristallisatie van het ijs een relevante rol speelde in de ijsmechanica die betrokken is bij door ijs veroorzaakte trillingen. Om deze hypothese te toetsen werden ijsmechanica-experimenten uitgevoerd in een ijslaboratorium. Dit laboratorium was voor dit doel ontwikkelend op Technische Universiteit Delft.

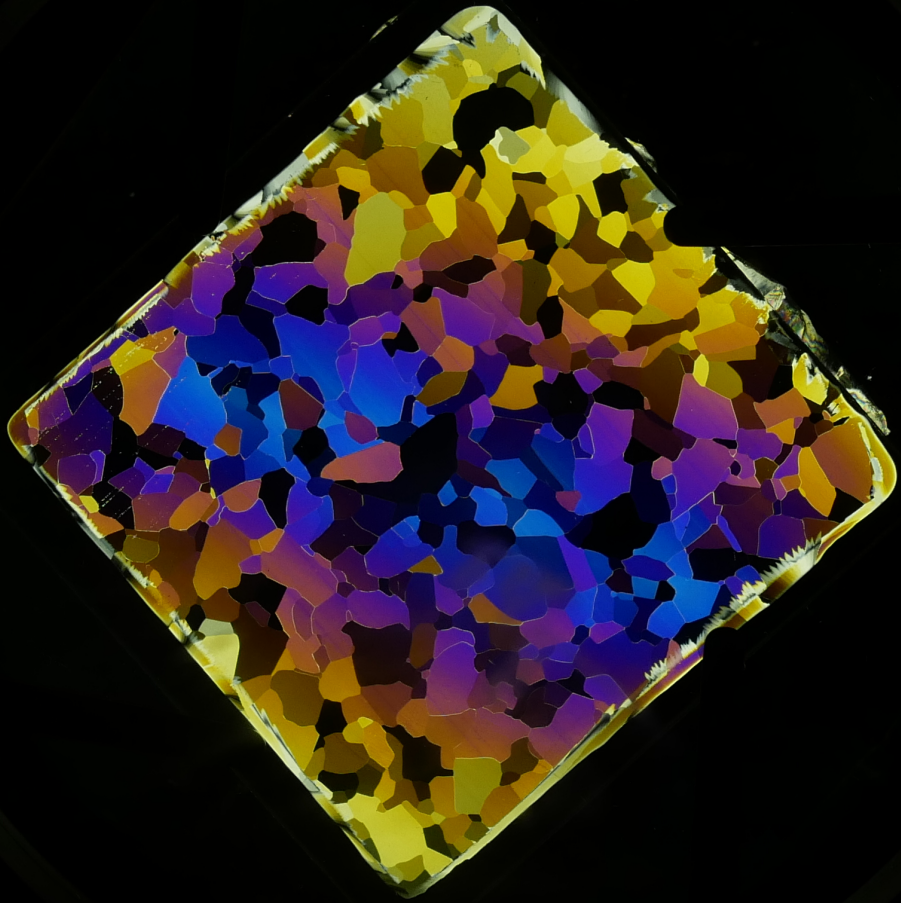
Om op korrelniveau mechanismen in ijs zoals dynamische herkristallisatie te kunnen onderscheiden is een methode ontwikkeld die met behulp van gekruist gepolariseerd licht en interferentiekleurings in dunne ijssecties textuur en structuur te verduidelijken. De methode is toegepast in een laboratoriumexperiment waarbij een ijsplaat van zoetwater met kolomvormige korrelstructuur aan een zijde op druk werd belast. De ijsplaat bevindt zich tussen glasplaten, waardoor het gepolariseerde licht geschenen werd. Hierdoor kon de korrelstructuur van het ijs geobserveerd worden terwijl het proefstuk cyclisch werd belast door een haversinusvormige snelheidsgolf. De belasting en begrenzing van het proefstuk was dusdanige gekozen om in een verticale ijsrand trillingen tijdens frequentie lock-in te produceren. Het experimentele data toonde aan dat de dynamische herkristallisatie niet duidelijk bijdroeg aan de piekbelasting-snelheidsrelatie die geassocieerd werd met

ijstrillingen tijdens frequentie lock-in. Zoals verwacht leidde scheuren op de korrelschaal tot plotselinge belastingdalingen. Interessanter was de observatie dat tijdens periodes met een lage relatieve snelheid tussen ijs en constructie een snelle spanningsrelaxatie optrad. Wanneer daarna de snelheid weer toenam, was de piekbelasting hoger dan de vorige broze piekbelastingen. De resultaten gaven aan dat de mechanismen achter de spanningsrelaxatie plaatsvonden op een schaal kleiner dan de korrelgrootte. Ook werd er waargenomen dat de piekbelasting-snelheidsrelatie afhangt van het belastingspad.

In de Aalto Ice and Wave Tank werden ijspenetratie-experimenten uitgevoerd met ethanol-gedoteerd koud modelijs. Hierin werd de interactie tussen het ijs en een starre structuur, gecontroleerde oscillaties en een constructie met een enkele vrijheidsgraad getest. De vergelijking van de resultaten toonde aan dat de globale piekbelasting van het ijs afhing van duur van perioden met lage relatieve snelheden waarin een ijsversterkend effect ontstond. Dit heeft gevolgen voor het zogenaamde snelheidseffect en het compliance-effect voor het ontwerpen van constructie die onderhevig zijn aan dynamische ijs-structuurinteractie.

Over het algemeen leken de belastingsignalen van de ijsmechanica-experimenten met zoetwaterijs op de belastingsignalen die werden verkregen uit de gecontroleerde oscillatie-experimenten in de ijsbekkenproeven op modelschaal. De kwalitatief vergelijkbare snelheids- en resulterende belastingspatronen onderbouwen het idee dat onderliggende mechanismen tijdens beide soorten experimenten vergelijkbaar waren, zelfs voor verschillende ijsoorten en belastingsscenario's.

Deze vergelijkbare resultaten tonen dat er een verband bestaat in de ijsmechanica voor verschillende ijsoorten en belastingsscenario's. Dit zou verklaard kunnen worden door middel van verder onderzoek naar het padsafhankelijk constitutief gedrag van ijs en met nauwkeuriger onderzoek naar ijsdislocaties en korrelgrensmechanica. Richtingen voor toekomstig onderzoek worden voorgesteld, waaronder het testen van ijs onder rekssnelheidsvariërende enkelassige drukbelasting en ijspenetratie-experimenten met haversinusvormige snelheidsgolven.

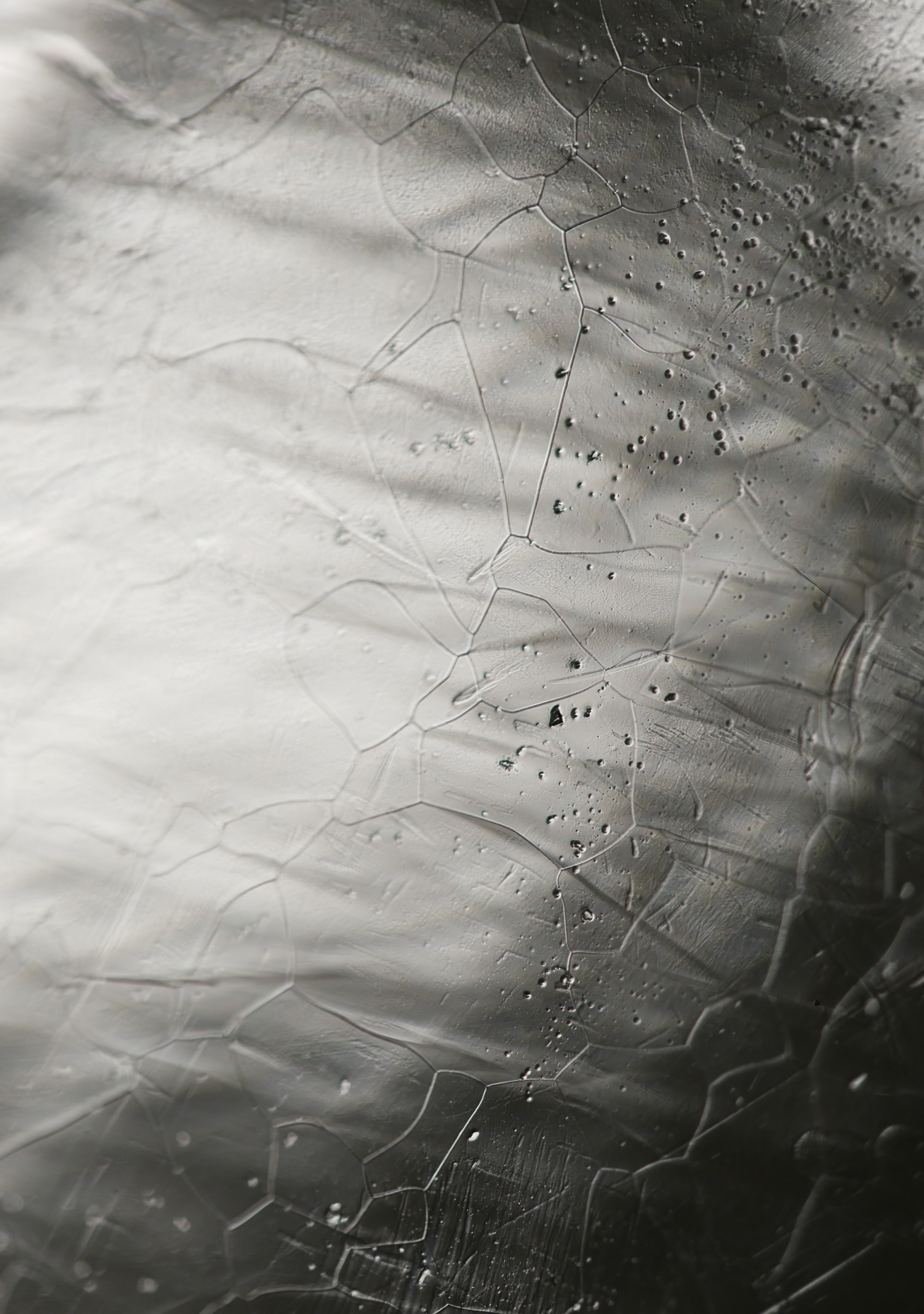


PREFACE

Serendipity, and the preparation for such, were the key to the findings presented in this thesis. Much of my time in the first two years of the PhD was spent stumbling around in the literature, grasping at concepts and topics which would require a PhD in themselves to properly understand and synthesize. Hayo and I had submitted a manuscript to *Cold Regions Science and Technology* which consisted of an exhaustive literature review and formulation of a hypothesis built on speculation. The manuscript was assigned re-submission after *major* revision. The criticism fatal to the survival of the manuscript was this: where are the experiments to test this hypothesis? We decided to withdraw the manuscript and focus our attention and energy on designing a test setup capable of testing the hypothesis. Roughly one year and thousands of euros later, a eureka moment was had! Surprisingly, it was, for lack of a better word, the *wrong* eureka! The hypothesis, at least with the test setup we had, was ostensibly falsified. Instead, we observed something else entirely. And to our disbelief, the observations were undeniably similar to those from the ice tank experiments of the SHIVER project. We found a common theme across ice types and interaction scenarios, a theme worth pursuing in the hope of making a more fundamental description of ice mechanics in ice-induced vibrations.

I wish there was more to say, but my contract ended, as did my residence and work permit, and there was only time to tie up loose ends. Perhaps my postdoctoral research will shed further light on the viscosity of ice, or maybe Tim and Hayo will unlock the next door to predicting ice-induced vibrations with ice property measurements. Or, hopefully, other researchers beyond TU Delft will continue this theme and find answers to our questions.

*Cody Carlton Owen
Delft, March 2024*



1

INTRODUCTION

1.1. ICE ENGINEERING IN A CAPRICIOUS CLIMATE

In 2019, the atmospheric concentration of carbon dioxide—the principle anthropogenic greenhouse gas—was higher than at any time in the last two million years (IPCC, 2023). The rate of global surface temperature increase has been higher since 1970 than in any fifty-year period in the last two thousand years. As for the Arctic, two especially striking trends have been observed (Pörtner *et al.*, 2019). First, since 1979, the areal proportion of multi-year sea ice has declined by approximately 90 %, indicating younger and thinner ice cover. Second, also since 1979, the Arctic sea ice extent has declined in every month of the year, and the decadal decrease in September has shown a trend which has not been observed in the last thousand years. Similarly, in the subarctic zone or regions with annual ice cover, ice conditions have become milder over the last century. This trend has been observed in, for example, the Baltic Sea (Jevrejeva *et al.*, 2004; Tikanmäki and Heinonen, 2022; Vihma and Haapala, 2009), Great Lakes of North America (Ozersky *et al.*, 2021), and Bohai Sea to some degree (Yan *et al.*, 2020).

Although milder winters in regions with ice cover could bode well for shipping and for design of offshore structures, context is needed. While the winters on average may become milder, past and future severe winters should not be disregarded from extreme value analysis in design—especially regarding extreme ice thickness and extent—even with confidence in near-centennial trends (e.g. Haapala *et al.*, 2015; Tikanmäki and Heinonen, 2022). Specifically, there is not yet evidence of absence, but only absence of evidence, of extreme winter events due to climate change. In other words, few or no severe winters in the last 30 years does not lower the risk of a severe winter in the next 30 years, particularly within a changing climate system. Moreover, anthropogenic climate change has been weakening the Atlantic Meridional Overturning Circulation (AMOC) (Pörtner *et al.*, 2019). Disruption or collapse of the AMOC, although very unlikely, would lead to devaluation of historical records of ice conditions in places such as the Baltic Sea due to radical, abrupt changes in the climate in the North Atlantic region (Ditlevsen and Ditlevsen, 2023; Jackson *et al.*, 2015).

To conclude, the increase in atmospheric carbon dioxide, and consequently the increase in global surface temperatures, do not necessarily lead to less relevance on the topic of ice or cold regions engineering. Counterintuitively, milder winters, notwithstand-

ing the possibility of extreme events, attract greater interest in wintertime Arctic and subarctic shipping, fishing, and hydrocarbon exploration (IPCC, 2023). These activities increase exposure of offshore structures to interactions with the ice cover.

1.2. OFFSHORE WIND IN ICY WATERS

Anthropogenic climate change and the potential, severe, irreversible consequences therefrom, termed the climate crisis, pose one of the greatest threats to human civilization in the 21st century. A substantial reduction in industrial carbon emissions offers a clear and tenable solution to the climate crisis (IPCC, 2023). The transition in large-scale electrical energy production from conventional fossil fuels, such as oil and coal, to more sustainable sources provides a means to combat the climate crisis in a manner compatible with the current economic system. Offshore wind energy, since the installation of the Vindeby Offshore Wind Farm in 1991, has been demonstrated to be a major player in the diverse energy portfolio required for a swift and economical energy transition.

To meet growing energy demands in a sustainable manner, eight countries bordering the Baltic Sea have planned to increase installed offshore wind capacity from about 2.8 GW today to 19.6 GW by 2030 (WindEurope, 2022). A significant portion of the Baltic Sea freezes during the winter months, with spring ice breakup leading to large quantities of mobile drift ice. Bottom-founded, or fixed, offshore wind support structures designed for the Baltic Sea or other freezing areas must be able to survive ice actions from the drift ice over their lifetimes (see Figure 1.1). When an ice floe is driven by wind and current into a vertically-sided structure, the ice can act on the structure and exert ice-induced loads with various characteristics. The scope of this thesis considers only level ice deforming and failing in in-plane creep and crushing against a vertically-sided structure. The reader is referred to Hendrikse (2017) for broader information on ice actions, ice features, and ice failure modes in the context of vertically-sided structures.

When level ice crushes against a vertically-sided structure at the waterline, termed the ice action point, dynamic interaction between the ice and structure may occur. With sufficient compliance at the ice action point, and sufficient ice-induced loads, ice-induced vibrations (IIV) of the structure may develop. Although the motivation for and application of this thesis is fixed offshore wind support structures, the theme of dynamic ice-structure interaction resulting in ice-induced vibrations extends to all types of offshore structures provided there is sufficient compliance at the ice action point. These ice-induced vibrations can result in high ice-induced global peak loads, severe structural response, and significant fatigue over the lifetime of an offshore structure. Therefore, it is important to predict whether a structure is susceptible to ice-induced vibrations under certain ice conditions. But first, ice-induced vibrations are defined based on the observed characteristics from full-scale and laboratory measurements.

1.3. THE PHENOMENON OF ICE-INDUCED VIBRATIONS

To describe ice-induced vibrations, it is best to first consider a scenario in which ice acts on a structure that is rigid: ideally, immovable and nondeformable; practically, very stiff relative to the applied force. For ice action on a rigid structure, two ice failure modes



Figure 1.1: Photograph, courtesy of Siemens Gamesa Renewable Energy, of the offshore wind turbines at the Danish Nissum Bredning site in the winter of 2018 (Hendrikse and Koot, 2019).

can develop: creep and crushing. At very low ice drift speeds, the ice deforms and fails in global creep—also called ductile failure—which refers to the plastic deformation and flow of the ice around the structure (Hendrikse and Nord, 2019). Relatively uniform pressures and full contact tend to develop at the ice-structure interface (Määttänen *et al.*, 2011; Sodhi, 2001; Takeuchi *et al.*, 2001). The global ice-induced load time history in creep is typically characterized by an increase at initial contact between ice and structure, followed approximately by a plateau once contact area maximizes (Hendrikse *et al.*, 2022a; Määttänen *et al.*, 2011; Michel and Toussaint, 1977; Sodhi, 1991a; Sodhi *et al.*, 1998; Takeuchi *et al.*, 2001). At higher ice drift speeds, ice fails against a structure in crushing which entails ice under compression, at and near the ice-structure interface, which deforms and fails in a brittle manner. The ice fractures, pulverizes, and is extruded upward and downward from the ice-structure interface, typically resulting in a pile of ice fragments of various sizes near the structure on the upper surface of the ice sheet (Hendrikse *et al.*, 2018; Jordaan, 2001; Matsushita *et al.*, 2000; Muhonen *et al.*, 1992; Sodhi, 2001; Timco, 1987). Contact area at the ice-structure interface tends to be lower in crushing than in creep (Takeuchi *et al.*, 2001), and generally concentrated with highest pressures in a fluctuating line-like contact along the horizontal center-line of the ice sheet (Hendrikse and Metrikine, 2016; Sodhi, 2001; Takeuchi *et al.*, 2001; Ziemer, 2021). In crushing, the local pressures are non-uniform and vary spatiotemporally (Taylor *et al.*, 2019). The global ice-induced load time history in crushing is typically characterized by quasi-random fluctuations about a mean load as a consequence of the sum of local ice pressures and failures at the ice-structure interface.

By introducing a compliant, or flexible, structure, the potential for ice-induced vibrations arises. For very low ice drift speeds, the ice fails in creep in a similar manner as that for a rigid structure and no dynamic interaction develops. However, for ice drift speeds causing failure of ice in crushing, distinct regimes of ice-induced vibrations can develop. For a structure with a single dominant mode, a single-degree-of-freedom (SDOF) model is representative and leads to three potential regimes of ice-induced vibrations (see Figure 1.2). At the lowest ice speeds above those causing creep, the regime of intermittent crushing (ICR) develops for all flexible structures. Above the speeds for intermittent crushing, a regime called frequency lock-in (FLI) may or may not develop, depending on the structural properties and ice-induced loads of the interaction scenario. Finally, for the highest ice speeds, the regime of continuous brittle crushing (CBR) manifests, and is present for all flexible structures.

As shown in Figure 1.2a, the intermittent crushing regime of ice-induced vibrations has been characterized by sawtooth-like global ice-induced load and structural displacement time histories at the ice action point and has been known to develop at low ice drift speeds (Hammer *et al.*, 2023; Hendrikse *et al.*, 2022a; Hendrikse and Nord, 2019; Owen and Hendrikse, 2019). The frequency of this sawtooth is relatively constant under steady ice conditions (i.e. constant ice thickness, strength, and drift speed) and is lower than the first natural frequency for a given structure. The sawtooth frequency increases with increasing ice drift speed until another regime of ice-induced vibrations dominates the interaction. Intermittent crushing can be referred to as quasi-static because the structural displacement amplitude is mainly a function of the ratio between the global ice load and the structural stiffness at the ice action point. However, the dynamic properties of

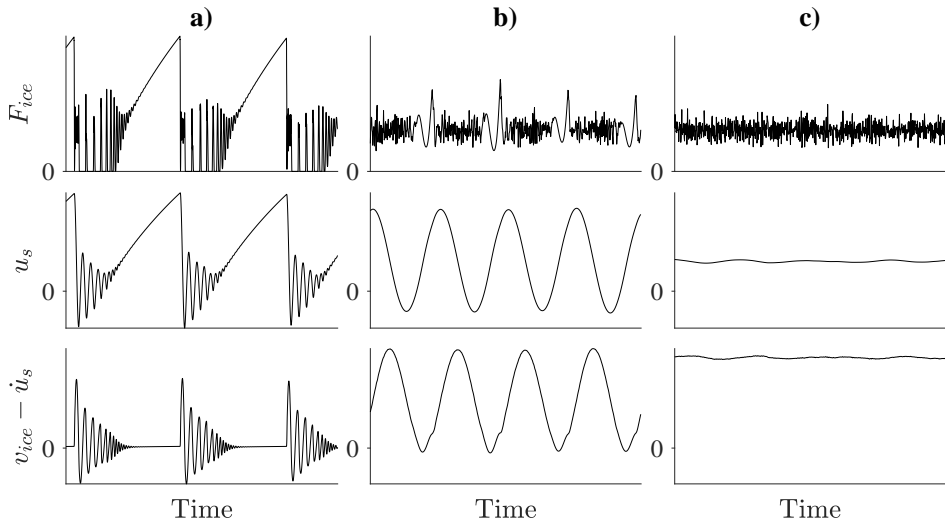


Figure 1.2: Illustration of simulated time histories depicting the global ice load F_{ice} , structural displacement at the ice action point u_s , and relative velocity between ice drift and structure at the ice action point $v_{ice} - \dot{u}_s$ during ice-induced vibrations of a single-degree-of-freedom (SDOF) model representation of a structure: **a)** intermittent crushing; **b)** frequency lock-in; and **c)** continuous brittle crushing.

the structure contribute to the transient structural response after moments of global ice failure (Nord *et al.*, 2015). Global ice failure, deemed simultaneous failure, associated with the load drops is the result of cascading brittle failure of the ice edge (Hendrikse and Metrikine, 2016; Ziemer, 2021). During the build-up phase of intermittent crushing, small-scale experiments in model ice demonstrated an increase in contact area between the ice and structure, as well as an increase in pressure to some extent (Hendrikse and Metrikine, 2015; Nord *et al.*, 2015; Ziemer, 2021).

As shown in Figure 1.2b, the frequency lock-in regime of ice-induced vibrations has been characterized by a quasi-sinusoidal structural displacement time history at or slightly below one of the natural frequencies of the structure at the ice action point and has been known to develop at intermediate ice drift speeds for structures with low damping (Hendrikse and Nord, 2019; Hendrikse *et al.*, 2018; Owen and Hendrikse, 2018; Owen and Hendrikse, 2019; van den Berg *et al.*, 2022; Ziemer and Hinse, 2017). During frequency lock-in, the structural response is nearly harmonic with an exception at the moment when the relative velocity between ice and structure begins to increase. The ice momentarily inhibits the structure from returning to its equilibrium position until the ice fractures significantly. As a result of this interaction, the global ice load appears quasi-periodic with two distinct intervals: highly irregular during high relative velocity due to brittle ice crushing and more regular at low relative velocity. The greater regularity in the ice load signal during low relative velocity is associated with non-brittle ice behavior, and a rapid increase in global ice load typically occurs following the moment of low relative velocity. Often, the global ice load decreases at negative relative velocity due to

the structure moving faster than—and therefore away from—the ice.

As shown in Figure 1.2c, the continuous brittle crushing regime of ice-induced vibrations has been characterized by 1) a stochastic global ice-induced load time history which varies about a mean value when in uniform ice conditions; and 2) a structural displacement time history typical of a structure excited by an aperiodic load, and has been known to develop at high ice drift speeds for all structures (Hendrikse and Nord, 2019; Hendrikse *et al.*, 2018; Owen and Hendrikse, 2019; van den Berg *et al.*, 2022). The aperiodic global ice load can be associated with the sum of spatiotemporal fluctuations of high-pressure zones with short durations across the ice-structure interface during interaction (Kamesaki *et al.*, 1996; Sodhi, 2001; Sodhi *et al.*, 1998). Compared to intermittent crushing and frequency lock-in, continuous brittle crushing exhibits a lower maximum global ice load and structural response amplitude, which indicates weaker dynamic ice-structure interaction.

For flexible structures—such as an offshore wind turbine—which have multiple modes of low damping and large mode shape amplitudes at the ice action point, a multi-degree-of-freedom (MDOF) model is then representative. More than the previous three regimes of ice-induced vibrations can develop for an MDOF structure. Mainly, between ice speeds for intermittent crushing and continuous brittle crushing, regimes called multi-modal interaction (MMI) with specific combinations of modes can develop (Hammer *et al.*, 2022; Hendrikse, 2017; Kärnä *et al.*, 2010). The development of the regimes for an MDOF structure are dependent on the properties of the modes at the ice action point, which means that the regimes for a MDOF structure cannot be generalized further. Figure 1.3 summarizes the dependence of ice action and ice-structure interaction on ice drift speed for rigid and flexible structures.

1.4. OFFSHORE WIND SUPPORT STRUCTURE DESIGN FOR ICE-INDUCED VIBRATIONS

It is imperative to accurately predict the development of ice-induced vibrations of offshore structures, and especially of offshore wind turbines, for which designs must be both safe and rigorously economical. Thus far, ice-induced vibrations of the support structure of an offshore wind turbine have yet to be measured, mainly due to recent mild winters (no or trivial ice formation) at the sites where offshore wind turbines have been installed. The absence of full-scale measurements commits design of offshore wind support structures in regions with drift ice to numerical simulations to meet design standards for certification (e.g. Hendrikse, 2019; IEC 61400-3-1, 2019; ISO 19906, 2019). Ideally, numerical simulations would be founded on a model or theory which comports with all or most of the empirical evidence available on ice-induced vibrations. But, as discussed in the next section, only empirical or phenomenological theories and their respective models have been developed to simulate the development of ice-induced vibrations of vertically-sided offshore structures. These phenomenological models require reference measurements for calibration; the manner in which physical ice properties are lumped into the reference measurements may limit the range of applicability of the models, especially in ice conditions which contrast significantly from experience. In summary, a theory and model that captures the main physical processes or mechanisms

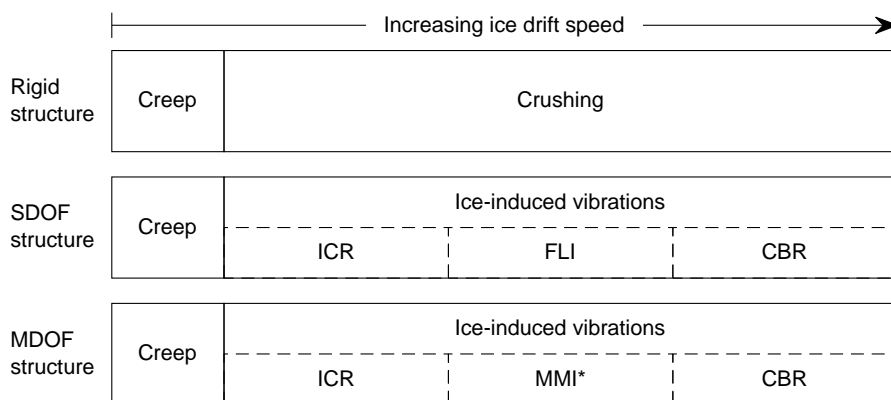


Figure 1.3: The regimes of ice action and ice-structure interaction for level ice acting against a vertically-sided structure. For a single-degree-of-freedom (SDOF) model of a structure, the regimes of intermittent crushing (ICR), frequency lock-in (FLI), and continuous brittle crushing (CBR) can develop. For a multi-degree-of-freedom (MDOF) model of a structure, the regime of frequency lock-in is instead replaced by the regime of multi-modal interaction (MMI). *FLI is subsumed under MMI for a MDOF model.

observed would grant accurate prediction of the development of ice-induced vibrations of offshore wind turbines in any set of ice conditions and without the need for full-scale measurements. Such a theory or model remains to be seen as explained next.

1.5. THEORIES OF ICE-INDUCED VIBRATIONS

Historically, the investigation of the theory of ice-induced vibrations has been motivated by engineering applications. Ice-induced vibrations of offshore structures resulting in serviceability issues or even catastrophic failure prompted research with the specific intent of producing a method for predicting these events (Björk, 1981; Blenkarn, 1970; Engelbrekton, 1977; Jefferies and Wright, 1988; Määttänen, 1975; Peyton, 1968; Schwarz and Jochmann, 2001; Yue and Bi, 2000; Yue *et al.*, 2001). To summarize this history, a concise timeline of the developments of ice-induced vibrations in terms of major observations, theories, experimental campaigns, and models is presented in Figure 1.4. Research motivation has primarily originated from hydrocarbon exploration and extraction, and from non-conservative design of navigational aids in ice-infested regions. But, in the last decade or so, offshore wind developments in the Baltic Sea have invigorated investigation into the topic of ice-induced vibrations. Although several theories and predictive models have been developed, contention has remained and meager progress has been made over the decades regarding identification of a physics-based theory for the development of ice-induced vibrations (Määttänen, 1988; Sodhi, 1988) with few exceptions (e.g. Gagnon, 1999). Instead, phenomenological models have been created and demonstrated to have limited applicability (Jeong and Baddour, 2010; Kärnä *et al.*, 2013; Muhonen, 1996).

Moreover, prediction formulae for the development of ice-induced vibrations have been attempted, but none can accurately predict the regimes of ice-induced vibrations given any realistic set of ice conditions and structure properties (Guo, 2013; Huang *et al.*, 2007; Izumiyama and Uto, 1997; Kamesaki *et al.*, 1996; Määttänen, 2008; Owen and Hendrikse, 2019; Palmer *et al.*, 2010; Yap and Palmer, 2013; Ziemer and Hinse, 2017).

Generally, theoretical and modeling developments have stemmed primarily from the failure length and the negative damping conceptions of ice-induced vibrations, which are addressed below. Models, based on these theories, have been refined and expanded to include zonal contact approaches and combinations of failure length and negative damping, although fundamentally the theories have remained unchanged. The recent development of the theory of contact area variation as the governing mechanism of ice-induced vibrations has sought to combine the observations of ductile-to-brittle transitional ice deformation and local failure length behavior with the ice speed dependence of local and global ice-induced loads in a phenomenological manner (Hendrikse and Metrikine, 2015). However, limitations—or even contradictions—in the predictive capabilities of all existing theories and their models highlight the key principle that is missing: the main physical mechanisms governing ice-induced vibrations.

Various advanced numerical modeling techniques, such as continuum, discrete, lattice, and cohesive element methods, have been implemented in an attempt to capture the complexities of dynamic ice-structure interaction (e.g. Kuutti and Kolari, 2013; Turner, 2018; Weiss and Dansereau, 2017; Xu *et al.*, 2019a; Zhang *et al.*, 2019). However, these methods circumvent physical mechanisms by modeling the ice as a medium with bulk behavior or as discrete and cohesive elements that may not be representative of physical observations of ice deformation and failure behavior (e.g. Gribanov *et al.*, 2018; Xu *et al.*, 2019b). Although these modeling techniques simulate greater levels of complexity in the dynamic ice-structure interaction problem, they do not address the physical mechanisms governing ice-induced vibrations and are therefore not treated here. Next, the various theories of ice-induced vibrations are addressed.

1.5.1. GLOBAL FAILURE LENGTH THEORY

The global or characteristic failure length theory of ice-induced vibrations entails structural resonance and employs a constant, discrete distance of ice that is crushed and expelled from the ice-structure interface during a typical loading cycle, which is most commonly associated with intermittent crushing (Matlock *et al.*, 1969; Palmer *et al.*, 2010; Peyton, 1968; Riska *et al.*, 1993). A constant effective pressure attributed to a constant area also meets this definition since the load needed to crush and expel the ice is then defined by the structural deflection (Neill, 1976; Sodhi, 1995). This theory typically divides the mechanism into a loading phase, then an unloading phase, and then sometimes a separation phase. The loading phase simulates low relative ice-structure velocity interaction that is characterized by a gradual global load increase and observed cracking in the ice sheet (Muhonen *et al.*, 1992; Nakazawa and Sodhi, 1990; Sodhi, 2001). The unloading phase simulates the rapid decrease in global load accompanied by pulverization and expulsion of crushed ice from the ice-structure interface as the deflected structure rebounds toward its equilibrium position. The separation phase refers to the period during which the structure and the ice sheet are not in contact as a result of either the transient

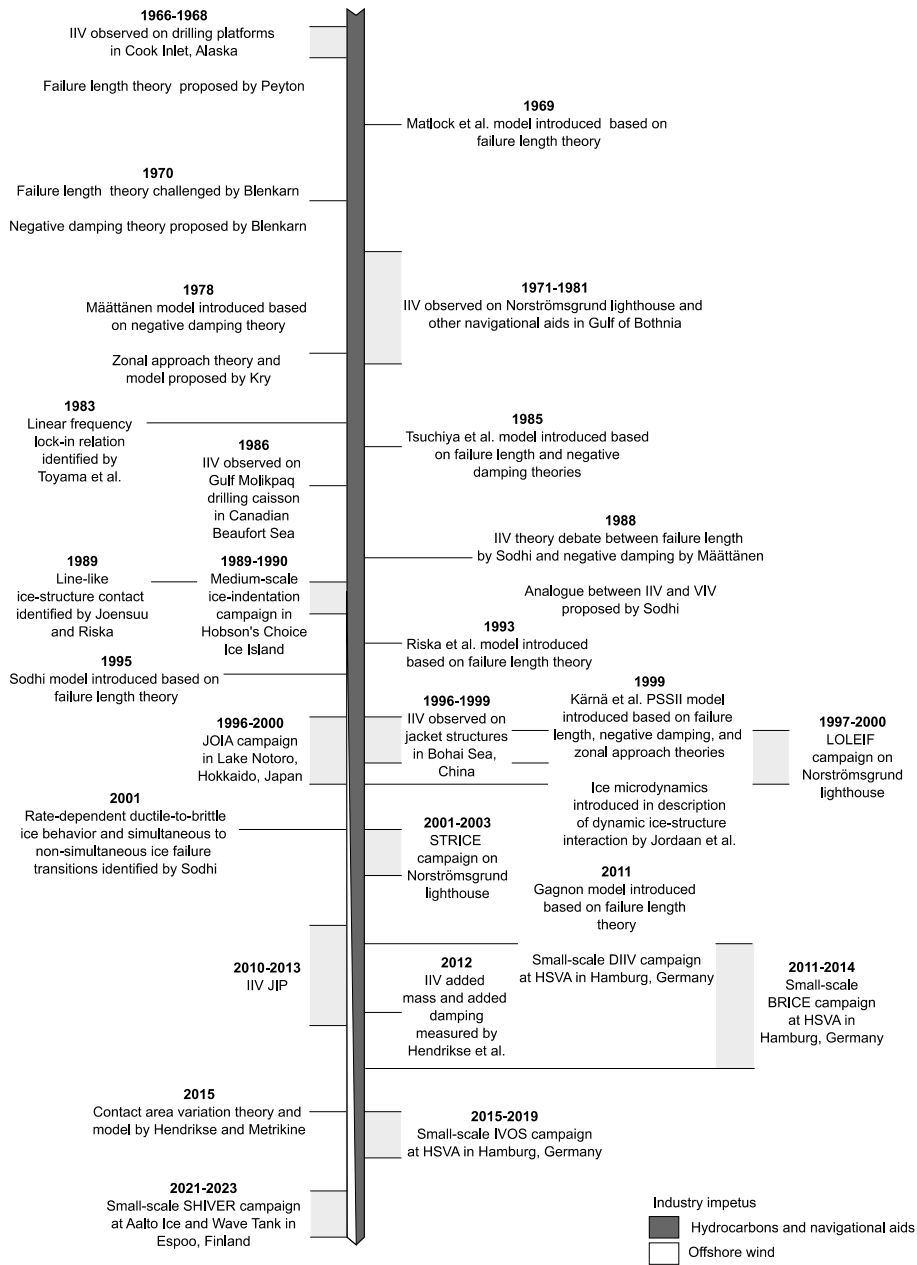


Figure 1.4: Timeline of key observational, theoretical, experimental, and model developments of ice-induced vibrations (IIV), 1966-2023.

vibrations of the structure induced by the rapid load drop or large spalling and flaking failure that ejected a very large portion of the ice sheet from the interface.

The theory of periodic, symmetric global spallation or flaking has been offered as a physical mechanism for development of ice-induced vibrations based on small- and medium-scale experiments (Gagnon, 2012; Kamesaki *et al.*, 1997; Kärnä and Järvinen, 1999). Reduction of contact due to ice flaking can explain global load drops during intermittent crushing, but such fracture events only provide a load-limiting mechanism under the assumption of purely brittle-elastic ice deformation and failure behavior. Contrarily, it has been observed in medium-scale indentation experiments that the ice sheet in close proximity to the ice-structure interface can undergo plastic deformation while the near-field ice sheet experiences elastic strains (Sakai *et al.*, 1998). Moreover, this theory does not explain the transition from simultaneous to non-simultaneous failure of ice with increasing ice drift speeds as observed in small- and medium-scale experiments (Saeki *et al.*, 1998; Sodhi, 1998; Sodhi *et al.*, 1998).

It has been suggested that the kinetic friction of the ice against the structure decreases with increasing interaction speed in a manner similar to the observed negative gradient of uniaxial compressive strength (Kärnä and Järvinen, 1999; Saeki *et al.*, 1986). A stick-slip friction mechanism is proposed to explain the development of a stagnation zone near the centerline of the ice-structure depending on ice drift speed (Shkhinek, 2010). This theory of velocity-dependent kinetic friction at the ice-structure interface, combined with symmetric or asymmetric flaking and comminution, compaction, and sintering at the interface, likely contributes to ice-induced vibrations by assisting in the development of high-pressure zones (Dempsey *et al.*, 2001; Jordaan, 2001; Sodhi, 2001). Note that the stagnation and high-pressure zones are effectively synonymous in this case.

It is emphasized that the sudden forward movements of a structure into a drifting ice sheet associated with intermittent crushing are caused not by the ice solely but by the deflected structure returning to equilibrium via crushing of the ice. In other words, cascading brittle failure of the ice sheet and elastic deflection of the structure, even on the order of millimeters for stiff structures, cause the sudden, cyclic compressive failure of ice sheets observed on all scales (Gagnon, 1999). Thus, cyclic compressive failure of ice in ice-induced vibrations is not caused by the ice alone, but by the interaction (Kärnä, 2011b; Kärnä and Järvinen, 1999). In the case of an effectually immovable and undeformable structure, global cyclic ice failure resulting in sawtooth-like global load patterns do not occur (Sodhi *et al.*, 1998; Takeuchi and Saeki, 1995), meaning that a characteristic crushing length is unequivocally defined by both the structural stiffness and by the ice properties, and is not solely a property of the ice. Dynamic ice-structure interaction models which rely on a characteristic global failure length (Ji and Oterkus, 2016; Ye *et al.*, 2019) 1) preclude the universally observed transition from simultaneous to non-simultaneous failure of ice during interaction; and 2) conventionally implement a constant characteristic failure length of ice derived from observations where the dynamic interaction undeniably affects this apparent failure length.

1.5.2. NEGATIVE DAMPING THEORY

The negative damping theory of ice-induced vibrations considers structural self-excitation, relies on the observed uniaxial compressive crushing strength of ice generally decreasing

with increasing stress rate¹, and assumes a continuous state of failure of the ice (Blenkarn, 1970; Kärnä *et al.*, 1999; Määttänen, 1988). Ice-structure interaction models have also been developed which define a characteristic failure length in combination with a source of negative damping stemming from rate-dependent ice strength, thereby manifesting as a speed-dependent global crushing length (Eranti *et al.*, 1981; Wu and Qiu, 2019). The ice crushing strength trend is determined from uniaxial compressive strength tests (Michel and Toussaint, 1977), which do not specifically resemble the stress states, deformation behavior, and failure mechanisms occurring at the ice-structure interface and inside the ice during dynamic interaction.

Moreover, the negative gradient of stress rate is not universally observed in uniaxial compressive strength tests for the range of strain rates and temperatures typical of dynamic ice-structure interaction (Jones, 1997; Jones, 2007; Schulson and Duval, 2009; Shazly *et al.*, 2009; Shkhinek, 2010; Sopper, 2016; Timco and Sudom, 2013; Wu *et al.*, 1976). Temperature has a strong effect on the uniaxial compressive strength trend but is not typically considered in negative damping modeling (Hendrikse and Metrikine, 2015). Numerical studies using a self-excitation model with negative damping (Hossain *et al.*, 2018) indicate ice temperature-based trends of development of ice-induced vibrations that are in contradiction with observed full-scale events, where frequency lock-in was more frequent at warmer temperatures and continuous brittle crushing was more frequent at colder temperatures (Bjerkås *et al.*, 2013; Kärnä, 2011a).

The self-excited vibration theory of vortex-induced vibration and its corresponding dimensionless Strouhal number have been used as an analogy to investigate the mechanism of negative damping in ice-induced vibrations (Izumiyama and Uto, 1997; Ji and Oterkus, 2016; Palmer *et al.*, 2010; Yue and Guo, 2012). Based on small-scale forced vibration, or controlled-oscillation, experiments, it was determined that the dependence of added mass and added damping on ice drift speed suggest that ice-induced vibrations is a self-excitation mechanism, but the dependence of added damping on velocity for ice-induced vibrations is opposite of that for vortex-induced vibrations (Hendrikse, 2017).

1.5.3. ZONAL APPROACH TO CONTACT AREA VARIATION

The non-simultaneous crushing nature of dynamic ice-structure interaction has been universally observed across all scales and for various interaction conditions, especially for wide structures (Jefferies *et al.*, 2008; Kamesaki *et al.*, 1996; Määttänen, 1983; Nord *et al.*, 2015; Sanderson, 1988; Sodhi, 1998; Sodhi *et al.*, 1998; Timco, 1987). To simulate the non-simultaneous ice failure behavior across the ice-structure interface, often in terms of global ice-induced loads, a zonal approach has been applied to dynamic ice-structure interaction models which treats the leading ice edge as a set of independent or correlated zones with local deformation and failure behavior (Ashby *et al.*, 1986; Eranti, 1992; Hendrikse and Nord, 2019; Ji *et al.*, 2018; Kärnä *et al.*, 1999; Kry, 1978; Wu and Qiu, 2019). This method requires either a comprehensive statistical and correlative analysis of local ice loads across the ice-structure interface (Kuiper, 2013), or information about local ice deformation and failure behavior related to physical ice properties.

¹The term *stress rate* is adopted from the literature and should not be conflated with strain rate in the context of ice mechanics.

A physical mechanism that can explain contact area variation in ice-induced vibrations has been referred to as leveling down of protrusions (Kamesaki *et al.*, 1998; Kärnä, 2010). However, this mechanism is limited to intermittent crushing in which transient vibrations of the structure after each load drop cyclically level down the protrusions of the leading ice edge via local crushing. In some cases of intermittent crushing vibrations, prolonged separation of ice and structure occurs after large flaking events which prevents the transient structural vibrations from locally crushing the ice edge, implying that intermittent crushing can occur without transient vibrations leveling down protrusions of the irregular ice edge (Kamesaki *et al.*, 1997; Muhonen *et al.*, 1992; Yap, 2011).

Another physical mechanism for contact area variation in ice-induced vibrations is the speed-dependent ductile-to-brittle transitional deformation and failure behavior of ice (Hendrikse and Metrikine, 2015; Sodhi and Haehnel, 2003). Ductility (or plasticity) in this case refers not to creep but to any process at the ice edge which is time-dependent and irrecoverable. Critics of this mechanism claim that creep-like or transitional ice deformation behavior could not occur on the timescales observed for frequency lock-in vibrations (Kärnä, 2010). The provided counterexample refers to the development of frequency lock-in of a full-scale structure with a natural frequency of 6.2 Hz subjected to ice with thickness of about 0.10 m drifting at about 0.10 m s^{-1} (Xu *et al.*, 2011). If frequency lock-in vibrations were recorded on the structure, then it would be expected that the maximum structural accelerations at the waterline would be on the order of 4 m s^{-2} in accordance with the frequency lock-in relation (Izumiyama and Uto, 1997; Toyama *et al.*, 1983). However, the structural accelerations were not more than 1.5 m s^{-2} , indicating that the ice velocity was overestimated from the video camera. Furthermore, the ductile-to-brittle transition theory is based on small-scale experiments where intermittent crushing and frequency lock-in vibrations were observed at ice speeds on the order of 0.1 m s^{-1} (Sodhi, 1991a; Sodhi, 1991b), demonstrating that transitional ice deformation behavior could occur at relevant timescales.

1.5.4. CONTACT AREA VARIATION AND RATE-DEPENDENT LOCAL FAILURE LENGTH THEORY

A one-dimensional, phenomenological dynamic ice-structure interaction model has been developed which demonstrates auspicious simulated results (Hendrikse and Metrikine, 2015). The model implements a zonal approach, a rate-dependent local failure length, and a nonlinear, statistical global force dependence on ice drift speed which is determined empirically from a rigid reference structure. The model can accurately predict the development of ice-induced vibrations when the target case is similar to the reference case, meaning similar ice conditions and structure properties (Hendrikse and Nord, 2019). The model does not implement any assumptions about the crushing strength or the failure strain of ice. Instead, a local failure length and a number of ice elements are chosen to reproduce the statistical maximum, mean, and standard deviation of brittle crushing loads at high relative velocities. The maximum global load observed in the ductile-to-brittle transition is selected based on full-scale and small-scale observations. Essentially, the model is based on the theory ice-induced vibrations as caused by contact area variation, which has been reported in the literature and was measured by tactile sensors during small-scale tests in model ice (Hendrikse *et al.*, 2012). Two main criticisms

can be levied against the theory and its model. First, the higher global ice-induced loads measured on the structure due to ice-induced vibrations may be the result of contact area increase, local pressure increase, or a combination of both, as indicated from tactile sensor measurements (Ziemer, 2021). No distinction is or can be made regarding the origin of the higher peak loads based on the phenomenology of the contact area variation theory. Contact area variation and local pressure considerations are strongly dependent on the quality of the measurement technique, which is dubious for tactile sensors that have rise times on the order of the duration of the pressure changes. It may be the case that contact area is changing during interaction, but local pressures may be mostly responsible for higher global loads during ice-induced vibrations. Second, the focus on contact area variation is itself phenomenological, given that the changes in contact area are caused by changes in the constitutive behavior of the ice near the interface and by fracture and extrusion processes at the ice edge.

On a broader level, the inherent phenomenological nature of the theory constrains the relationship between the ice properties and the interaction problem to the set of reference parameters chosen to model the problem. For example, ice type (grain structure, density, porosity, and brine volume) is lumped into statistical measurements of load which cannot capture any relationship between changes in the ice properties and loads on the structure, and consequently the resulting changes in ice-induced vibrations. A priori measurements are required to calibrate the phenomenological model, thereby restricting the application of the model to the reference measurements and to scenarios which are similar to those reference cases. On a deeper level, the modeling of the ice with elastic, viscoplastic (Hendrikse and Metrikine, 2015) or viscoelastic (Hendrikse *et al.*, 2018), and viscous deformation and brittle failure was chosen to reproduce the contact area variation and consequent load behavior as observed experimentally. Constitutive ice behavior was not considered when developing the ice elements in the model. Nevertheless, the contact area variation theory assumes ductile or plastic deformations when the relative velocity is low and mostly elastic when the relative velocity is high. While the contact area has been measured to markedly increase at low relative velocity and decrease at high relative velocity (Hendrikse and Metrikine, 2016), the exact type and quantity of deformation in the ice at and near the ice-structure interface during ice-induced vibrations have not been measured. Moreover, questions about whether the ice producing the higher pressures is intact or damaged, or whether pulverized ice adds necessary confinement for the high pressures to develop, remain unanswered by this theory.

The phenomenological ice model by Hendrikse and Nord (2019) demonstrates an approach to the accurate prediction of the development of ice-induced vibrations without needing detailed understanding of the local interaction processes. However, accurate prediction requires model input parameters derived from measurements which are representative of relevant ice conditions. For example, the model input parameters derived from the full-scale observations in the Gulf of Bothnia at the Norströmsgrund lighthouse are mostly unsuitable for accurate prediction of the dynamic ice-structure interaction scenario witnessed on the Molikpaq caisson (Jefferies and Wright, 1988). Simulated cases of the Norströmsgrund lighthouse (Hendrikse and Nord, 2019) and Molikpaq (Owen and Hendrikse, 2019) with the ice model demonstrated accurate prediction of the development of appropriate regimes of ice-induced vibrations, but with significant disparities

in global ice loads and structural responses. The disparities are partly caused by the uncertainty in the ice conditions, e.g. ice thickness, strength, and drift speed, and partly by the complex processes of ice failure and rubble formation not accounted for by the modeling. More fundamentally, physical property measurements, such as ice type and temperature, or even mechanical properties, such as elastic modulus and (uniaxial) compressive strength, are only implicitly incorporated into the model via the global ice load-velocity relation. Therefore, differences in these properties between the locations are largely neglected, and how these differences influence the global ice load-velocity relation is superficially understood.

1.6. KNOWLEDGE GAPS IN THE ICE MECHANICS OF ICE-INDUCED VIBRATIONS

Bringing attention to all of the aforementioned theories of ice-induced vibrations, a core gap in knowledge exists: the relation between the physical or mechanical properties of ice and the ice-induced load on a rigid structure. From a physics-based perspective, or even from a mechanics-based perspective on ice-induced vibrations, the relationship between the constitutive ice behavior and failure and the structural dynamics remains undefined. Focus has been drawn to the contact area at the ice-structure interface due to observations from model-scale experiments (Hendrikse and Metrikine, 2016; Muhonen *et al.*, 1992; Riska and Frederking, 1987; Sodhi, 2001; Takeuchi *et al.*, 2001; Taylor *et al.*, 2019; Ziemer, 2021). Full-scale observations of transition from non-simultaneous to simultaneous global failure of the ice against a structure gives support to the importance of this contact area variation on the development of ice-induced vibrations (Jefferies *et al.*, 2008). However, the contact area and local pressures—while critical as the means of load transfer from the ice to the structure—are also phenomenological in the sense that the constitutive behavior of the ice during interaction is often neglected. In-situ strain measurements of the ice near the interaction zone, although difficult to obtain and analyze, have shown important results in understanding the constitutive ice behavior during ice-structure interaction (Hirayama *et al.*, 1974; Muhonen *et al.*, 1992; Sakai *et al.*, 1998). As generally observed in uniaxial compression of ice over a vast range of strain rates (e.g. Løset *et al.*, 2006; Schulson and Duval, 2009), the ice exhibited elastic, delayed-elastic, viscous, and brittle fracture behavior during ice-structure interaction. The ice model by Hendrikse and Nord (2019) coincidentally captures this behavior in a phenomenological manner, circumventing the mechanical ice properties which could be used for defining the constitutive and fracture behavior, especially in relation to physical properties such as ice type and temperature. Ultimately, it is uncertain whether the phenomenological model can accurately predict the development of ice-induced vibrations without full-scale reference measurements. Rather, it is desirable to pursue a physics-based or phenomenological modeling approach based on mechanical and physical ice properties more directly.

1.7. THESIS OBJECTIVE AND SCOPE

The phenomenological progress and continually missing links between ice physics and full-scale events have led this thesis to seek the main mechanisms of ice-induced vibrations via exhaustive literature review. It was with this method that a hypothesis was formulated in an attempt to explain key mechanisms of ice-induced vibrations. The hypothesis was proposed as follows:

High-pressure zone microdynamics is a significant mechanism that governs ice-induced vibrations, and comprises two distinct primary processes: dynamic recrystallization and microfracture.

These processes would compete in high-pressure zones and depend on temperature, pressure, rate-dependent strain, and microstructure (e.g. Browne *et al.*, 2013; Habib *et al.*, 2014; O'Rourke *et al.*, 2016; Sopper *et al.*, 2017; Wells *et al.*, 2011). The high-pressure zone microdynamics would consequently influence the leading-edge roughness (collection of asperities or protuberances) of the drifting ice floe during ice-induced vibrations, which would contribute to the mechanism by varying the contact area and, therefore, the global ice-induced load on the structure. Other evident processes such as comminution and compaction or sintering would also participate in high-pressure zone microdynamics but would be secondary to dynamic recrystallization and microfracture.

Previous theories and models have explicitly or implicitly incorporated the effects of microfracture in the deformation and failure behavior of ice (e.g. Cormeau *et al.*, 1986; Kavanagh, 2018; Kolari, 2017; Sinha, 1989; Turner, 2018). However, the inclusion of dynamic recrystallization and its effects in the deformation and failure behavior of the ice would be entirely novel to the theory of ice-induced vibrations, although it has been elaborated in high-pressure zone mechanics (Jordaan *et al.*, 2016; Jordaan, 2001). Copious research in cryospheric science and glaciology have measured and simulated dynamic recrystallization and provided a foundation for fostering this topic (e.g. Craw *et al.*, 2018; Faria *et al.*, 2014; Piazzolo *et al.*, 2019; Weiss and Dansereau, 2017).

Dedicated small-scale experiments—including the development of an ice laboratory—were designed and executed to test the hypothesis (see Chapter 3), which required a method to identify dynamic recrystallization in-situ (see Chapter 2). Ultimately, no evidence was found for the presence of dynamic recrystallization as either a cause for or effect of cyclic crushing of confined ice representing the ice edge during ice-induced vibrations. However, evidence for strongly viscous behavior² of ice at timescales relevant for ice-induced vibrations was found, a finding which was remarkably similar in character to the results from ice tank tests (see Chapter 4). Further research on the constitutive and strength behavior of ice under strain and strain-rate paths resembling those during ice-induced vibrations would likely grant more insight, and therefore predictive power, into the ice mechanics involved in ice-induced vibrations.

² *Strongly viscous behavior* is treated as an umbrella term for any strain or stress response in the ice which is rate-dependent.

1.8. THESIS OUTLINE

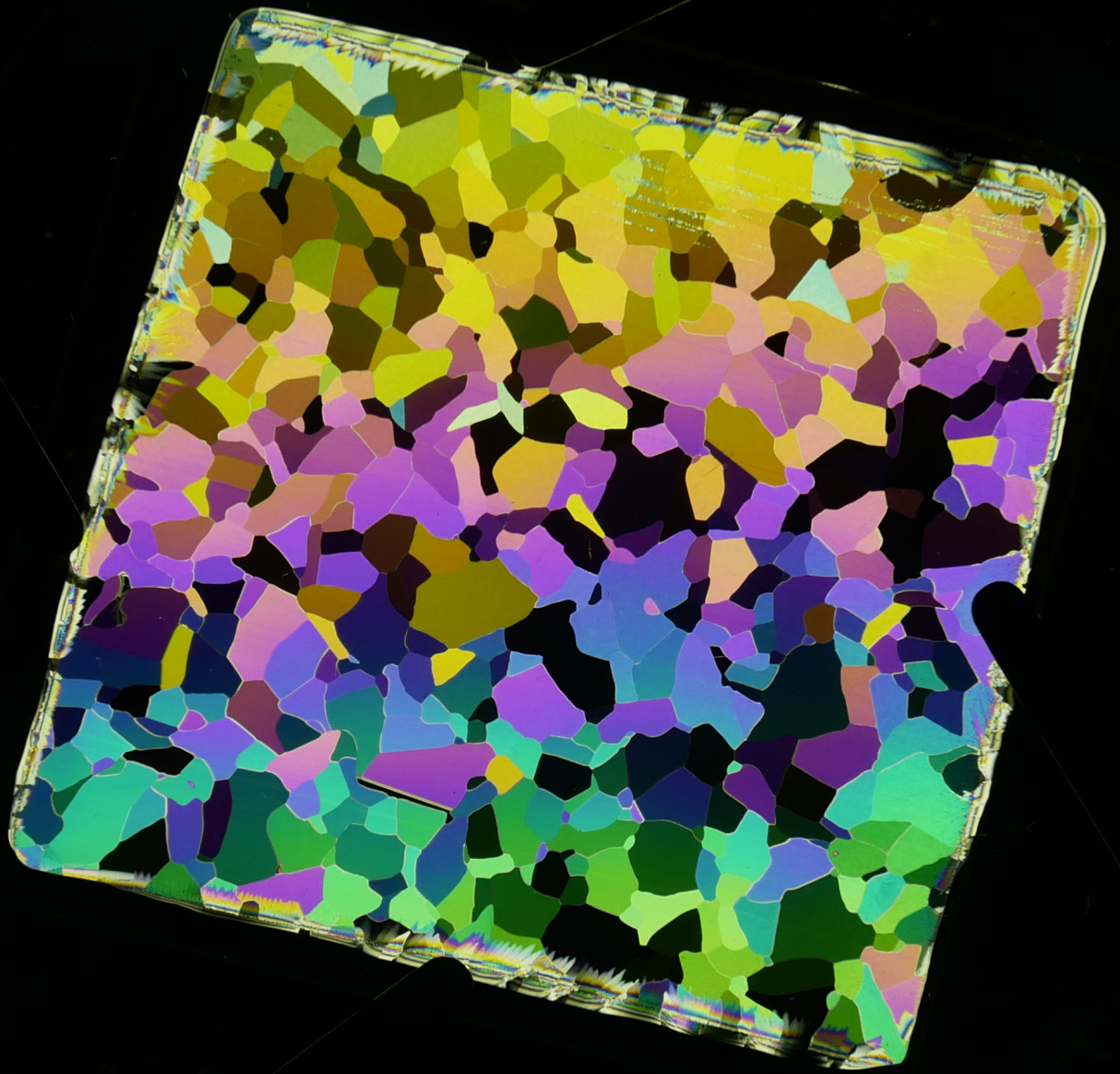
The thesis is formatted as a collection of journal publications. The publications are presented per chapter in chronological order and are the main body of research conducted in the thesis. The thesis contains five chapters, of which Chapter 1 has introduced the topic and scope. The following three chapters (Chapters 2 to 4) present the journal publications, which have been formatted to this dissertation. Minor typographical errors have been corrected and a corrigendum to Chapter 4 has been incorporated, but otherwise the journal publications appear as published. The thesis is concluded in Chapter 5 with a summary of the chapter conclusions and discussion, and an outlook on future work is offered.

Chapter 2 explains the interference coloration of ice thin sections in crossed-polarized transmitted light, and its relevance for ice texture and fabric analysis. The theory is elaborated and a method is developed for determining the size and *c*-axis (quarter) orientation of each grain based on a collection of in-plane photographs of an ice thin section rotated about its azimuth in a polariscope. The method was intended for in-situ identification of dynamic recrystallization using the test setup described in the next chapter.

Chapter 3 describes the dedicated experiments performed to assess whether dynamic recrystallization plays a role in the development of ice-induced vibrations. A thin ice plate was confined laterally by glass plates and subjected to cyclic crushing on the edge via a steel indenter with a haversine velocity waveform. The ice deformation and failure processes were observed through the glass plates with crossed-polarized transmitted light with the intention of identifying changes in the fabric and texture of the ice plate. Dynamic recrystallization was not observed; instead, stress relaxation of the ice, as confirmed by load signal and stress-induced birefringence changes, was observed, indicating strongly viscous ice behavior on timescales relevant for the frequency lock-in regime of ice-induced vibrations. An interpretation of the results suggests that the ice deformation mechanisms involved in frequency lock-in vibrations operate on microscopic length scales. Moreover, this type of ice deformation behavior was qualitatively similar to the load signals measured during ice penetration tests with controlled-oscillation of a rigid model-scale structure as described in the following chapter.

Chapter 4 compares the results from ice penetration tests with a rigid structure, controlled-oscillation, and single-degree-of-freedom oscillator. Based on this comparison, it was possible to discern a rapid strengthening of the ice following periods of low relative velocity between ice and structure. It was observed that the peak loads during the controlled-oscillation and single-degree-of-freedom vibration tests never exceeded those from the rigid structure tests at the same relative velocity. Whether contact area variation, change in constitutive ice behavior, or a combination thereof are responsible for the rapid strengthening observed warrants further experimental investigation.

Chapter 5 summarizes the conclusions from the chapters, offers a discussion on the ice mechanics in ice-induced vibrations, and gives an outlook on future research on this topic.



2

AN INITIAL STUDY OF INTERFERENCE COLORATION FOR QUANTIFYING THE TEXTURE AND FABRIC OF ICE

In this chapter, a novel approach is presented for ice microstructural analysis in terms of grain size and c -axis (quarter) orientation based on the interference coloration of each grain in a thin section in crossed-polarized transmitted light. This approach was designed as a means to identify and quantify dynamic recrystallization of ice under compressive loading scenarios relevant for ice-induced vibrations. The interference coloration method is combined with the experiments as described in Chapter 3 to test the hypothesis as stated in Section 1.7. The approach is also capable of analyzing ice thin sections for the purpose of ice type identification and quantification, which can be used to infer ice growth and deformation history. Example ice thin section analyses are demonstrated with the approach and a validation is performed by comparison of the approach with the traditional Rigsby stage technique.

This chapter has been published in *Cold Regions Science and Technology*, 2023 (Owen and Hendrikse, 2023).

ABSTRACT

The manual application of universal (Rigsby) stage techniques is commonly used to determine the fabric of thin sections of ice viewed with crossed-polarized light. This process can require hours of focus in cold conditions to identify the *c*-axis of each grain in a thin section. Automated ice texture and fabric methods of several forms exist but are rarely implemented beyond the field of glaciology. The present study introduces a method based on the theory of interference coloration for automated ice texture and quarter fabric analysis by using in-plane conventional photography of an ice thin section as input. The method is compatible with universal stages and polariscopes, and is not restricted by the planar-face dimensions of the thin section, allowing for thin section analysis of any size when sufficient digital camera resolution is available. Light source color temperature and chromatic adaptation are considered in the interference coloration theory, and ice fabrics are simulated for reference in identifying ice types. Sample thin section texture and quarter fabric analyses from freshwater lake and laboratory-grown ice are presented to demonstrate the applications of the method. The method is compared with the Rigsby stage technique, which yielded mean (standard deviation of) azimuth and inclination errors of 2.9 (1.0) and 11.5 (8.0) degrees, respectively, thereby demonstrating accuracy sufficient for quantifying quarter fabrics when considering a mean standard deviation in inclination of 5.4 degrees with the Rigsby stage technique.

2.1. INTRODUCTION

The measurement of ice microstructure—herein referring to texture and fabric (Sammonds *et al.*, 2017; Thorsteinsson *et al.*, 1997)—utilizing birefringence was first implemented by Rigsby (1951) on glacial ice and the technique was later elaborated by Langway (1958). Classifications of ice microstructure were then formally catalogued by Michel and Ramseier (1971) based on thin sections that were analyzed with a universal stage and the results were presented with Schmidt equal-area projection plots (also known as Wulff stereographic net or stereonet). These stereonet (from stereographic projection of spherical coordinates onto a circular plane) and other fabric methods represent the orientation distribution of the *c*-axes, coincident with the optic axes, of the ice grains, from which the growth and deformation histories and mechanical properties can be ascertained. Historically, ice textures were determined from scaled photographs of ice thin sections viewed between crossed polarizers (Perey and Pounder, 1958; Thorsteinsson *et al.*, 1997).

Detailed ice textures and fabrics are evident in experiments relevant for glaciological studies (e.g. Chauve *et al.*, 2015; Grennerat *et al.*, 2012; Peternell *et al.*, 2014), but such analyses are only applied to a limited extent in freshwater and saline ice cover research (e.g. Cole *et al.*, 1998; Schulson and Duval, 2009). One reason for this absence of ice microstructure analysis is the arduous nature of manual identification of numerous *c*-axes in a universal (Rigsby) stage in a subzero working environment, which is the manner by which this information is still extracted in contemporary studies (e.g. Gharamti *et al.*, 2021; Wei *et al.*, 2020). Furthermore, when ice textures are made, they are still done by manually tracing grain boundaries and counting grains in a thin section or by using the linear intercept method (e.g. Snyder *et al.*, 2015). Instead, typically only photographs are provided of an ice thin section viewed between crossed polarizers with a reference

length scale and little mention is made of the relevance of the ice texture and fabric to the mechanical behavior (e.g. Hendrikse *et al.*, 2022b; O'Rourke *et al.*, 2016; Seymour-Pierce *et al.*, 2017; Sinha, 2011; Sopper *et al.*, 2017; Timco and Weeks, 2010). An exception to this trend is the use of the Schmid (orientation) factor to characterize the effects of alignment of the *c*-axes on the constitutive behavior of freshwater and sea ice (Azuma, 1994; Azuma, 1995; Chauve *et al.*, 2017; Cole *et al.*, 1998; Cole, 1998; Grennerat *et al.*, 2012; O'Connor *et al.*, 2020; Wei *et al.*, 2022).

Instruments and techniques have been developed over the years in an attempt to automate this process, which were found to be satisfactory but rarely proliferated outside of the laboratory in which they were created (Eicken, 1993; Lange, 1988; Morgan *et al.*, 1984; Yun and Azuma, 1999). Furthermore, the procedure for the universal stage and analysis of the results have improved markedly since Rigsby first documented the technique (Hansen and Wilen, 2002; Hill and Lasca, 1971; Wilen *et al.*, 2003). Most notably, a device for automated and robust thin section analysis is commercially available (Wilson and Peternell, 2011) and has been successfully used in various ice applications (Georges *et al.*, 2021; Grennerat *et al.*, 2012; Montagnat *et al.*, 2021). Alternatively, electron backscatter diffraction (EBSD) (e.g. Iliescu *et al.*, 2004; Monz *et al.*, 2021; Seidemann *et al.*, 2020) is used to determine the *c*-axes—and *a*-axes, which are not discernable from optical methods—of a thin section, though this equipment is highly specialized, requires specially-trained operators, and admits only relatively small ice specimens for analysis.

Also crucial to the discussion of textures and fabrics of ice thin sections is the process of thin sectioning itself. Techniques ranging from rough (hand-melting the ice (Langway, 1958; Shokr and Sinha, 2015)) to refined (double-microtoming method (Shokr and Sinha, 2015; Sinha, 1977)) to something in between (CNC milling) yield different results of thin sectioning which can influence the quality of the surface roughness and thus the image processing of the photographs taken for automated texture and fabric analysis. Presented herein is a method of preparing ice thin sections and analyzing ice textures and quarter fabrics via in-plane photography with any digital camera based on the interference coloration of the ice. Additionally, ice fabrics are simulated with the interference coloration theory which provide a visual reference for ice type identification. Finally, the method is compared with the Rigsby stage technique, sample results are presented, and limitations are identified based on laboratory-grown freshwater ice and ice specimens taken from in the IJsselmeer near Breezanddijk, Netherlands in February 2021.

2.2. THEORY

2.2.1. ICE BIREFRINGENCE IN LINEARLY POLARIZED LIGHT

Water ice at standard atmospheric conditions of Earth has hexagonal (Ih) crystal structure and, consequently, optically positive uniaxial birefringence (Hobbs, 1974; Pauling, 1935; Petrenko and Whitworth, 1999) (Hobbs, 1974; Pauling, 1935; Petrenko and Whitworth, 1999). While pure freshwater ice is transparent under unpolarized visible light, the shape and orientation of the grains can be readily distinguished to the observer with linearly polarized light because of the birefringence of the ice (see Figure 2.1). The birefringence, or double refraction, of ice is weakly dependent on the visible wavelength of light and on temperature above -60°C , and is strongly dependent on the angle between the linearly

polarized incident light ray (wave normal) and the c -axis, the principal axis of symmetry and the optic axis of the hexagonal crystal (see Figure 2.2a) (Bloss, 1961; Hobbs, 1974; Petrenko and Whitworth, 1999; Schulson and Duval, 2009). This double refraction of ice can be described by a refractive index tensor ellipsoid, or indicatrix (see Figure 2.2b) (Fueten and Goodchild, 2001; Shestov, 2018).

2

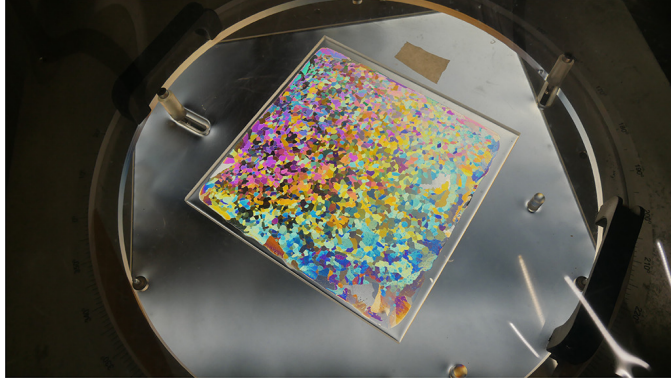


Figure 2.1: Oblique photograph of laboratory-grown columnar horizontal ice thin section viewed with crossed-polarized transmitted light in a large polariscope in the ice laboratory at Delft University of Technology. The acrylic plate on which the thin section is welded has dimensions of 220 mm square.

The angle between the incident light ray (coincident with vertical viewing axis or line of sight (LoS)) and the c -axis of an ice crystal can be defined as θ and is typically referred to as inclination angle (Heilbronner and Pauli, 1993), (or sometimes plunge angle (Fueten and Goodchild, 2001) or colatitude angle (Peternell *et al.*, 2011)). The positive birefringence of ice Δn is defined as the difference between the refractive index of the extraordinary ray and the refractive index of the ordinary ray:

$$\Delta n(\lambda) = n_e(\lambda) - n_o(\lambda) \quad (2.1)$$

with:

$$n_e(\lambda) = \frac{n_o(\lambda)}{\sqrt{1 + \left(\frac{n_o(\lambda)}{n_c(\lambda)} - 1\right) \sin^2(\theta)}} \quad (2.2)$$

and:

$$n_o(\lambda) = n_\omega(\lambda) \quad (2.3)$$

where λ is the wavelength of the incident light, n_c and n_ω are the refractive indices of the extraordinary and ordinary rays, respectively, and n_e and n_o are the refractive indices of the extraordinary and ordinary rays, respectively, that are projected from the indicatrix via inclination angle to the plane orthogonal to the incident ray (see Figure 2.2b). The term n_o is constant because the cross section of the indicatrix related to the ordinary ray

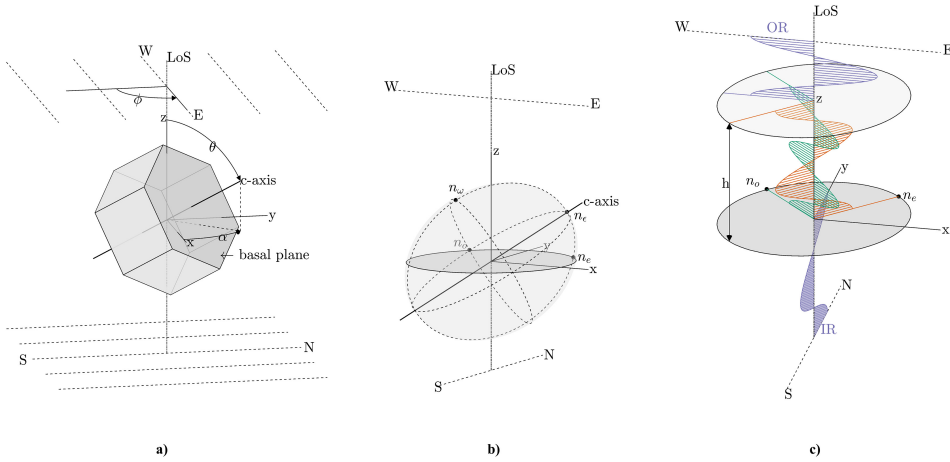


Figure 2.2: Diagrams of ice grain specimen between linear polarizers. **a):** Ice crystal unit cell (orientation of a -axis is arbitrary) with orientation of c -axis (orthogonal to the basal plane) relative to the line of sight (LoS). The c -axis orientation is defined by the inclination angle θ and azimuth angle α relative to the LoS. The angle ϕ between the privileged directions of the N-S polarizer and the W-E polarizer (called the analyzer) is set according to the type of polarization desired. **b):** Corresponding refractive index tensor ellipsoid of the ice crystal unit cell with refractive indices projected onto the plane orthogonal to the incoming light ray. **c):** The tensor ellipsoid projected plane with transmission of light rays through the ice of thickness h . The incident ray (IR) is decomposed into the extraordinary ray (color orange) projected onto the c -axis and the ordinary ray (color green) projected orthogonal to the c -axis, and with a path difference caused by the birefringence Δn . The combination of c -axis orientation and ice thickness determine the transmission of the resultant outgoing ray (OR) through the analyzer with orientation $\phi = 90^\circ$ in this case of crossed-polarization ($\theta = 60^\circ$, $\alpha = 45^\circ$, h and light wavelengths not to scale). For more information, refer to, e.g., Bloss (1961) and Shestov (2018). Note that the diagrams are shown at different viewing perspectives for clarity.

is circular. The term n_e varies elliptically between n_ω and n_c as defined by the indicatrix. The refractive indices of ice as a function of visible light wavelength and temperature (which is treated as constant and about -3°C in this study) are listed in Table 2.A.1. The refractive indices are fit by a Cauchy approximation (Heilbronner and Pauli, 1993):

$$n_{\omega,\epsilon}(\lambda) = A_{\omega,\epsilon} + \frac{B_{\omega,\epsilon}}{\lambda^2} + \frac{C_{\omega,\epsilon}}{\lambda^4} + \mathcal{O}(\lambda^4) \quad (2.4)$$

where a fourth-order approximation is deemed sufficient for the purposes of this study and the corresponding coefficients A , B , and C are fit to the measured data from Table 2.A.1 for n_ω and n_c (see Figure 2.3). The coefficients for the Cauchy approximations of n_ω and n_c of ice and their respective R-squared values as a function of wavelength in nanometers are provided in Table 2.1.

When an individual ice grain is viewed in a polarization microscope (Heilbronner and Barrett, 2014), polariscope (Pounder, 1965; Shokr and Sinha, 2015), or similar configura-

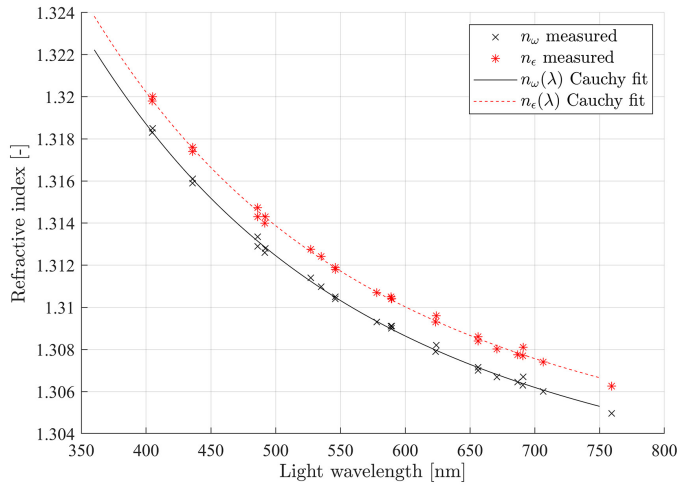


Figure 2.3: Measured refractive indices as a function of the wavelength of light for the ordinary and extraordinary rays of ice (Heilbronner and Barrett, 2014; Hobbs, 1974; Petrenko and Whitworth, 1999). The measured values from Table 2.A.1 are fit with a Cauchy approximation (Heilbronner and Pauli, 1993).

Table 2.1: Coefficients and the R-squared value for the fourth-order Cauchy approximation of the refractive indices of the ordinary and extraordinary rays of ice as a function of light wavelength in nm (see Figure 2.3).

	Ordinary	Extraordinary
<i>A</i>	1.2989	1.3002
<i>B</i>	3.7945×10^3	3.8042×10^3
<i>C</i>	-9.9396×10^7	-9.6295×10^7
R-squared	0.9984	0.9983

tion of crossed-polarized transmitted light system, emitted light first passes through the polarizer with nominally north-south (N-S) orientation, which linearly polarizes the light with vertical incident ray (wave normal) and transverse wave parallel to the polarizing (privileged) direction (IR with color purple in Figure 2.2c). The linearly polarized light then passes through the ice grain, resolving the light into an ordinary ray (color green in Figure 2.2c) and an extraordinary ray (color orange in Figure 2.2c) with transverse waves in the plane of the respective n_o and n_e which were projected onto the plane orthogonal to the incident ray. Depending on θ , a difference in the refractive indices means that the extraordinary ray passes through the grain more slowly and results in a retardation, or phase shift, at the exit of the grain between the ordinary and extraordinary transverse waves. Thus, elliptically polarized light exits the grain with a resultant transverse wave which reaches the upper polarizer (called the analyzer) with west-east (W-E) privileged direction and may be accepted or rejected depending on whether its components are in

that W-E orientation. Finally, the light reaches the receiver (eye, camera, etc.) if the light is accepted by the analyzer.

If no crystal were present, and the angle between the polarizer and analyzer privileged directions ϕ were 90° , then minimum light would pass to the receiver and the image would appear dark. By placing the crystal between the polarizer and analyzer, depending on the orientation of the crystal, interference coloration of the crystal can occur. This is caused by different transmission of the spectral component wavelengths of white light through the analyzer and results in certain colors absorbed and others not (Bloss, 1961; Shestov, 2018). The specific color of a crystal is dependent on Δn (function of θ), thickness of the ice h , angle between polarizer and analyzer ϕ , and the azimuth angle between the polarizer and the c -axis of the crystal α . The intensity of the transmission of the light through the system is defined:

$$I = I_0 \cos^2 \phi - \sin 2(\alpha - \phi) \sin(2\alpha) \sin^2 \left(\frac{2\pi h \Delta n}{2\lambda} \right) \quad (2.5)$$

where I_0 is the incident light intensity (Bloss, 1961; Heilbronner and Pauli, 1993; Price, 1973; Sørensen, 2013). For typical crossed-polarization, $\phi = 90^\circ$, which simplifies Equation (2.5) to the following:

$$I|_{\phi=90^\circ} = I_0 \sin^2(2\alpha) \sin^2 \left(\frac{2\pi h \Delta n}{2\lambda} \right) \quad (2.6)$$

which follows Shestov (2018). For a range of h , θ , and α , with $\phi = 90^\circ$, the intensity of transmission of visible light through the system is shown (see Figure 2.4). When the c -axis of the ice crystal is coincident with the incident light ray, $\theta = 0^\circ$, the refractive index of the extraordinary ray equals that of the ordinary ray and the difference, the birefringence, is zero. As a result, the intensity is also zero. The intensity is minimum for $\alpha = 0^\circ$ and increases to maximum for $\alpha = 45^\circ$, but only influences the amplitude and not the proportional shape of the intensity curve over the wavelength spectrum. In other words, α affects the relative brightness of the color of an ice crystal when viewed between crossed polarizers. The color of a crystal is then dependent on h and θ .

The color of an ice crystal, when observed between crossed polarizers, is the combination of the visible light wavelengths that pass through the system, and can be characterized by a quality function (Shestov, 2018):

$$Q = I_{max} \left[1 - \int_{\lambda_{violet}}^{\lambda_{red}} I d\lambda / (I_{max} (\lambda_{red} - \lambda_{violet})) \right] \quad (2.7)$$

where I_{max} is the maximum intensity for the range of visible light wavelengths. Note that $\lambda_{violet} = 350 \text{ nm}$ and $\lambda_{red} = 750 \text{ nm}$. This quality function is used in the following section with the interference coloration of ice in crossed-polarized light to demonstrate the coloration of ice grains as a function of c -axis orientation and specimen thickness.

2.2.2. INTERFERENCE COLORATION OF ICE IN CROSSED-POLARIZED LIGHT

The phenomenon of interference colors of birefringent minerals in polarized light is well-established in mineralogy (Bloss, 1961; Murphy, 2001; Raith *et al.*, 2012). However, digital

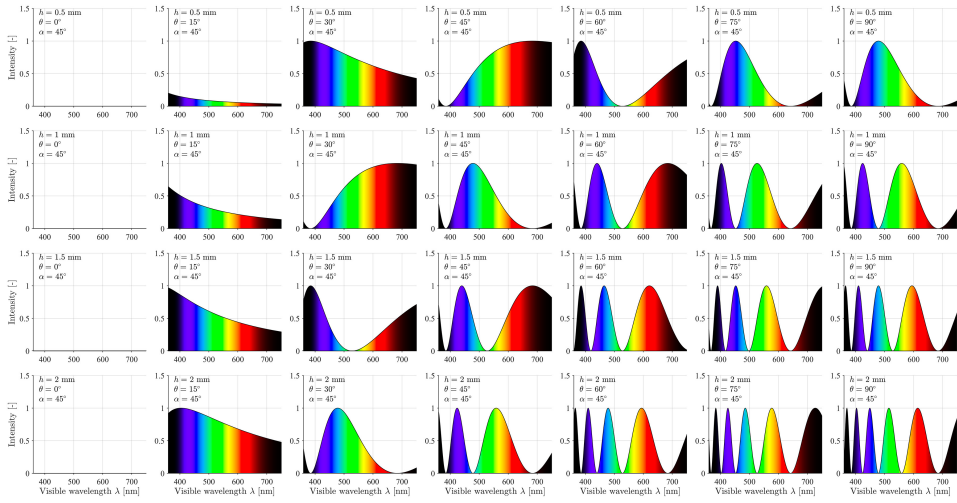


Figure 2.4: Intensity of transmission of visible light through the crossed-polarized birefringence light system for ranges of ice thickness h and inclination angle θ , with azimuth angle $\alpha = 45^\circ$ for maximum intensity. Initial intensity I_0 is assumed at unity. The colors for the visible wavelengths of light are converted to RGB values for plotting purposes (Stockman *et al.*, 2020).

techniques to accurately represent interference colors in human vision on computer monitors is an ongoing study (Linge Johnsen *et al.*, 2018; Sørensen, 2013). With this in mind, the following is an attempt to portray the interference coloration of ice thin sections. To begin, the intensity from the special case in Equation (2.6) is called the spectral color transmission \bar{I}_λ as a vector or matrix and calculated over the range of visible wavelengths of light and expressed as follows (Sørensen, 2013):

$$\bar{I}_\lambda(h, \theta, \alpha) = \begin{bmatrix} I(\lambda = 350 \text{ nm}, h, \theta, \alpha) \\ \vdots \\ I(\lambda = 750 \text{ nm}, h, \theta, \alpha) \end{bmatrix} \quad (2.8)$$

where the visible spectrum is considered from 350 nm to 750 nm. The spectral color transmission must be converted from wavelengths of light to red, green, and blue (RGB) channel values for digital displays; this is done with two steps. The first is conversion from spectral color to human vision color with use of the CIE1931 color matching functions (Stockman *et al.*, 2020):

$$\bar{I}_{XYZ}(h, \theta, \alpha) = \begin{bmatrix} \vec{r}_\lambda \\ \vec{g}_\lambda \\ \vec{b}_\lambda \end{bmatrix} \bar{I}_\lambda(h, \theta, \alpha) = \begin{bmatrix} X \\ Y \\ Z \end{bmatrix} \quad (2.9)$$

where \vec{r}_λ , \vec{g}_λ , and \vec{b}_λ are the red, green, and blue sensitivity functions and X , Y , and Z are the human vision color coordinates (Sørensen, 2013). The second step is conversion

from human vision color coordinates to RGB channel values for digital displays. This conversion is done via linear transformation to Adobe RGB (Pascale, 2003):

$$RGB_{linear} = M_{RGB} \begin{bmatrix} X \\ Y \\ Z \end{bmatrix} = \begin{bmatrix} R \\ G \\ B \end{bmatrix} \quad (2.10)$$

with:

$$M_{RGB} = \begin{bmatrix} 2.0414 & -0.5649 & -0.3447 \\ -0.9693 & 1.8760 & 0.0416 \\ 0.0134 & -0.1184 & 1.1054 \end{bmatrix} \cdot 10^{-2} \quad (2.11)$$

where X , Y , and Z are the red, green, and blue channel values of human vision, respectively. Note that there is a typographical error in the first element (row and column 1) of Equation 6 in Sørensen (2013), which is corrected herein according to page 21 of Pascale (2003). Additionally, the linear transformation matrix M_{RGB} is reduced by two orders of magnitude for RGB channel values between 0 and 1 in MATLAB. However, the linear RGB channel vector RGB_{linear} contains values outside the admissible 0 to 1 range for RGB channel values, which then requires values greater than 1 and less than 0 to be set to 1 and 0, respectively:

$$v_i = \begin{cases} 1, & u_i > 1 \\ 0, & u_i < 0 \\ u_i, & \text{else} \end{cases} \quad \text{for } i = 1, 2, \dots, N \quad (2.12)$$

where i is an element in RGB_{linear} , v is the clipped RGB channel value, u is the unclipped RGB channel value, and N is the number of elements in RGB_{linear} . Finally, a nonlinear gamma correction is applied to the clipped linear RGB channel vector in accordance with the Adobe RGB 1998 standard (Adobe Systems, 2005):

$$w_i = \begin{cases} v_i^\gamma, & v_i^\gamma \geq 0 \\ -(-v_i)^\gamma, & v_i^\gamma < 0 \end{cases} \quad \text{for } i = 1, 2, \dots, N \quad (2.13)$$

where w_i is the gamma-corrected, clipped RGB channel value, and $\gamma = (2.19921875)^{-1}$. The resulting gamma-corrected, nonlinear RGB channel vector represents the color corresponding to a given ice thickness and c -axis orientation; this result can be populated for ranges of thicknesses, inclination angles, and azimuth angles and plotted with the quality function (see Figures 2.5 to 2.7). Colors of individual grains can be identified and attributed with known birefringence to the Michel-Lévy color chart or the Raith-Sørensen chart (Raith *et al.*, 2012; Sørensen, 2013). Azimuth and inclination angles of zero result in extinction of the ice crystal as expected since birefringence is zero. For nonzero inclination angle, the azimuth angle controls the brightness, i.e. amplitude, of the given range of colors. For increasing inclination angles from zero to maximum, the interference colors of the quality function become less monochromatic and more vibrant for the given range of ice thicknesses. For ice thicknesses greater than about 2 mm and for grains with high inclination angles, the colors become more like white light with numerous passes of the wavelengths of light. Practically, this means that c -axis orientations can no longer

be distinguished reliably as most or all of the grains possess coloration varying between extinguished dark and grey or white interference coloration.

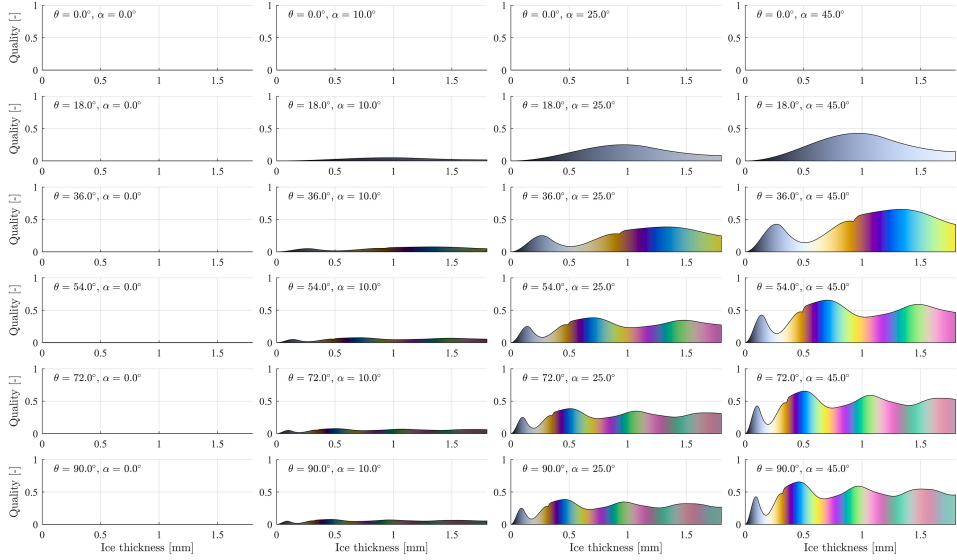


Figure 2.5: Interference colors from the quality function that are transmitted by the birefringence system, for a range of inclination angles and azimuth angles, as a function of ice thickness.

To summarize the possible interference colors observable for different ice thicknesses, conoscopic interference color patterns are shown in Figure 2.8. The interference colors display four-fold symmetry, i.e. 90° degeneracy, meaning that the c -axis of a grain cannot be resolved to its true quadrant in a stereonet in this crossed-polarization system. This limitation is illustrated in Section 2.2.4 and addressed in Section 2.5.

2.2.3. EFFECT OF LIGHT SOURCE COLOR TEMPERATURE ON INTERFERENCE COLORATION

While Sørensen (2013) provides a valuable framework by which to visualize interference coloration on digital displays, their approach ignores a fundamental component: color temperature of the light source (Linge Johnsen *et al.*, 2018). The color temperature influences the light source spectral distribution; this light source color temperature can be determined when the light is assumed to originate from a black body irradiator as monochromatic irradiance or emissive power [W m^{-3}] (Forsberg, 2021):

$$E_{b\lambda} = \frac{C_1 \lambda^{-5}}{\exp\left(\frac{C_2}{\lambda T_c}\right) - 1} \quad (2.14)$$

where constant $C_1 = 3.74 \times 10^{-16} \text{ W m}^2$, constant $C_2 = 1.4388 \times 10^{-2} \text{ mK}$, and color temperature T_c is in units of Kelvin. In adjusting the interference colors based on the

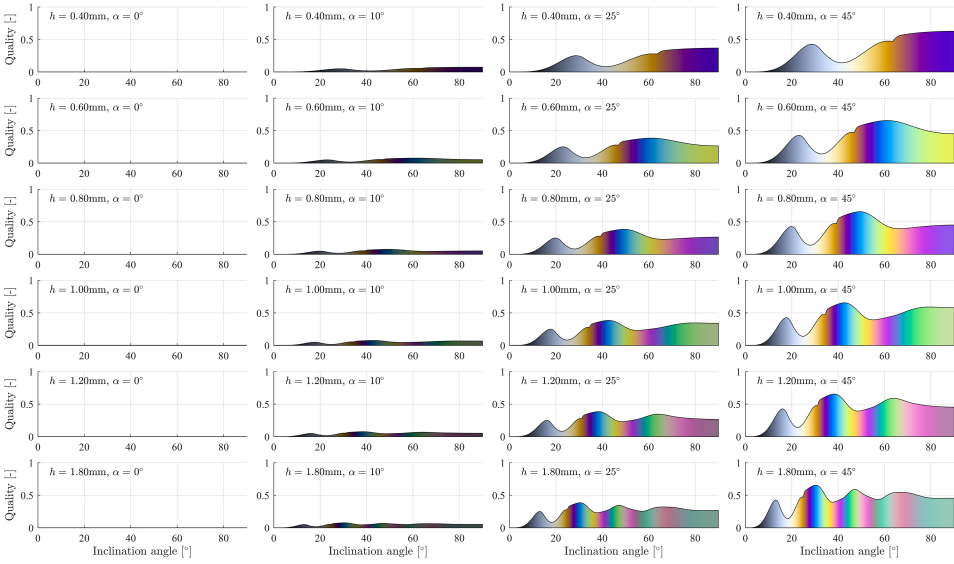


Figure 2.6: Interference colors from the quality function that are transmitted by the birefringence system, for a range of ice thicknesses and azimuth angles, as a function of inclination angle.

color temperature of the light source, Equation (2.9) is altered as follows (Linge Johnsen *et al.*, 2018):

$$\begin{aligned}
 \vec{J}_{XYZ} &= \begin{bmatrix} \vec{r}_\lambda \\ \vec{g}_\lambda \\ \vec{b}_\lambda \end{bmatrix} \left(\hat{E}_{b\lambda} \odot \bar{I}_\lambda(h, \theta, \alpha) \right) \\
 &= \begin{bmatrix} \vec{r}_\lambda \\ \vec{g}_\lambda \\ \vec{b}_\lambda \end{bmatrix} \left(\begin{bmatrix} \hat{E}_{b\lambda}(\lambda = 350 \text{ nm}, T_{CLS}) \\ \vdots \\ \hat{E}_{b\lambda}(\lambda = 750 \text{ nm}, T_{CLS}) \end{bmatrix} \odot \bar{I}_\lambda(h, \theta, \alpha) \right)
 \end{aligned} \tag{2.15}$$

where $\hat{E}_{b\lambda}$ is the monochromatic irradiance spectrum vector of the light source normalized by its maximum value over the spectrum, operator \odot is the Hadamard (element-wise) product, and T_{CLS} is the light source color temperature. The application of Equation (2.15) to the previous procedure to obtain the interference colors will result in colors that have a white-balance shift in color temperature. To adjust interference coloration from a light source with a warm or cool color temperature to interference coloration with white balance or other color temperature, a transformation is performed by using the light source color temperature and a target color temperature. This procedure is called chromatic adaptation and is done with the following manipulations:

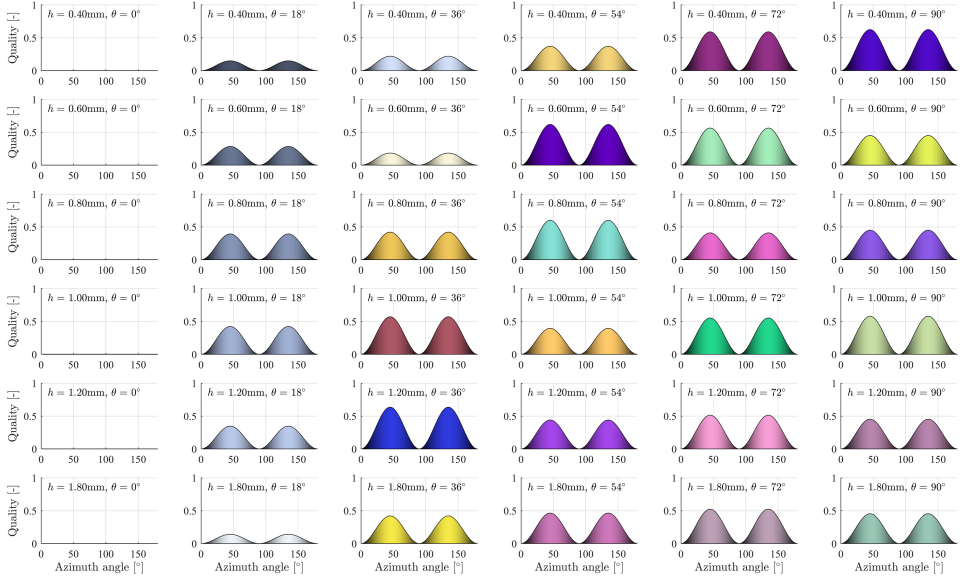


Figure 2.7: Interference colors from the quality function that are transmitted by the birefringence system, for a range of ice thicknesses and inclination angles, as a function of azimuth angle.

$$\vec{W}_{XYZ}(T_{cLS}) = M_A \begin{bmatrix} \vec{r}_\lambda \\ \vec{g}_\lambda \\ \vec{b}_\lambda \end{bmatrix} \hat{E}_{b\lambda}(T_{cLS}) \quad (2.16)$$

and:

$$\vec{W}_{XYZ}(T_{cTg}) = M_A \begin{bmatrix} \vec{r}_\lambda \\ \vec{g}_\lambda \\ \vec{b}_\lambda \end{bmatrix} \hat{E}_{b\lambda}(T_{cTg}) \quad (2.17)$$

with:

$$M_A = \begin{bmatrix} 0.8951 & 0.2664 & -0.1614 \\ -0.7502 & 1.7135 & 0.0367 \\ 0.0389 & -0.0685 & 1.0296 \end{bmatrix} \quad (2.18)$$

Where T_{cTg} is the target color temperature and M_A is the linearized Bradford matrix (Linge Johnsen *et al.*, 2018; Pascale, 2003). Next, the chromatic adaptation transformation matrix is constructed:

$$M_{CA} = M_A^{-1} \text{diag}(\vec{W}_{XYZ}(T_{cTg}) \odot \vec{W}_{XYZ}(T_{cLS})^{-1}) M_A \quad (2.19)$$

where $\text{diag}(\cdot)$ is the diagonalization operator. Finally, the light-sourced modified human color vision matrix \vec{J}_{XYZ} is chromatically adapted:

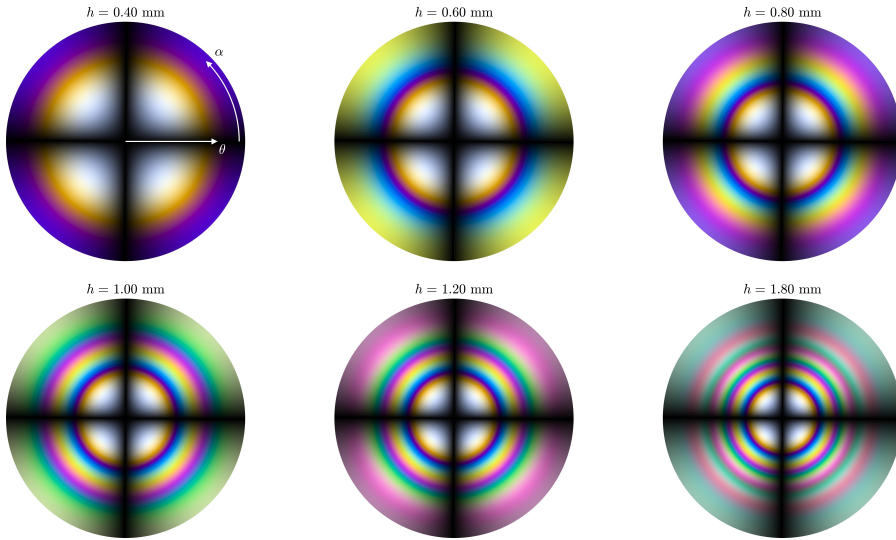


Figure 2.8: Conoscopic interference color patterns, for a range of ice thicknesses, as a function of azimuth and inclination angles. Note that the LoS is coincident with the center of the conoscopic interference color pattern.

$$\bar{J}_{XYZca} = M_{CA} \bar{J}_{XYZ} \quad (2.20)$$

where this chromatically adapted matrix can then be used in Equations (2.10) to (2.13) as previously explained. An example of chromatic adaptation is presented in the next section. Note that, unless otherwise stated, all simulated interference colors in the present study are rendered at a color temperature of 6504 K.

2.2.4. MULTI-LEVEL VORONOI TESSELLATION FOR SIMULATED ICE FABRICS

By using interference colorations and Voronoi tessellation (dual graph of Delaunay triangulation), representative thin sections of ice textures (or fabrics) can be artificially generated. However, the representative grains generated by Voronoi tessellation do not follow any grain growth behavior expected during ice cover formation. As a compromise between conventional Voronoi tessellation and grain growth simulation based on thermodynamics and geometric constraints, an ad hoc multi-level Voronoi tessellation is implemented (Yadegari *et al.*, 2014). An example simulated thin section is shown in Figure 2.9 with a polar plot of the orientation of the c -axes and their respective interference color at initial specimen orientation. Extinction angles can be seen around inclination angles of zero and azimuth angles collinear with the privileged directions of the polarizer (N-S) and analyzer (W-E), as viewed in the polar plot (note the four-fold symmetry of the interference colors). This ice fabric is roughly representative of a medium-diameter-grained granular or columnar horizontal thin section with random c -axis orientations as observed in ice types P2–P4 and S2, S4, S5, and T1–T3 (Michel and Ramseier, 1971). For

freshwater columnar and first-year sea ice immediately below the transition layer (e.g. Schwarz and Weeks, 1977), type S2 ice is observed and would appear with a distribution of colors such as in Figure 2.10. It is clear that c -axes randomly oriented in the plane of the thin section would display roughly one or two colors with a range of brightness between those respective colors and extinction. This approach can also be used to examine the effect of light source color temperature without chromatic adaptation on the interference coloration of the grains, in this case the effect on S2 type ice (see Figure 2.11).

2

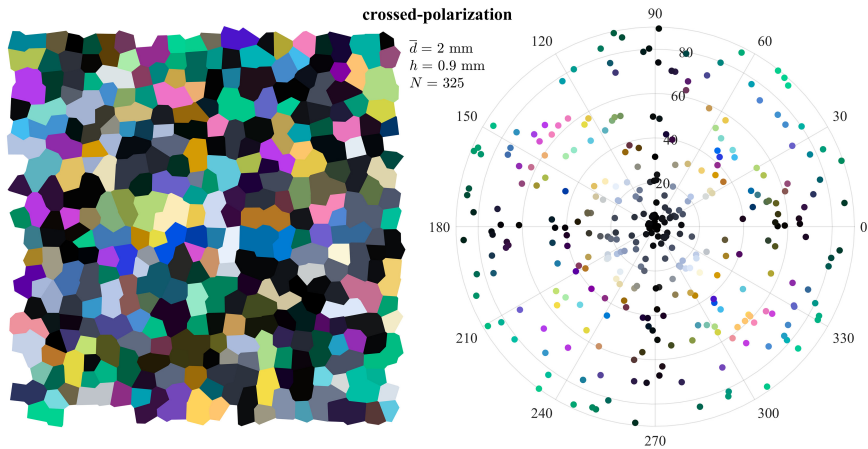


Figure 2.9: Example multi-level Voronoi diagram of representative, simulated ice fabric in crossed-polarized backlighting with thickness h , and with quantity N ice grains of uniformly distributed size with arbitrary top-level diameter \bar{d} . Right: polar plot with interference-colored points of inclination (radial) and azimuth (circumferential) angles in degrees as defined for each of the ice grains.

2.3. METHODOLOGY

There are two main approaches to collecting photographs of ice thin sections for quantitative analysis. First and most commonly, an ice thin section is placed between stationary, crossed-polarizers and photographs are taken of the ice as the thin section is rotated azimuthally. While this technique is easy to implement, it has serious implications for image registration. First, if the line of sight is not coincident with the axis of azimuthal rotation, then eccentricity of the thin section in the image will occur. When the images are to be registered, or transformed such that all of the images contain the same orientation of the thin section, this eccentricity needs to be eliminated. Additionally, if the thin section is rotated without a fixed axis of rotation, then accidental translations can occur which also need to be eliminated. Second and ideally, image registration can be avoided altogether by having the thin section be stationary and, instead, rotating the crossed polarizers while maintaining their perpendicular privileged orientation. This procedure permits pixel-to-pixel image correspondence for precise image comparison, but requires special equipment for synchronous rotation of the crossed-polarizers. For the present study, the

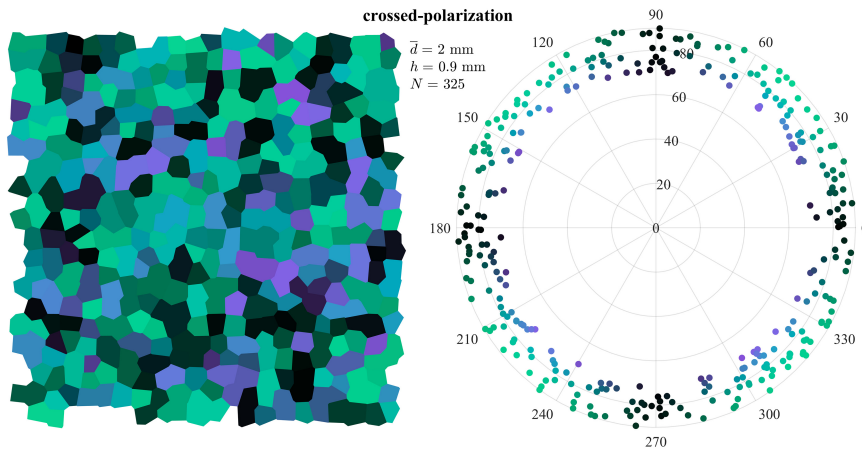


Figure 2.10: Example multi-level Voronoi diagram of representative, simulated ice fabric of S2 type ($\theta = 80 \pm 10^\circ$) in crossed-polarized backlighting with thickness h , and with quantity N ice grains with arbitrary top-level diameter \bar{d} . Right: polar plot with interference-colored points of inclination (radial) and azimuth (circumferential) angles in degrees as defined for each of the ice grains.

former technique is available and thus image registration is required for pre-processing the images for quantitative analysis. Moreover, being most common, this method is most useful to be explained for others to use for field and laboratory work.

2.3.1. IMAGE REGISTRATION

In the field of image processing, image registration refers to the process of transforming one image such that the result optimally matches a reference or target image. The transformations can include but are not limited to translation, rotation, and shear. When registering a series of images, called an image stack, one image is selected as a reference image to which all other images of the stack are registered. For image registration of the rotation of a thin section between crossed-polarizers, it is obvious that the rotation needs to be registered. But if there is an eccentricity in the axis of rotation of the thin section, or the thin section accidentally translates during rotation, then these translations need to be registered as well. Distortions in the image as a result of misalignment of the camera with the plane of rotation can occur as well, which require shear transformations to be registered. In all, simply reversing the rotations of the images may not suffice to properly register the image stack. Note again that if the crossed-polarizers are rotated about a stationary thin section, then image registration is not necessary. Image registration can be performed with photographs taken in either parallel- or crossed-polarized backlighting; it is recommended that photographs are taken under both conditions. Certain ice types may prove to be more challenging to register (e.g. horizontal section of S1 type ice) with crossed-polarization and thus easier to register in parallel-polarization.

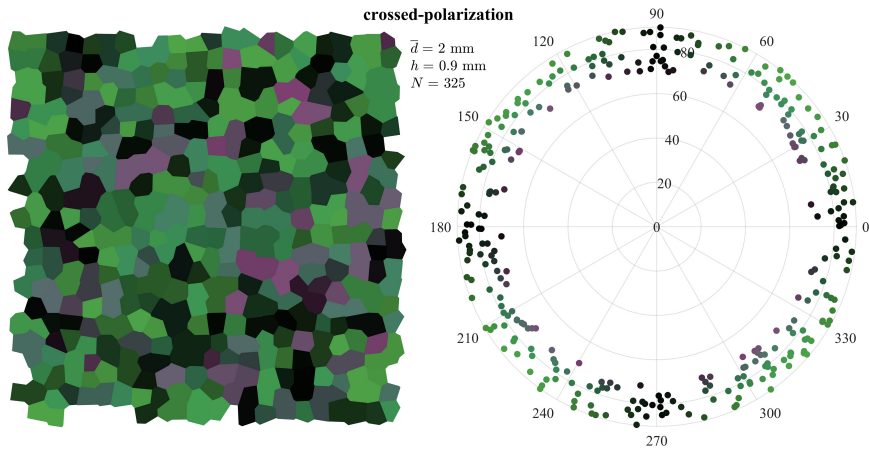


Figure 2.11: The Voronoi diagram and polar plot from Figure 2.10 with a light source color temperature of 3200 K and without chromatic adaptation (equivalent to chromatic adaptation with target color temperature of 3200 K).

2.3.2. GRAIN BOUNDARY SEGMENTATION

Once the photographs have been taken and the images have been registered if necessary, the registered image stack is chromatically adapted to 6504 K using the *chromadapt* function in MATLAB, and then can be processed to identify the grain boundaries via segmentation. This allows for identification of individual grains within which the pixels can be attributed to that particular grain from each photograph. While many different methods and approaches exist (Eicken, 1993; Gay and Weiss, 1999; Goodchild and Fueten, 1998), the following procedure was found to be most reliable for several ice types. Explanation for the image processing techniques can be found in literature (Gonzalez and Woods, 2008; Heilbronner and Barrett, 2014). First, for each image in the image stack, the image is divided into its component RGB channels (monochromatic versions of the colored image from the red, green, and blue channels). For each of these greyscale images, a Sobel filter is applied with a heuristically-determined threshold which is then scaled ad hoc. All greyscale images are then combined via Boolean multiplication. This combined image is then subjected to the following morphological operations. First, a majority neighborhood morphological operation is performed. Second, a morphological closing with a 3×3 square kernel is done. Third, the image is morphologically skeletonized. Fourth, the image is morphologically de-spurred. Finally, the image is morphologically cleaned. The boundaries of grains can then be traced using the Moore-Neighbor tracing algorithm modified by the Jacob's stopping criteria (*bwboundaries* function in MATLAB).

Regions are defined by the closed boundaries, from which the number of pixels inside each region and the shape of the boundary can be determined. Using this information and a scale in one of the reference images, the grain area, centroid, equivalent diameter, and other characteristics can be calculated. This approach is clearly more user-friendly and less biased than the manual linear intercept method commonly referred to in literature (Durand *et al.*, 2006; Snyder *et al.*, 2015). These regions each define the set of pixels from

the image stack which are used to determine the extinction of the c -axis of the grain in the azimuth and the color at brightest to be used for approximating the inclination angle. This is discussed in the next sections.

2.3.3. GRAIN AZIMUTH EXTINCTION AND ORIENTATION OF BRIGHTEST COLOR

As the image stack is the set of registered photographs which have been rotated in the azimuth by at least 90° , the variation in the intensity of each grain should expose the undulose extinction if the c -axis is not collinear with the LoS. This done by finding image with the azimuth angle resulting in the minimum color distance in the RGB color space of the color image stack for each grain, as defined by its region from the grain boundary segmentation. The color distance U_{RGB} is found as follows:

$$U_{RGB} = \sqrt{R^2 + G^2 + B^2} \quad (2.21)$$

which is the Euclidean distance in the RGB color space. Conversely, the color of each grain at its highest intensity, when $\alpha \approx 45^\circ$, can be confirmed as 45° from the extinction angle by finding the image with the azimuth angle resulting in the maximum color distance of the color image stack. This manner only finds azimuth angle of the c -axis in one quadrant of its four-fold symmetry, which cannot be distinguished with crossed-polarized light (see Figure 2.8). Important to note is the issue of deciding on a color representative of the entire grain, based on the collection of pixels in each grain. Statistical values of mean, median, mode, and maximum brightness or minimum extinction coloration are considered. The median of the color is chosen as representative for the entire grain for the analysis in Section 2.4.

2.3.4. GRAIN INCLINATION ANGLE

To determine the inclination angle in this case of azimuth rotation of the thin section only, an attempt was made to compare the interference color of each grain at its brightest with a look-up table based on the theory from Section 2.2. For a known thickness and azimuth angle, the color of the grain can be compared with a look-up table of colors associated with the range of inclination angles possible for the grain (e.g. see Figures 2.6 and 2.8). The inclination angle is selected based on the minimum color difference between the color of the grain and the interference colors of the look-up table. The minimum color difference is computed in the $L^*a^*b^*$ color space using MATLAB function *imcolordiff* based on the CIE94 standard (e.g. Melgosa, 2000).

2.3.5. *ColorIce* MATLAB TOOLBOX

The *ColorIce* toolbox of programs for registering the image stack, segmenting the grain boundaries, and generating ice texture and quarter fabric diagrams is written in MATLAB version 2021a and publically available for use at the following link: <https://doi.org/10.4121/19824067.v1>.

2.4. APPLICATION

The theory and tool are applied in three parts to demonstrate the advantages and limitations of the proposed method. The first is a comparison, conducted in the ice laboratory at the Norwegian University of Science and Technology, between the Rigsby stage technique and *ColorIce* using freshwater laboratory-grown ice. The second is the implementation of *ColorIce* for a large horizontal thin section of freshwater laboratory-grown ice which was grown in the ice laboratory at Delft University of Technology. Finally, the third part entails application of *ColorIce* to a series of horizontal sections of an ice core taken from the IJsselmeer near Breezanddijk, Netherlands in February 2021.

2.4.1. VALIDATION AGAINST RIGSBY STAGE TECHNIQUE

Freshwater ice was prepared at the ice laboratory at the Norwegian University of Science and Technology using the following techniques. First, Trondheim tap water at about 20 °C was poured into a cooler. The water was cooled at –12 °C until a thin ice surface forms, after which the ice was removed and the surface was dry-seeded with crushed ice sieved to less than 2 mm diameter. The ice was left to grow to about 120 mm, after which the ice was removed from the cooler by cutting the ice with a saw. An ice plate was cut from the ice block with a band saw to approximately 80 by 80 by 3 mm. The ice plate was polished by hand until smooth, welded to a glass plate with warm tap water, and reduced to below 1 mm with a sledge microtome equipped with vacuum pump. The thin section was placed in the Rigsby stage and a series of photographs were taken of the specimen while incrementally rotating the thin section through the azimuth by 90°.

The Rigsby stage technique (Langway, 1958; Weeks and Hibler III, 2010; Wilen *et al.*, 2003), with corrections for refraction (Kamb, 1962; Wilen, 2000), was applied to two horizontal thin sections of the seeded, freshwater columnar ice, and for each thin section 30 grains were selected and their *c*-axes were determined thrice. While the reported error of the Rigsby stage technique is 5° (Iliescu *et al.*, 2004; Langway, 1958), it was found in the present study that the mean standard deviation of the error in the inclination angles was 5.4°. Additionally, the azimuth angle for a given *c*-axis was found to occasionally vary significantly due to sensitivity in judgment as to which quadrant the *c*-axis was located based on the manipulations of the out-of-plane axes of the stage; thus, the median of the azimuth angle for each grain was chosen as representative. The results from the Rigsby stage technique were then compared with the results from *ColorIce*. Because of the four-fold symmetry inherent in conoscopic crossed-polarization used in *ColorIce*, the fabrics from the Rigsby stage technique were rotated into one quadrant for valid comparison. The inclination angles were compared directly, but the azimuth angles were compared to the minimum difference with either α or $90^\circ - \alpha$ because the complements of the angles cannot be distinguished in *ColorIce*. The mean (standard deviation in) difference in inclination and azimuth angles were found to be 11.5° (8.0°) and 2.9° (1.0°), respectively. Assuming a normal distribution in human error, these errors are comparable to those of the Rigsby stage technique and are deemed suitable for characterizing ice quarter fabrics.

2.4.2. LABORATORY-GROWN FRESHWATER ICE

Freshwater ice was prepared at the ice laboratory at Delft University of Technology using the following techniques. First, Delft tap water at about 20 °C was poured into a cooler retrofitted with a heated pressure-relief pipe connected to the bottom of the cooler. The water is cooled at -20 °C until a thin ice surface forms, after which the ice is removed and the surface is dry-seeded with crushed ice sieved to less than 2 mm diameter. The ice is left to grow to about 50 or 100 mm, after which the ice is removed by first draining the water from the cooler via a ball valve on the pressure-relief pipe and then cutting the ice from the box with a saw. The ice block is cut with a band saw to approximately 200 by 200 by 10 mm. Either this ice plate is used to seed another ice growth cycle by replacing the crushed ice (Barrette *et al.*, 1993), or the ice plate is directly used in the following manner. The ice plate is welded to an acrylic plate with warm tap water and milled level with a CNC machine. The ice plate is then removed from the acrylic and the milled surface is polished by slight melting with a hair dryer and welded to the acrylic. The ice plate is finally milled to a target thickness of 0.30 ± 0.15 mm. The thin section on the acrylic plate is placed in a polariscope and photographs are taken while incrementally rotating the thin section through the azimuth by 90°.

An example result of the method from Section 2.3 applied to a horizontal thin section of freshwater columnar ice is shown in Figure 2.12. The *c*-axes are not strictly in the horizontal plane but are randomly oriented in the range measured for the quarter fabric. Generally, the majority of the *c*-axes lie between 45° and 90° from the LoS. The accuracy of the azimuth angle is estimated at < 5° because the azimuth increments of the photographs were taken every 5°; more photographs at smaller angle increments (e.g. every 2° for a total of 44 photographs, with an accuracy of < 2°) increases the azimuth accuracy. The mean equivalent grain diameter is 10.1 mm with the largest segmented grain of around 30 mm diameter. The median of the color is chosen as statistically representative of the color within a grain at brightest azimuth angle, and is applied to the point in the corresponding polar plot.

Ideally, the colors in the polar plot should approximately match those of the interference colors as a function of inclination angle as seen in Figures 2.6 and 2.8. However, since the thickness varies across the section by an amount significant enough to change the interference color, the colors are then overlapping due to their dependence on both the inclination angle and on the thickness differences. This variation is compensated by inputting a measured thickness field (accuracy of ± 0.10 mm) into the method such that the inclination angles are determined with a specific thickness at the centroid of each segmented grain which should be representative of the true thickness of the specimen and the corresponding interference color at that location.

2.4.3. IJSSELMEER LAKE ICE

Cores of 90 mm diameter were drilled from landfast ice (salinity of < 1 ppt) which formed near Breezanddijk, Netherlands in the IJsselmeer. Analysis of two horizontal thin sections from the same core are provided, the first from about 20 mm from the ice cover surface (see Figure 2.13), and the second from about 50 mm from the surface (see Figure 2.14). The 20 mm-depth thin section displays grains with *c*-axes clustered towards nearly vertical, low inclination angles, which then tend to transition to higher inclination angles

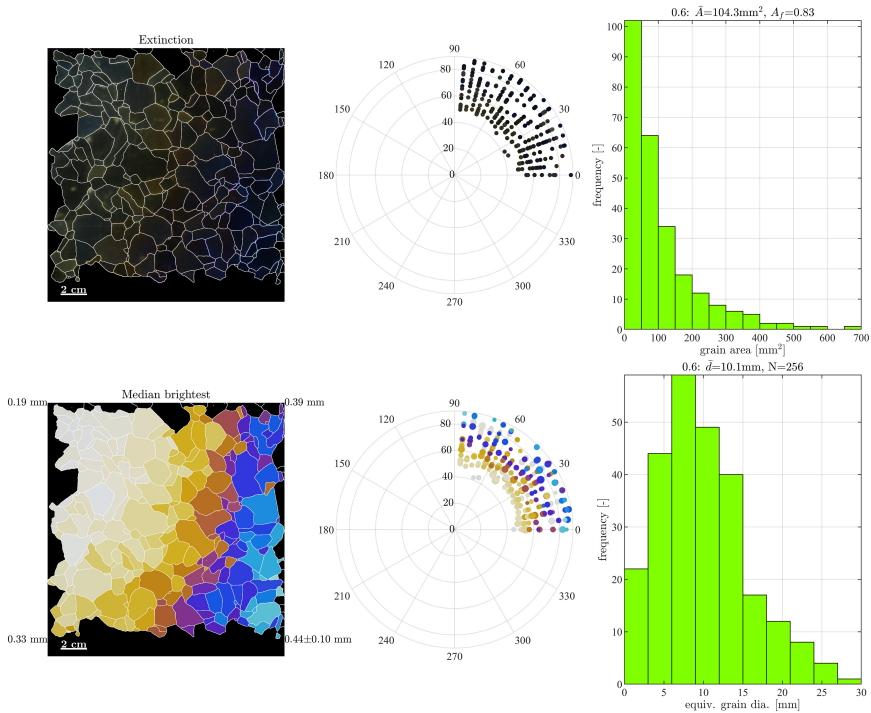


Figure 2.12: Analysis of horizontal thin section of freshwater columnar ice. Left column: composite of extinct grains at their respective extinction angles and composite of median value of brightest color of each grain. Center column: corresponding polar plots for the extinction and brightest median values of the c -axes of the grains, with the colored points scaled with grain size. Right column: distribution of grain areas and equivalent grain diameters, with mean grain area \bar{A} , area fraction analyzed of the total image area A_f , mean equivalent grain diameter \bar{d} , and number of grains analyzed N . 18 photographs were taken with 5° azimuth increments. Each registered image has 1863 by 1863 pixels, and the analyzed grains are superimposed onto the original image without azimuth rotation. The ice thicknesses and tolerance are specified at the corners of the median brightest composite image. A light source color temperature of 4000 K and chromatic adaptation to 6504 K were used.

with depth in the 50 mm-depth thin section. The azimuth angles of the c -axes show some preferential orientation around 45° at 50 mm-depth.

2.5. DISCUSSION

The *ColorIce* tool provides a method from which further developments can be made for assessment of ice microstructure. The analysis can be applied to individual photographs for preliminary grain boundary segmentation and ice texture analysis, as well as to image stacks of photographs of thin sections rotated between polarizers for complete texture analysis and quarter fabrics. For the present study, a large polariscope, a Riggsby

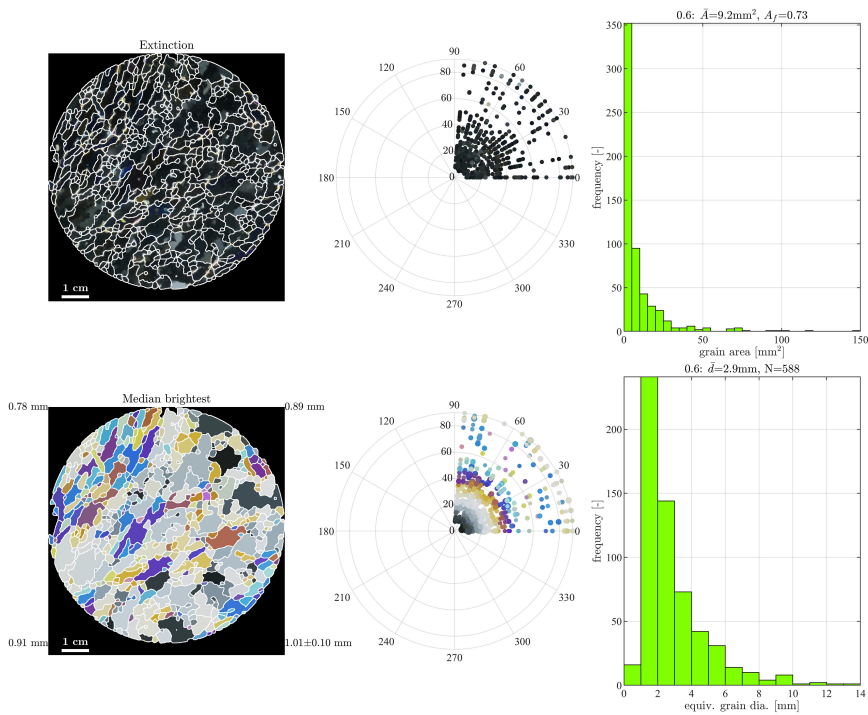


Figure 2.13: Analysis of horizontal thin section of IJsselmeer ice taken from about 20 mm from the ice cover surface. Left column: composite of extinct grains at their respective extinction angles and composite of median value of brightest color of each grain. Center column: corresponding polar plots for the extinction and brightest median values of the c -axes of the grains, with the colored points scaled with grain size. Right column: distribution of grain areas and equivalent grain diameters, with mean grain area \bar{A} , area fraction analyzed of the total image area A_f , mean equivalent grain diameter \bar{d} , and number of grains analyzed N . 18 photographs were taken with 5° azimuth increments. Each registered image has 870 by 870 pixels, and the analyzed grains are superimposed onto the original image without azimuth rotation. The ice thicknesses and tolerance are specified at the corners of the median brightest composite image. A light source color temperature of 4000 K and chromatic adaptation to 6504 K were used.

stage, and a PANASONIC LUMIX DMC-GX80 digital camera (16 megapixel sensor) with a PANASONIC MFT 12–32 mm F/3.5–5.6 lens were used, but the method permits any crossed-polarization transmitted light system setup and any digital camera with a lens that adequately captures the thin section in focus.

2.5.1. RIGSBY STAGE TECHNIQUE

While the Rigsby stage technique reveals the c -axis orientations of the grains within the full four quadrants of the stereonet, this method does not yield the ice texture. The *ColorIce* tool, at the very least, is compatible with universal stages and provides ice textures and

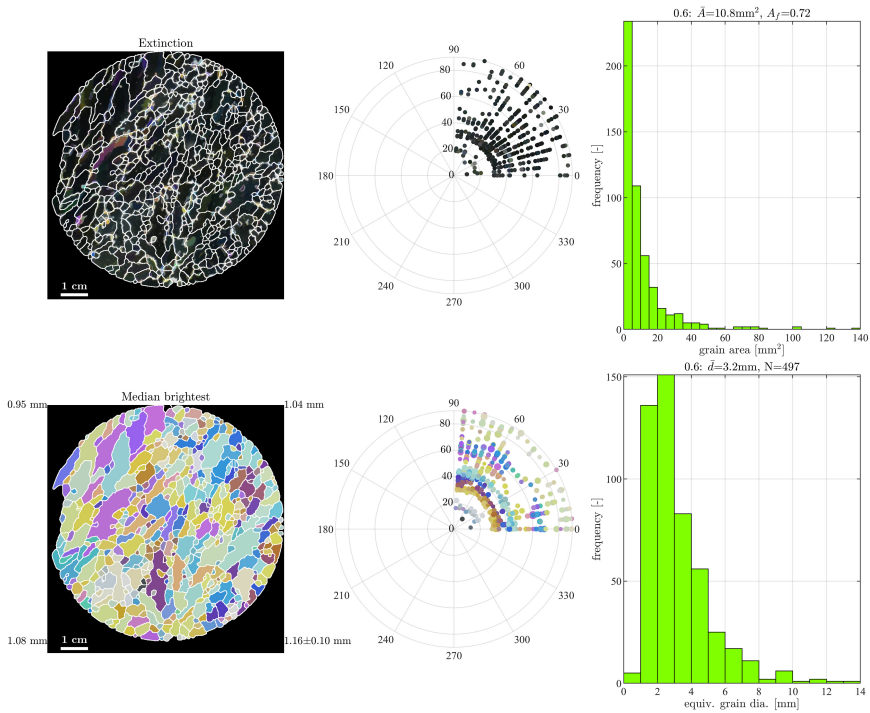


Figure 2.14: Analysis of horizontal thin section of IJsselmeer ice taken from about 50 mm from the ice cover surface. Left column: composite of extinct grains at their respective extinction angles and composite of median value of brightest color of each grain. Center column: corresponding polar plots for the extinction and brightest median values of the c -axes of the grains, with the colored points scaled with grain size. Right column: distribution of grain areas and equivalent grain diameters, with mean grain area \bar{A} , area fraction analyzed of the total image area A_f , mean equivalent grain diameter \bar{d} , and number of grains analyzed N . 18 photographs were taken with 5° azimuth increments. Each registered image has 872 by 872 pixels, and the analyzed grains are superimposed onto the original image without azimuth rotation. The ice thicknesses and tolerance are specified at the corners of the median brightest composite image. A light source color temperature of 4000 K and chromatic adaptation to 6504 K were used.

quarter fabrics for initial study. In other words, the *ColorIce* tool supplements universal stage techniques with ice textures and offers fabric information when universal stages and other specialized equipment are not available.

2.5.2. LIMITATIONS

As made clear by the polar plots in Figures 2.12 to 2.14, the quarter fabric contains c -axes with orientations only between 0° and 90° in the azimuth. This is due to the four-fold symmetry of the interference coloration theory (see Figure 2.8). More photographs of the thin sections from 90° to 180° in the azimuth would result in a repetition of the results in

each of the four quadrants. This observation does not affect e.g. relative misorientation angles between the grains within the 90° degeneracy, but does limit results when exact c -axis orientation are required for applications such as the Schmid factor.

Another limitation of automatic grain boundary segmentation is the lack of a ground truth of the image stack. The grain boundaries can be generally identified visually by an observer based on the gradient between any two grains of sufficiently different interference colors, but this does not mean there is a known solution apart from manually mapping the grain boundaries. Therefore, any result from the automatic grain boundary analysis must be deemed acceptable by the user. Regardless of the subjectivity of the user, the results are more quantitatively tractable than simply providing a photograph of an ice thin section without any statistical measure of grain boundaries, shapes, areas, or equivalent diameters.

When color-matching in the comparison with the Rigsby stage technique, it was found that in some cases the inclination angles deviated significantly (see Figure 2.15). Due to the similarity of some interference colors as a function of inclination angle (see Figure 2.6), the color matching fails to identify the correct inclination angle. In this particular case, the gold color around 35° resulted in a global minimum instead of the yellow color around 60° .

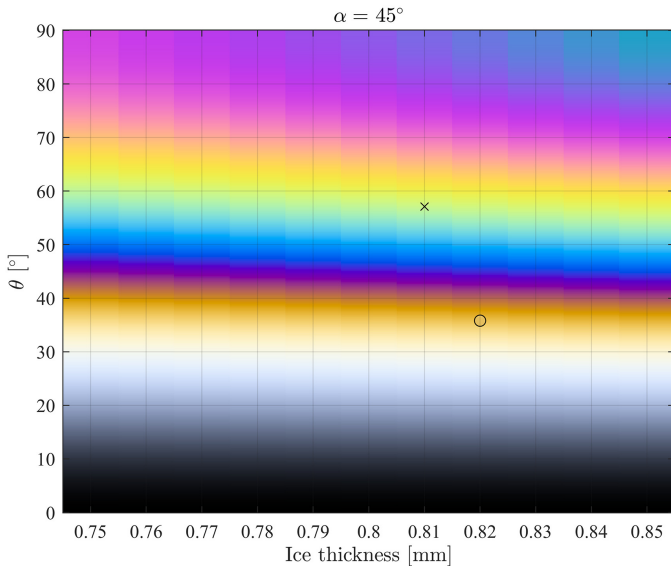


Figure 2.15: Example visualization of the color-matching algorithm for identifying an inclination angle. The circle indicates the result and the filled-in color represents the median color of the grain at maximum brightness. The cross indicates the inclination angle identified using the Rigsby stage technique. Note that ice thickness was 0.80 mm with a tolerance of 0.05 mm for relaxation in the color-matching algorithm.

The algorithms applied in the present analysis do not address the effects of cracks or impurities such as air pockets on the identification of grain boundaries and interference colors. This issue requires further development, likely incorporating manual or user-interactive intervention in the image processing techniques described previously. One of the larger impacts of impurities is the effect on the apparent thickness of the specimen in the vicinity of the impurity, namely that an air pocket means less ice thickness or variation in the thickness of a given ice grain. This discontinuity within a grain or between grain boundaries may be identified and isolated from the general analysis.

The thickness of the thin section has a major impact on the interference colors observed in the ice. Variations in the thickness on the order of 0.1 mm can be easily distinguished and can lead to errors in color matching. To avoid this error, the thickness of the thin section should ideally be measured over the whole specimen. Practically, several measurements can be made of the thickness around the edges of the specimen and the thickness field can be interpolated from the edge measurements and then used to calibrate the color look-up table when estimating the inclination angles of the grains. In this study, variations in thin section thickness are caused by 1) the levelness and thickness spatial fluctuations of the acrylic plate onto which the ice is welded; and 2) spatial fluctuations in the CNC machine axes. Another issue is the machining effects from the milling process. If the milling bit is not perfectly level, then an uneven milling pass will occur, causing a thickness difference between passes of the milling bit and visual stripes in the ice, depending on factors like rotational and translational speed. Moreover, milling grooves are also visible and can cause a cloudiness of the ice surface. These errors can be reduced slightly by melting the surface of the ice with a hair dryer, but this process is difficult to control and extreme care must be taken because over-melting can result in an even rougher surface. Polishing of the thin section surface by bare hand can also be performed, but proves challenging with large thin sections of 200 by 200 mm, especially when the ice temperature is below -10°C . Uneven wiping, fingerprints, or other blemishes can be easily caused when using the hand or fingers to smoothen the ice surface.

2.5.3. RECOMMENDATIONS

Improvement to *ColorIce* entails the addition of photographs taken with a wave plate added between the thin section and the analyzer (e.g. Heilbronner and Barrett, 2014; Peternell *et al.*, 2011; Wilen *et al.*, 2003). The wave plate reduces the four-fold symmetry of the interference coloration to two-fold symmetry based on additive and subtractive birefringence. Furthermore, if each grain possesses a dominant geometrical orientation, or clear orientation of platelet substructure as in the case of saline ice (e.g. Weeks and Hamilton, 1962), then the *c*-axis of the grain can be compared with the geometrical orientation to resolve the four-fold symmetry to two-fold symmetry. This analysis can be performed with *ColorIce* and is planned for further development. Finally, the color-matching algorithm requires adaptation to avoid misidentification of inclination angles. The mean error for the inclination angles can be markedly reduced with such an improvement.

2.6. CONCLUSION

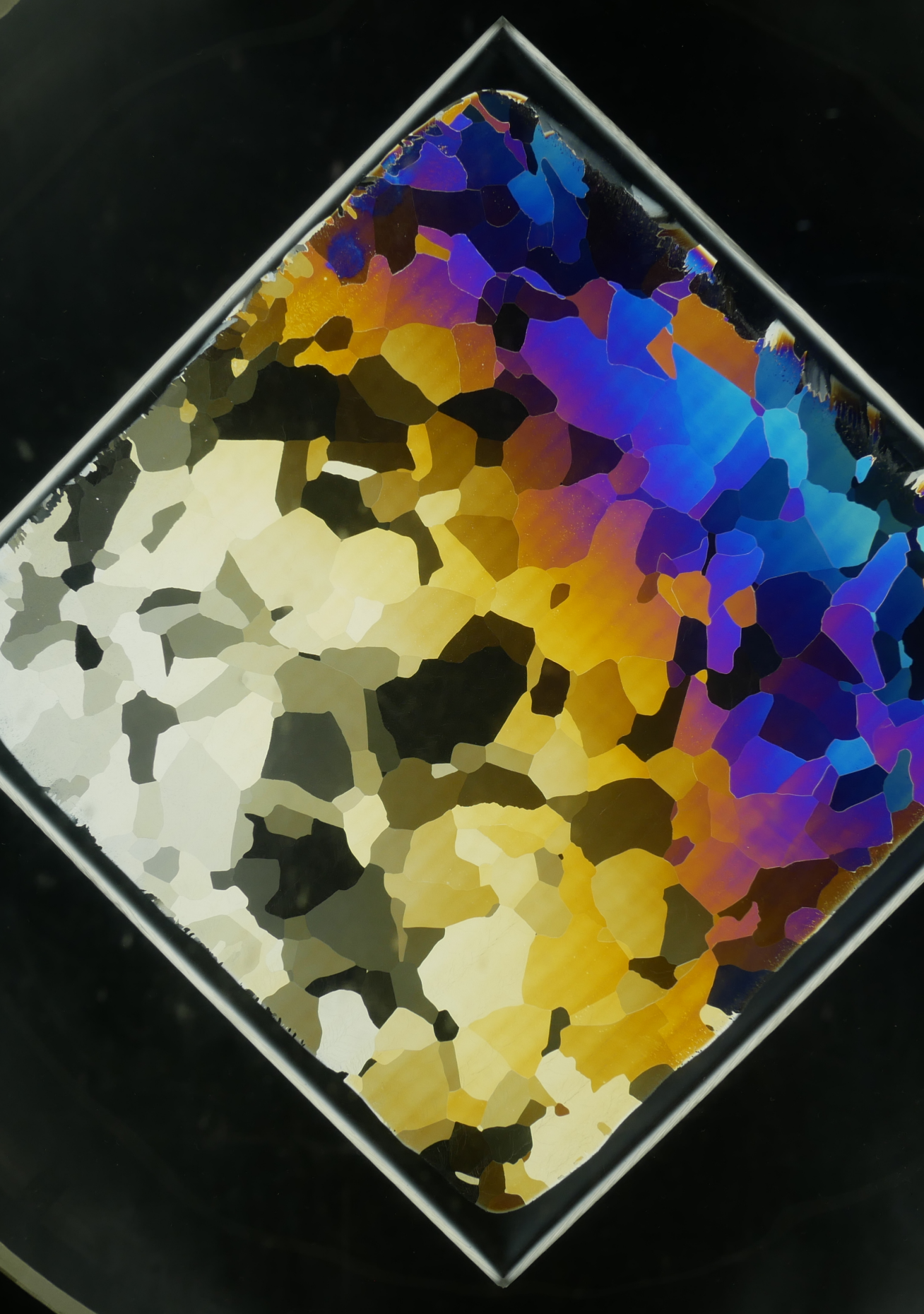
The theory of interference coloration was developed for visualization purposes and for rendering simulated ice types for identification purposes. The *ColorIce* tool based on interference coloration of thin sections was compared with the Rigsby stage technique, and example results were demonstrated for freshwater lake and laboratory-grown ice. The method is compatible with universal stages and polariscopes using any digital camera setup, and yields complete ice texture and quarter fabric diagrams for quantitative analysis. Albeit the ice fabrics are not complete, the quarter fabrics grant comparative information about relative grain orientations when universal stages and other specialized equipment are not available. With a mean standard deviation of inclination angle from the Rigsby stage technique of 5.4° , the mean (standard deviation of) inclination and azimuth errors of 11.5° (8.0°) and 2.9° (1.0°), respectively, demonstrate sufficient accuracy for *ColorIce*. Recommendations to improve the method include additional photographs with a wave plate, and developing the color-matching algorithm to avoid misidentification of similar interference colors.

2.A. REFRACTIVE INDICES FOR ICE

See Table 2.A.1 for a list of refractive indices for ice compiled from several sources.

Table 2.A.1: Refractive indices of freshwater ice as a function of visible light wavelength for the ordinary and extraordinary rays (Heilbronner and Barrett, 2014; Hobbs, 1974; Petrenko and Whitworth, 1999).

	Visible light wavelength λ [nm]	Ordinary ray refractive index n_o [-]	Extraordinary ray refractive index n_e [-]
Ice at unknown temperature (Heilbronner and Barrett, 2014)	486.134	1.31335	1.31473
	527.039	1.31140	1.31276
	535.100	1.31098	1.31242
	589.594	1.30911	1.31041
	656.281	1.30715	1.30861
	670.800	1.30669	1.30802
	686.719	1.30645	1.30775
	759.370	1.30496	1.30626
Ice at -3.6°C (Petrenko and Whitworth, 1999)	405	1.3185	1.3200
	436	1.3161	1.3176
	492	1.3128	1.3143
	546	1.3105	1.3119
	589	1.3091	1.3105
	624	1.3082	1.3096
	691	1.3067	1.3081
Ice at -3°C (Hobbs, 1974)	404.596	1.3183	1.3198
	435.806	1.3159	1.3174
	486.098	1.3129	1.3143
	491.594	1.3126	1.314
	546.090	1.3104	1.3118
	578.001	1.3093	1.3107
	589.310	1.3090	1.3104
	623.403	1.3079	1.3093
	656.297	1.3070	1.3084
	690.799	1.3063	1.3077
706.514	1.3060	1.3074	



3

HYSTERESIS AND DICHOTOMOUS MECHANICS IN CYCLIC CRUSHING FAILURE OF CONFINED FRESHWATER COLUMNAR ICE

In this chapter, laboratory experiments are described which attempted to reproduce the loading scenario experienced by a vertical section of the ice edge during the frequency lock-in regime of ice-induced vibrations. Plates of freshwater columnar ice were passively confined on the faces by glass plates and cyclically loaded on two edges by steel plates with a haversine velocity waveform while illuminated by crossed-polarized transmitted light. The results from laboratory experiments, when combined with the approach from Chapter 1, tested the hypothesis from Section 1.7 and illustrated an absence of evidence for the presence of dynamic recrystallization in ice compressive loading scenarios resembling the frequency lock-in regime of ice-induced vibrations. Instead, stress relaxation in the load, accompanied by stress-optic effects in the ice, occurred at low velocities during each cycle. These results implied mechanisms which happened below the grain scale and yield viscous behavior which are likely relevant for frequency lock-in vibrations. The stress relaxation, and a subsequent high load peak, observed in the laboratory experiments were also observed in small-scale controlled-oscillation and single-degree-of-freedom model structure experiments in an ice tank as will be discussed in Chapter 4.

This chapter has been published in *Cold Regions Science and Technology*, 2023 (Owen *et al.*, 2023a).

ABSTRACT

Cyclic crushing experiments with a haversine velocity waveform were performed on passively confined, freshwater columnar ice specimens for a variety of velocities and frequencies. The aim of the experiments was to study the ice deformation and failure behavior in crushing when loaded at a prescribed displacement pattern closely resembling the frequency lock-in regime of ice-induced vibrations. The focus of the experiments was on the development of load and ice deformation behavior at the grain and ice specimen scales during each cycle. To this end, the deformation and failure of the ice were observed with crossed-polarized light to highlight the microstructure in-situ during cyclic crushing. It was shown that there are dichotomous mechanical behaviors of the damaged and confined ice during a single crushing cycle: brittle at high velocity and non-brittle at low velocity. At low velocity, ice fracture was interrupted and stress relaxation occurred until the predefined velocity began increasing in the cycle. The stress relaxation in the load was accompanied by stress-optic effects in the ice. It was found that a load peak-velocity hysteresis developed in each crushing cycle: peak loads following the non-brittle behavior were temporarily higher than the peak loads of the brittle behavior. The temporary load peak enhancement tended to increase with increasing duration of stress relaxation, i.e. the peak enhancement tended to increase with decreasing velocity and frequency. Negligible peak enhancement and stress relaxation duration were observed for the highest frequency and mean velocity tested of 2 Hz and 10 mm s^{-1} , respectively. For tests with a minimum velocity of 1 mm s^{-1} , no stress relaxation was observed in the load measurement. Preliminary results from the experiments with a deviating haversine velocity waveform, by increasing the minimum velocity, showed that the stress relaxation duration decreases, but the non-brittle peak load does not decrease. It is speculated that anelastic ice behavior (as a function of accumulated microstructural damage) could account for the rapid stress relaxation at low velocity. It is unclear what causes the hysteresis, although it is speculated that dynamic strain aging might play a role. The change in ice behavior during the experiments demonstrates a mechanism which develops rapidly and might therefore incite the development of the frequency lock-in regime of ice-induced vibrations of vertically-sided structures.

3.1. INTRODUCTION

For the design of vertically-sided offshore structures—such as offshore wind turbines on monopile foundations—in cold regions, the scenario must be considered in which a drifting ice floe fails in crushing against the structure (ISO 19906, 2019). If the structure is sufficiently compliant at the ice action point, then the phenomenon known as ice-induced vibrations can develop. Depending on the ice drift speed and the ice thickness, among other factors, severe vibrations can develop which interfere with operability, cause fatigue damage, or even lead to failure of the structure (Björk, 1981). Therefore, accurate prediction of the development of ice-induced vibrations is important in the design of these offshore structures. Numerical modeling of dynamic ice-structure interaction serves the purpose of predicting the development of ice-induced vibrations, and requires full-scale measurements for validation. Some data exist for navigational aids (Kärnä *et al.*, 2001; Schwarz, 1994) and hydrocarbon platforms (Jefferies and Wright, 1988), but not for offshore wind turbines. To remedy this dearth of full-scale data, model-scale experiments were performed and a scaling approach was suggested which provided a benchmark dataset for dynamic ice-structure interaction of offshore wind turbine support structures

(Hammer *et al.*, 2023). However, even with these data, accurate prediction of the development of ice-induced vibrations is limited because a governing physical mechanism remains obscure. Moreover, current dynamic ice-structure interaction models are phenomenological in implementation and applicable only for structures and ice conditions which are similar to a given reference case (Hendrikse and Nord, 2019; Kärnä *et al.*, 1999). Therefore, the advancement of an understanding of the actual mechanisms that govern ice deformation and failure processes is sought to improve the accuracy in prediction of the development of ice-induced vibrations.

A physical mechanism governing ice-induced vibrations, and specifically frequency lock-in, has remained in debate ever since such vibrations were observed in Cook Inlet, Alaska (Peyton, 1968). Historically, the theories of 1) characteristic ice failure length or frequency, and 2) negative damping-based self-excitation were proposed to explain the perpetuation of severe structural vibrations (Määttänen, 1988; Sodhi, 1988). However, model-scale experimental observations of ice loads identified from a rigid pile showed that no distinct characteristic ice failure frequency occurred; instead, a distribution of frequencies developed with a median that increases with increasing ice drift speed (van den Berg *et al.*, 2022). Furthermore, the negative damping theory relies on an ice strength dependence which decreases with increasing strain or loading rate, a dependence which was neither universally observed (Cole, 2021; Hendrikse and Metrikine, 2015) nor accounted for the stochastic nature of strength in brittle failure from uniaxial compression and penetration at high strain rates (Jones, 2007; Timco, 1987).

The ductile-to-brittle transitional behavior, namely competition between creep and fracture (Schulson, 1990), of ice with respect to strain rate has been employed to describe the change in deformation and failure behavior of ice as a function of deformation rate in dynamic ice-structure interaction (Sodhi, 2001; Sodhi and Haehnel, 2003). Additionally, competition between fracture at different scales and dynamic recrystallization in high-pressure zones at the ice-structure interface have been suggested as a mechanism governing the dynamic loading in ice-structure interaction (Jordaan *et al.*, 2016; Jordaan, 2001). But neither creep nor fracture nor dynamic recrystallization as discussed in literature have been demonstrated to contribute to a governing mechanism in ice-induced vibrations. Consequently, no model based on these ice mechanics has been formulated which accurately predicts the development of frequency lock-in for various structures and ice conditions.

Results from model-scale ice penetration experiments with controlled harmonic oscillation of a pile instrumented with tactile sensors have been interpreted as having an effect of contact area variation on the load level and a delay of global ice failure during a crushing cycle (Hendrikse and Metrikine, 2016). It was found that higher peak loads resulted from longer delay of global ice failure, which were initiated by periods of low relative velocity between ice and pile. But because neither the strain nor the internal deformational behavior of the ice sheet could be measured in the edge indentation tests, a test apparatus—inspired by the confined ice crushing experiments by Gagnon and Bugden (2008)—was developed to investigate the deformation and failure behavior of ice in-situ when crushed while viewing the ice in crossed-polarized light (Owen *et al.*, 2022). By viewing the ice in-situ with crossed-polarized light, it could be verified whether and how dynamic recrystallization manifested during ice-induced vibrations. Emphasis was

placed on studying the deformation and failure behavior of full-scale or ‘real’ ice due to the uncertainty regarding the scalability of model-scale ice properties in the context of ice-induced vibrations of vertically sided structures (Gagnon, 2022).

The following research question is posed: how does the deformation and failure behavior of columnar ice develop during frequency lock-in vibrations? The objective of the present study was to reproduce the stress and strain states of the ice sheet edge during frequency lock-in vibrations in a small laboratory setting and to observe the ice mechanics involved in the interaction at the grain scale.

3

In light of the aforesaid objective, the present study employed a haversine displacement rate waveform to a passively-confined, freshwater columnar ice specimen while being filmed in crossed-polarized transmitted light. Load and velocity time series are presented with video frames, and statistical summaries are provided to illustrate trends in the results. It is shown that there were dichotomous mechanical behaviors of the damaged and confined ice during a single crushing cycle: brittle at high velocity and non-brittle at low velocity. At low velocity, ice fracture was interrupted and stress relaxation occurred until the velocity began increasing in the cycle. The stress relaxation in the load was accompanied by stress-optic effects in the ice. It was found that a load peak-velocity hysteresis developed in each crushing cycle: peak loads following the non-brittle behavior were temporarily higher than the peak loads of the brittle behavior. The temporary load peak enhancement tended to increase with increasing duration of stress relaxation, i.e. the peak enhancement tended to increase with decreasing velocity and frequency. Negligible peak enhancement was observed for the highest frequency and velocity tested. Preliminary results from the experiments with a deviating haversine velocity waveform, by increasing the minimum velocity, showed that the stress relaxation duration decreased, but the non-brittle peak load did not decrease. The results were then compared with load and velocity time histories from model-scale ice tank tests (Hendrikse *et al.*, 2022b) with controlled-oscillation of a rigid pile to demonstrate consistency of the observations for different ice types (freshwater columnar ice in the present study versus ethanol-doped granular model ice) and loading scenarios (passively confined crushing of an ice plate in the present study versus penetration of a pile through a floating ice sheet). Finally, a contribution to a physical mechanism is speculated by comparing both the results of the present study and the ice tank tests to studies establishing anelastic—defined as delayed- or visco-elastic (Cole, 2001)—behavior of ice.

The present study demonstrates novelty in two aspects. First, the application of a haversine velocity waveform—with velocities spanning several orders of magnitude during a cycle—to passively-confined columnar ice resulting in cyclic compressive failure was unique. Second, the observation of the confined ice in-situ with crossed-polarized transmitted light, highlighting deformation and failure at the grain scale, has not been reported previously. In-situ observation of confined ice with crossed-polarized transmitted light was performed only at strain rates and with ice types relevant for glaciological research (Peternell *et al.*, 2011).

The present study is structured in the following manner. The ice preparation, test setup, and experimental procedure are introduced in Section 3.2. Section 3.3 summarizes the general observations from the time series and videos. In Section 3.4, the results of the experiments are elaborated, with specific focus on two particular tests to highlight certain

features which can be generalized to the experiments. The two tests consider the effect of 1) the haversine velocity waveform on the load signal, and 2) deviation from the haversine on the load signal. The discussion is given in Section 3.5 which relates the results from the present study to research on model-scale dynamic ice-structure interaction experiments and ice anelasticity (as a function of accumulated microstructural damage). Finally, the conclusions are presented in Section 3.6.

3.2. EXPERIMENTAL SETUP AND PROCEDURE

The ice preparation and the “Optical apparatus with Linear Actuator loading Frame” (OLAF) test setup are described by Owen *et al.* (2022), but additional features have been added and are summarized here.

3.2.1. ICE PREPARATION

The ice used in the experiments was grown in the ice laboratory using tap water from Delft, Netherlands. The procedure for growing the ice was as follows. First, tap water at room temperature (about 20 °C) was poured into a cooler with dimensions of approximately 430 mm by 400 mm by 320 mm (length by width by depth, Dometic Cool-Ice CI 55, Dometic Group AB, Solna, Sweden) in the cold room which was retrofitted with a heated pressure relief system and ball valve at the base for emptying the water when desired. The cold room temperature was set at -20 °C and the water surface was left to freeze. Once a thin skim of ice formed, the ice was removed and an internally-dimensioned 200 mm cubic wooden frame was floated in the water to act as the mold for the shape and size of the ice block desired (see Figure 3.1). Inside the frame was placed either 1) crushed ice or snow sprinkled onto the surface as dry seeding; or 2) a thin ice plate cut from another ice block to act as a template seed from which the ice grain structure would follow during growth (Barrette *et al.*, 1993). The freezing process in the cooler was mainly unidirectional from the surface of the water due to the insulation from the walls and bottom of the cooler. The unidirectional cooling and the seeding process promoted columnar grain growth. The ice was left to grow for about 72 h; it was found that roughly 80 mm of ice forms in 24 h with this setup. After, for example, 72 h, roughly 185 mm of ice would have grown following the wooden frame, leaving an ideally-shaped cubic ice block nominally free from air pockets or other optical impurities. The remaining water in the cooler was drained via the ball valve and the wooden frame with ice block was cut from the surrounding ice in the cooler.

Once removed from the cooler, the wooden frame and ice block were left at room temperature of about 20 °C to thaw until the ice block separated from the wooden frame. The ice block was then cooled and cut into vertical plates of about 15 mm thickness with a band saw. Each ice plate was welded to an acrylic plate of similar size with warm tap water. While using warm water melts the bottom surface of the plate slightly, the ice that forms generally follows the grain structure of the ice plate and reduces the likelihood of grain growth emanating from the acrylic plate instead. Once welded to the acrylic, the ice plate was milled flat with a computer numerical control (CNC) milling machine. The acrylic plate was then heated so that the ice could be removed and the machined side was welded to the acrylic. Prior to welding, the machined side was heated with

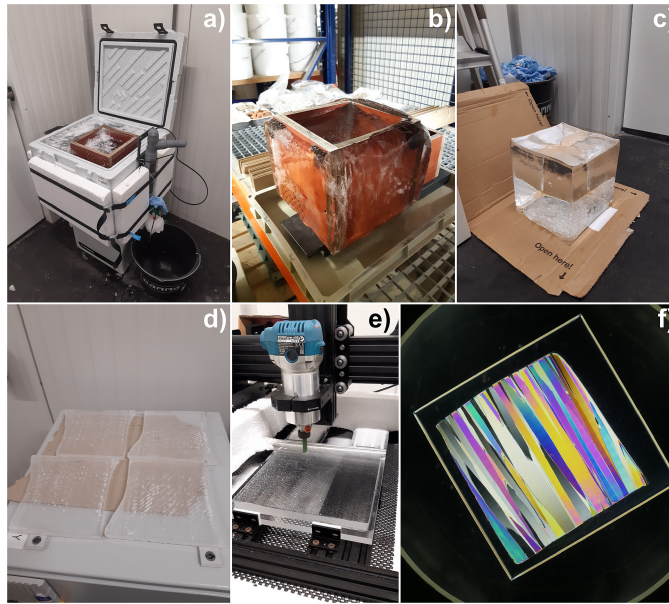


Figure 3.1: Photographic summary of the ice preparation process and assessment of grain structure: **a)** The retrofitted cooler with ice growth within the wooden frame. **b)** The wooden frame and ice block removed from the cooler and placed outside the cold room to separate the ice from the wood. **c)** The ice block removed from the wooden frame and placed in the cold room to cool. For this ice block, some air bubbles can be seen within the bottom few centimeters. **d)** The ice plates cut from the block with a band saw. **e)** The ice plate, welded to an acrylic plate, is machined with a CNC milling machine. **f)** An example thin section made from an ice plate and viewed in crossed-polarized transmitted light to assess the grain structure. Note that the photographs are representative and do not necessarily pertain to the same process of the ice preparation.

a hair dryer to melt the milling grooves and lines and promote a smoother surface for welding. Once the machined side was welded to the acrylic, the specimen was machined a target thickness of 5.20 mm with a machining tolerance of ± 0.20 mm over 185 mm and an accuracy of 0.05 mm. The ice thick section was then removed from the acrylic and the machined surface was heated with the aforesaid method, and then the uneven edges from the welding were melted flat. The ice specimen was then ready to be installed in the confinement box as explained next.

3.2.2. EXPERIMENTAL SETUP

The OLAF test setup consists of a self-contained load frame with an electric linear actuator (GSX50-1005-MKR-SB5- 358-G2ACTUATION DIVISION-EXLAR Corporation, Eden Prairie MN 55346, USA) which drives a stainless steel indenter plate into a confinement box containing the ice specimen (see Figure 3.2). Each ice specimen, a vertical thick section of columnar freshwater ice with approximate dimensions of 185 mm by 185 mm by 5 mm,

was passively confined by the confinement box and loaded on the edge by the indenter plate (see Figure 3.2b). Specifically, the ice was 1) confined by 40 mm-thick fused-silica glass plates orthogonal to the light source; 2) confined opposite the indenter plate by the steel backing plate in the direction of loading; and 3) confined by acrylic plates which were frozen in place in the aft-part of the confinement box to provide confinement upward and downward in the plane of loading to prevent splitting failure of the ice plate (see Figure 3.2c). The ice was free to deform, fracture, and clear upward and downward in the plane of loading in the fore-part of the confinement box, and was otherwise approximately rigidly confined.

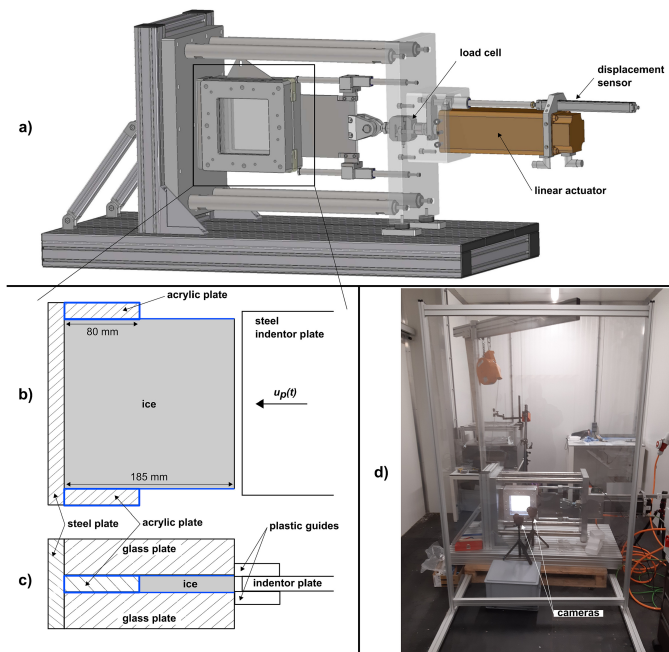


Figure 3.2: Visual description of OLAF test setup: **a)** Schematic of the OLAF test setup (Owen *et al.*, 2022). **b)** Profile view schematic of ice confinement and crushing scenario. The nominal direction and imposed displacement of the indenter plate are denoted by $u_p(t)$ and are discussed in Section 3.2.3. **c)** Top plan view schematic of ice confinement and crushing scenario. Note that the blue lines indicate the locations of weld water added for affixing the acrylic plates and ice specimen to the confinement box. **d)** Photograph of OLAF in the cold room with cameras mounted on tripods during testing.

The force was measured with a load cell (VST5000 S-type load cell, HENK MAAS Weegschalen B.V., 4264 AW Veen, The Netherlands) between the indenter plate and the linear actuator at 1 to 2 kHz. The displacement of the indenter plate was measured by a magneto-strictive displacement sensor (BIW0007-BIW1-A310-M0250-P1-S115 Balluff B.V., 5232 BC 's-Hertogenbosch, The Netherlands), also at 1 to 2 kHz, which was connected to the torque compensation rod of the linear actuator. The ice specimen was filmed at 2.7 K resolution and 50 frames per second with two cameras (GoPro HERO9

Black, 3025 Clearview Way, San Mateo, CA 94402, USA), each at a different angle and distance from the viewing window of the confinement box, in crossed-polarized light (see Figure 3.2d). The crossed-polarized light was supplied by an LED light panel (JINBEI EFP-50 BICOLOR LED PANEL LIGHT, RCP Handels-GmbH & Co. KG, in de Tarpen 42, D-22848 Norderstedt, Germany) with a linear polarizer. The cameras were fitted with linear polarizers and macro lenses for the short depth of field. All hardware, software, and non-structural equipment were adapted from another test campaign (Hammer *et al.*, 2021; Hendrikse *et al.*, 2022b).

3.2.3. EXPERIMENTAL PROCEDURE AND TEST MATRIX

For level ice drifting with a constant speed and crushing against a compliant offshore structure, structural vibrations may develop which resemble sinusoidal oscillation; this is termed frequency lock-in. During frequency lock-in, the relative velocity between the ice drift and structure oscillates between roughly double the ice drift speed and zero. To emulate this relative velocity pattern with the test setup, the indenter plate followed a haversine velocity waveform \dot{u}_p :

$$\dot{u}_p = \bar{v} [1 + \alpha \cos(2\pi f t)] \quad (3.1)$$

which is the time derivative of a constant displacement rate superimposed with a sinusoidal displacement u_p :

$$u_p = \bar{v} t + \frac{\alpha \bar{v}}{2\pi f} \sin(2\pi f t) \quad (3.2)$$

where t is time, \bar{v} is the mean velocity, α is a scale factor for the velocity amplitude, and f is the controlled frequency of the indenter plate displacement. Example time series of imposed displacement and corresponding velocity of the indenter plate and their relations to \bar{v} , f , and α are shown in Figure 3.3.

A total of 12 individual tests were performed in which \bar{v} , f , and α were varied (see Table 3.1). The mean velocities ranged from 0.4 to 10 mm s⁻¹, the frequencies from 0.2 to 2 Hz, and the scale factor from 0.5 to 1. The air temperature was $-8 \pm 2^\circ\text{C}$ for all tests, which was controlled by the refrigeration system of the cold room and locally measured with a digital temperature logger (Extech RHT30 Multi-channel data logger, Teledyne FLIR LLC, USA). The ice temperature was not directly measured, but the ice was equilibrated in the cold room for at least two hours before testing. To ensure full contact between the indenter plate and ice specimen, and improved confinement of the ice plate in the confinement box, pre-straining (deformation of the specimen prior to cyclic crushing) of 0.5% at 2×10^{-3} mm s⁻¹ was performed for all tests. Pre-straining resulted in the formation of some cracks and growth of existing cracks caused accidentally during installation of the ice specimen into the confinement box. Implications of the preexisting cracks are addressed in Section 3.2.5. The nominal crushing distance for each test was about 40 mm or 20% of the length of the specimen.

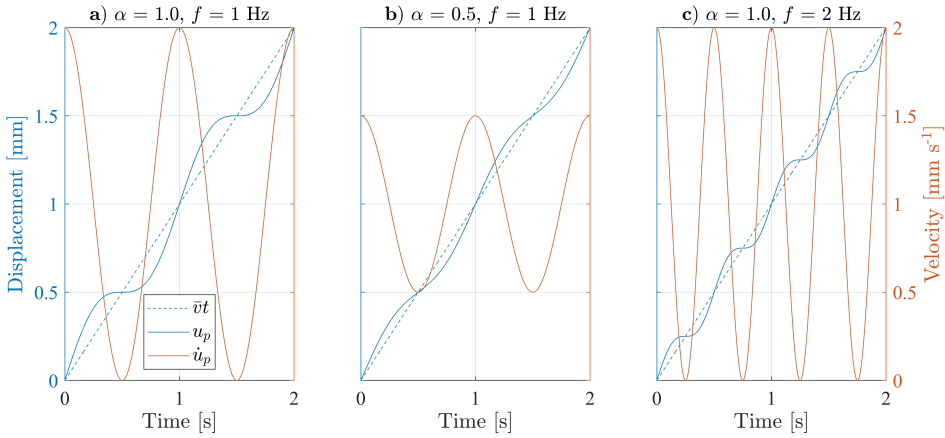


Figure 3.3: Example time series of displacement (and corresponding displacement rate, or velocity) waveform used as input to the linear actuator controller. These time series use as input $\bar{v} = 1 \text{ mm s}^{-1}$, and **a):** $\alpha = 1, f = 1 \text{ Hz}$; **b):** $\alpha = 0.5, f = 1 \text{ Hz}$; **c):** $\alpha = 1, f = 2 \text{ Hz}$.

Table 3.1: Test matrix of the cyclic crushing experiments.

Test [#]	Date	$\bar{v} [\text{mm s}^{-1}]$	$f [\text{Hz}]$	$\alpha [-]$
1	04-07-22	0.4	0.2	1
2	05-07-22	1.0	0.2	1
3	06-07-22	5.0	0.2	1
4	07-07-22	5.0	1.0	1
5	08-07-22	2.0	0.5	1
6	11-07-22	1.0	0.2	0.9
7	12-07-22	5.0	2.0	1
8	15-07-22	10.0	2.0	1
9	18-07-22	1.0	0.2	0.75
10	19-07-22	1.0	0.2	0.5
11	29-09-22	2.0	0.2	1
12	03-10-22	2.0	0.2	0.5

3.2.4. METHOD OF DATA POST-PROCESSING

The displacement measurements were filtered with an 8th order Bessel and zero-phase shift filter to reduce the significant noise from the 50 Hz power source in the data acquisition system. The velocity of the indenter plate was derived from the displacement measurements, which required additional filtering of the same type after the differentiation. The force measurements were not externally filtered. The raw videos from the GoPro cameras were compressed using a H-264 codec. The videos were visually synchronized with the force and displacement signals according the first major fracture event, or a clearer subsequent fracture event that was easily discernible from both the video and

force records.

3.2.5. IMPACT OF TEST SETUP ON MEASUREMENTS

A large scatter was observed in the mean load which contained uncertainty from differences in passive confinement of the confinement box and differences in contact area during each test. The confinement of the ice by the glass plates was not measured, and complete contact between the ice and glass plates was not guaranteed due to machining limitations for the parallelity of the ice specimen. The contact area was observed to vary significantly during the tests because of the fracture and fragmentation of the intact specimen, though contact area was not directly measured in the experiments. Moreover, cracks were formed during the installation of the ice specimen into the confinement box and acted as nucleation points for fragmentation, which formed differently for each test.

Plastic guides were used to ensure the indenter plate entered the confinement box and maintained alignment within the box (see Figure 3.2c). These guides induced frictional forces on the indenter plate of no greater than 0.3 kN, which were not subtracted since these forces were roughly the same across all tests.

It was found that the test setup was not rigid and noticeable vibrations were present in the displacement measurements. This also meant that the derived velocity signals contained vibrations of the test setup after large load drops. However, some of the recorded vibrations were likely noise from the power source, especially where the load signal did not follow these vibrations in the displacement. In cases where load drops were on the order of 1 kN or more, the indenter plate, and the test setup as a whole, underwent transient vibrations which could be clearly observed in the time series and in the videos from the shaking of the cameras. The effect of the lack of stiffness in the test setup on the test results is elaborated in Section 3.5.1.

3.3. GENERAL OBSERVATIONS FROM EXPERIMENTS

The following general observations from the experiments are supported with results from Test #2 for the sake of brevity. The time series of load and velocity for all tests can be found in the supplementary material. Synchronized videos with the load and velocity time series for all tests, as well as the raw data and post-processing techniques, are publicly available and can be found here: <https://doi.org/10.4121/22047680.v1>.

3.3.1. LOAD AND MOTION SIGNALS

All tests began with initial contact between the indenter plate and ice, typically followed by elastic loading and subsequent fracturing, consisting of numerous events, of the ice specimen when the velocity was high (see Figure 3.4). The brittle crushing failure can be characterized by linear load increases followed by sudden load drops (sawtooth-like load pattern). The first load drop was usually much higher than subsequent load drops due to the greater contact area of the ice specimen at the beginning of the test. Cracks which were initiated from the pre-straining tended to propagate and cause more cracks during the initial loading.

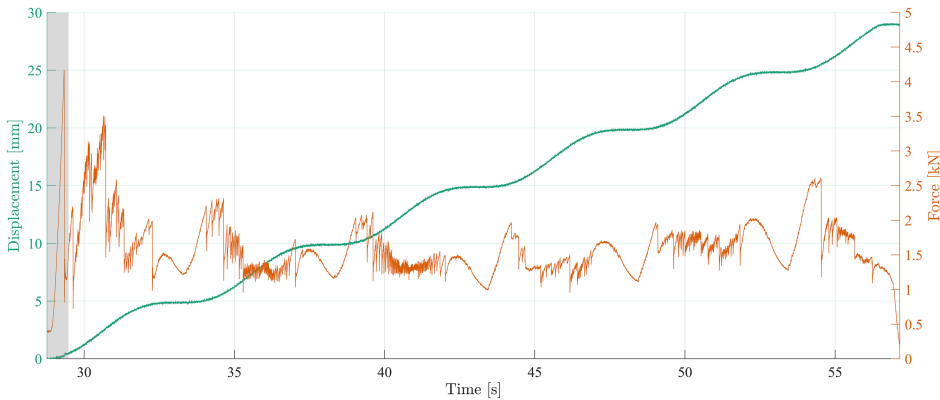


Figure 3.4: Time series of indenter plate displacement and load from the results of Test #2. The grey region delineates the initial loading and fracture.

For all tests where $\alpha = 1$ (proper haversine velocity waveform), when the velocity was relatively low and decreasing the brittle failure was interrupted and unloading of the ice specimen was observed, where the load signal became smooth (e.g. see Figure 3.5). This period of unloading (Marker 2 to 3 in Figure 3.5) was followed by reloading (Marker 3 to 4) when the velocity began increasing and typically a load build-up and fracture occurred (Marker 4 to 5), where the load prior to failure was higher than the mean of the previous brittle load peaks. This behavior was lost when significant damage developed in the ice specimen, resulting in extrusion. The load from the extrusion process was relatively smooth and low during both low and high velocity in a cycle. Damage of the ice specimen refers to a dense field of cracks without apparent separation of the intact ice into fragments.

For some tests where $\bar{v} \leq 1 \text{ mm s}^{-1}$, the latter portion of the time series showed little or no sawtooth-like load, especially when the ice specimen became uniformly damaged (see Section 3.4.5). For these tests, it appeared that the significant, uniformly distributed damage inhibited further ice fracture and instead allowed for extrusion of the damaged material.

3.3.2. VIDEOS

All individual tests were performed on vertical thick sections of columnar, freshwater ice with mean grain columnar diameters on the order of 10 to 20 mm and with nominally random orientation of the c -axes perpendicular to the growth direction (see Figure 3.6). The interference colors of each grain are defined by their c -axis orientation with respect to the crossed-polarized light, the line of sight, and the thickness of the grain (Owen and Hendrikse, 2023), with the exception of the regions near the corners of the glass plates. Unfortunately, the glass plates contained stress-induced birefringence from the manufacturing process, resulting in a superposition of birefringence of the ice sandwiched between the glass plates. Nevertheless, at the beginning of all tests, the ice specimen was loaded rapidly until brittle fracture, which was visually accompanied by a stress-induced

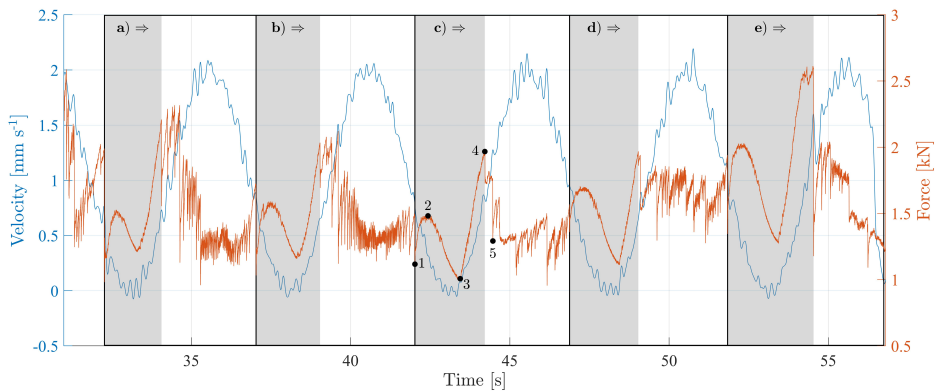


Figure 3.5: Time series of indenter plate velocity and load from the results of Test #2. Each grey region a)-e) delineates the period of low velocity and non-brittle ice behavior, with brittle ice behavior subsequently in each cycle as indicated by the arrows.

birefringence change (Ravi-Chandar *et al.*, 1994) in the ice grains (see Figure 3.7). An example of how the stress-induced birefringence change relates to the load patterns during a crushing cycle is given in the next section.

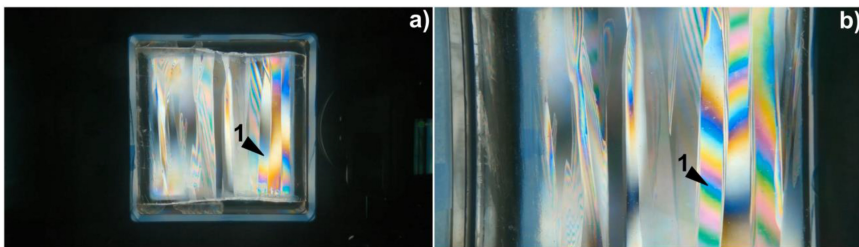


Figure 3.6: Frames from the a) global straight, and b) close-up oblique video views of Test #2 prior to loading. Indicator 1 points to the same location in both views. Note the differences in interference colors due to the difference in line of sight relative to the direction of the transmitted crossed-polarized light.

For all tests, fracture was observed at high velocity. Fracture was characterized by cracks at two scales (see Figure 3.8), one on the order of the ice specimen size (herein termed macrocrack), and the other on the order of the grain columnar diameter (herein termed microcrack). Microcracks typically emanated from macrocracks, but also occasionally developed randomly within the specimen. The microcracks propagated in clusters around the macrocracks and along grain boundaries. More specifically, the crack propagation first tended to be transgranular (macrocracks) and in the direction of loading. Those transgranular cracks were then connected by cracks propagating along grain boundaries (microcracks) which became progressively more dense with increasing deformation. The densification of microcracks with deformation eventually led to either partial or complete opacity of the ice specimen.

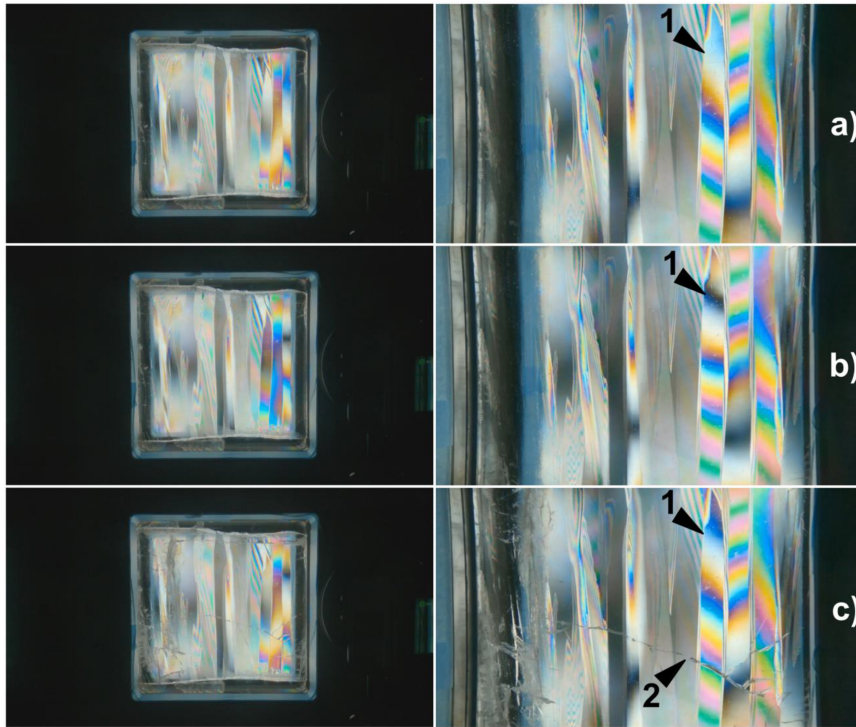
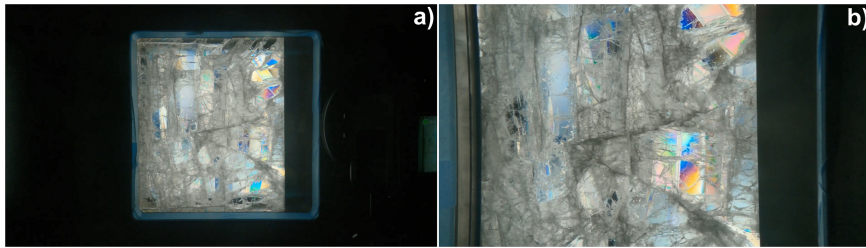


Figure 3.7: Global straight and oblique close-up video views from Test #2 with frames **a)** prior to loading; **b)** initial loading, just before fracture; and **c)** immediately after fracture. Indicator 1 points to the same location in each frame, highlighting the change in the shape and color of the interference color pattern in the grain with loading. Indicator 2 points to a large crack which unloaded the grain (compare Indicator 1 in b) and c)).

Prior to the initial, large fracture event, the could be considered as a continuum which was loaded uniformly. Following the initial fracture, the ice tended to fragment and could be considered as interacting particles. Those particles underwent comminution as deformation increased. Consequently, the fragmentation process caused loading to develop heterogeneously and fracturing to occur in localized zones.

3.4. RESULTS

The test results are presented in the form of time series, statistics, and video frames to illustrate the behavior of ice deformation and failure behavior and the corresponding load patterns. First, attention is given to one particular test for conciseness to highlight key features of the ice deformation and failure behavior, which can be generalized to all tests with a haversine velocity waveform ($\alpha = 1$). Second, trends are identified from the stress relaxation durations and load peaks of all tests with a haversine velocity waveform. Third, a test with a velocity waveform which deviated from the haversine ($\alpha < 1$) is presented to



3

Figure 3.8: Frames from the **a)** global straight, and **b)** close-up oblique video views of Test #2 at the end of testing (compare with Figure 3.6). The ice specimen has become opaque with cracks; however, some portions of grains within the ice specimen remained minimally cracked and clearly retain their interference colors.

show the effect on the ice deformation and failure behavior and consequent relaxation duration and peak loads.

3.4.1. ICE DEFORMATION AND FAILURE BEHAVIOR DURING A CRUSHING CYCLE

Using Test #2 as an exemplar of the ice behavior during individual velocity oscillations, called crushing cycles, specific features from the velocity and load time histories can be discerned and are delineated by the grey regions in Figure 3.5. During high velocity, above about 0.8 mm s^{-1} , brittle crushing dominated the load signal with sawtooth-like load drops. But during the period of low velocity—delineated by each grey region—the fracture was interrupted. The load first increased to a plateau, then decreased with decreasing velocity until the velocity began increasing again. Once velocity began increasing, or i.e. the acceleration became positive, the load immediately began increasing and continued to increase to a high velocity until fracture. The load peak at fracture was consequently higher than majority of the load peaks during the preceding brittle crushing cycle (e.g. compare Marker 4 in cycle c) to the brittle crushing of cycle b) in Figure 3.5). No significant fracture events or cracking were observed during the period in each grey region, as confirmed by the video and changes between video frames (see Figure 3.9). However, stress-induced interference color change was observed in relatively undamaged grains which were loaded and unloaded. It also appeared from the difference between video frames in the right column of Figure 3.9 that deformation at grain boundaries from Marker 1 to Marker 4 was also visible. Upon fracture between Marker 4 and Marker 5, the stress-induced birefringence did not appear to markedly change.

Strikingly, the peaks in Figure 3.5 immediately following the non-brittle behavior were higher than any other peak thereafter during the portion of the cycle with brittle behavior. This observation was consistent for all of the cycles in Test #2 after the first series of fracture in the beginning of the experiment. This observation suggested that a load-history or ‘memory’ effect, a rate-dependent hysteresis as a result of accumulated microstructural damage, contributed to the change in the peak loads following non-brittle behavior.

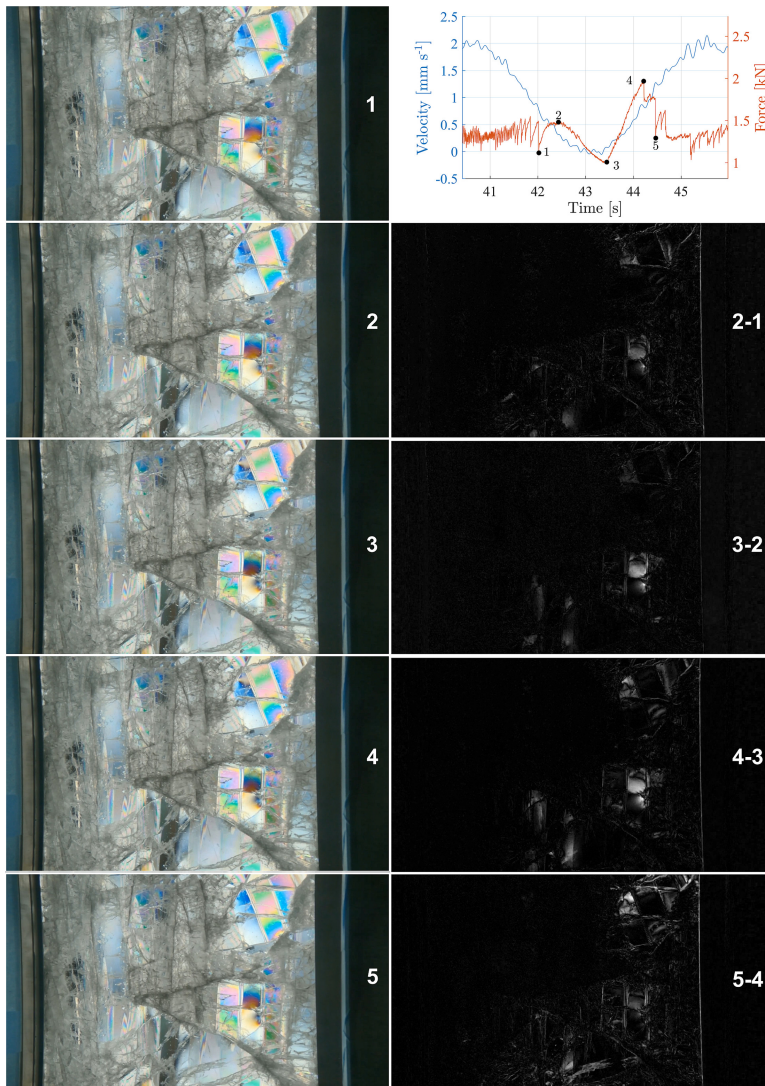


Figure 3.9: Left column: video frames (1–5) from Test #2, corresponding to the markers in Figure 3.5. Right column: greyscale difference between the video frames (e.g. 2–1 means frame 2 minus frame 1). Top right: reproduced portion of Figure 3.5.

3.4.2. EFFECT OF VELOCITY ON LOAD PEAKS DURING A CRUSHING CYCLE

To further illustrate this point, Figure 3.10 presents the peak load at fracture at the corresponding velocity for each cycle. Peaks are identified per cycle based on the MATLAB function *findpeaks* with a minimum peak prominence of 4% of the maximum load in each cycle. It can be shown that peak load at fracture varies inversely with velocity, where peak loads are higher for lower velocities. Interestingly, for cycles a) and b) in Figure 3.10,

the relation between force and velocity suggests a process which can be described qualitatively by a curve as shown in Figure 3.10f. The change in peak load varied not only with velocity but also with the duration during which the velocity was sufficiently low to inhibit fracture. For the peaks immediately following the period of non-brittle behavior, the load was higher and then appeared to reduce with the number of failure events and with time until the next period of non-brittle behavior (see Figure 3.5). It appeared that the load peak-velocity hysteresis that was gained during the period of non-brittle behavior was eventually lost during brittle crushing and was not present in subsequent crushing cycles, i.e. short-term load-history effects on the order of less than one half of a cycle (< 2.5 s in this case, Test #2). The hysteresis was clearly observed for the first two or three cycles, and was obfuscated with succeeding cycles, which was likely related to the accumulation of damage in the material.

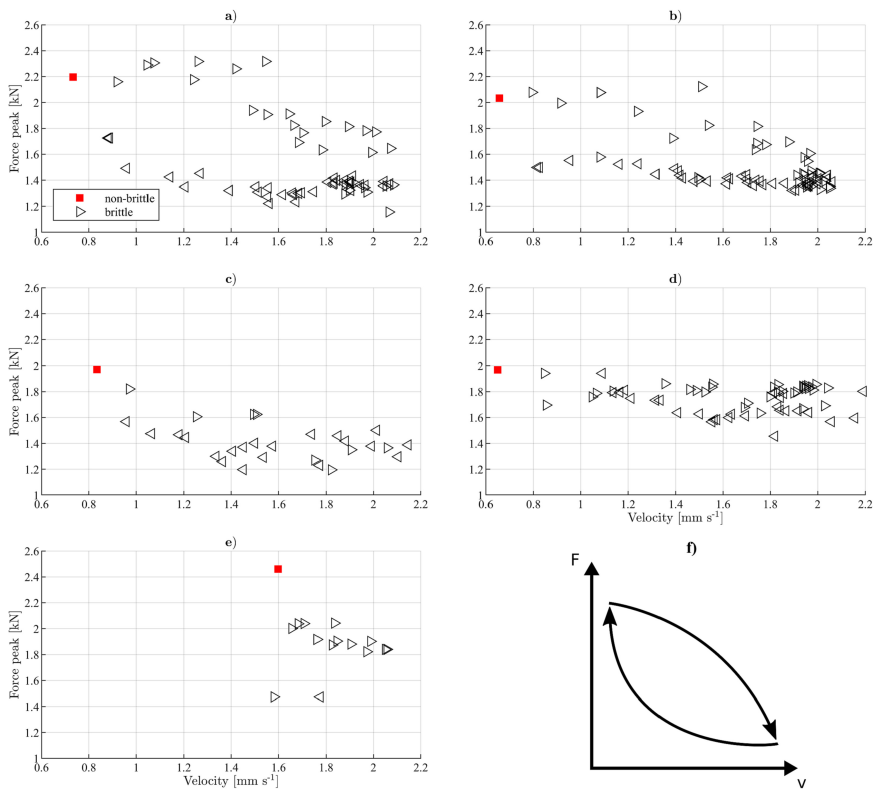


Figure 3.10: Force peaks at fracture as a function of velocity for each consecutive crushing cycle a)-e) Figure 3.5, Test #2. The force peaks following the period of non-brittle ice behavior are indicated by a red square, and the force peaks during brittle behavior are shown as a triangle. Right-pointing triangles indicate positive acceleration and left-pointing triangles indicate negative acceleration of the indenter plate. f): Observed qualitative relation of rate-dependent hysteresis between peak force at fracture (F) and velocity (v) from cycles a) through d).

3.4.3. EFFECT OF VELOCITY ON CRITICAL DEFORMATION BETWEEN FRACTURE EVENTS

Additionally, the deformation between fractures, termed critical (failure) deformation δ_f , was determined by integrating the velocity over the time between load peaks. The critical deformation values from Test #2 are plotted as a function of mean velocity between peaks in Figure 3.11. Apart from several outliers, caused by the algorithm missing failure events and thus extending critical deformation, the dichotomy in ice behavior is clear. The critical deformation during non-brittle behavior is higher than during brittle behavior, where the brittle critical deformation is roughly independent of velocity and can be fitted well with a Weibull probability distribution for Test #2 (see Figure 3.11f). The non-brittle critical deformation correlates strongly with a peak load that is mostly, though not always, higher than peak loads during brittle behavior. Comparing the ratio non-brittle to mean brittle critical deformations per cycle and averaging over the five cycles results in a factor of about 6. The results suggest that there was a change in the critical deformation between brittle and non-brittle behavior, allowing for more deformation, and thus more load, to be introduced into the ice prior to fracture.

Extending this analysis to the other tests, the effect of frequency and velocity on stress relaxation duration and peak load are investigated next.

3.4.4. EFFECT OF FREQUENCY AND VELOCITY ON STRESS RELAXATION DURATION AND PEAK LOAD

As mentioned previously, for tests where $\alpha = 1$, when the velocity was relatively low and decreasing the brittle failure was interrupted (confirmed by video inspection) and unloading of the ice specimen was observed, where the load signal became smooth. This smooth unloading was associated with a stress relaxation mechanism in the ice which prevented observable fracture and was a function of time at low velocity. Therefore, there was a frequency and velocity dependency of the relaxation, namely in the duration at low velocity. This stress relaxation duration—defined as the duration from the lowest point in the trough of the load signal during non-brittle behavior to the previous peak during non-brittle behavior (e.g. Marker 2 to 3 in Figure 3.5)—was determined for all tests. Additionally, all load peaks following the stress relaxations per cycle were identified and the previous brittle peak load was subtracted from each non-brittle load peak, denoted as ΔF . The mean of the ΔF for each test was plotted against the mean stress relaxation duration for each test in Figure 3.12. It can be seen that ΔF increases for increasing stress relaxation duration, which is a function of lower frequencies and velocities; i.e. longer durations at low velocity result in higher peak loads. Negligible peak enhancement was observed for the highest frequency and velocity tested of 2 Hz and 10 mm s⁻¹, respectively.

While stress relaxation duration increased with a decrease in frequency and velocity, it was not apparent whether the duration at low velocity or low velocity itself was contributing to ΔF . Thus, the minimum velocity was increased in some tests by altering the haversine waveform as discussed next.

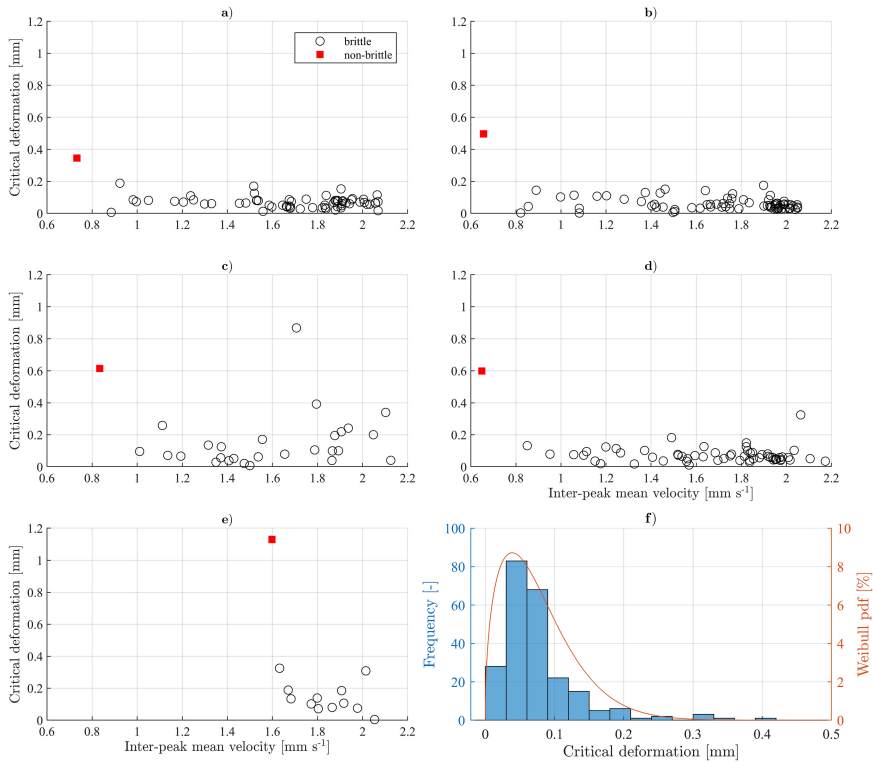


Figure 3.11: a)–e) Critical deformation between force peaks against the mean velocity between force peaks from Figure 3.5, Test #2. The critical deformation during period of non-brittle ice behavior is indicated by a red square, and the critical deformation during brittle behavior is shown as a circle. f) Distribution of all brittle critical deformation events (black circles) for Test #2, fitted with a Weibull probability distribution function ($\lambda = 0.0849$, $k = 1.4615$, $\delta_{f, brittle} \approx 0.08$ mm). Note that critical deformation > 0.8 mm were treated as outliers and omitted from the fitting.

3.4.5. EFFECT OF DEVIATION FROM HAVERSINE VELOCITY WAVEFORM ON LOAD SIGNAL

To assess the importance of the duration at low velocity or solely low velocity, several tests were performed in which the velocity waveform deviated from the haversine ($\alpha < 1$, see Equation (3.1) and Figure 3.3). In effect, this means the minimum velocity was nonzero. For these tests, it was observed that when the velocity was relatively low and decreasing the brittle failure was interrupted but unloading did not necessarily occur (see Figure 3.13). Instead, the load remained nearly constant or began increasing with a smooth signal until a fracture event occurred. Therefore, the stress relaxation duration decreased or vanished with a decrease in α for a given velocity and frequency. For example, when comparing Test #10 ($\alpha = 0.5$, Figure 3.13) to Test #2 ($\alpha = 1$, see Figure 3.5), the development of the load during non-brittle behavior with a higher minimum velocity displayed effectively no

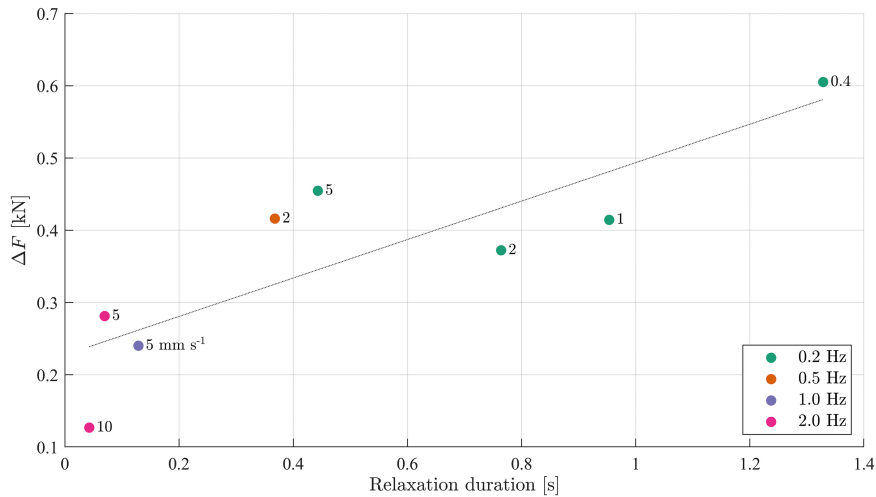


Figure 3.12: Difference between non-brittle load peak and previous brittle peak ΔF plotted against stress relaxation duration for different velocities and frequencies. Velocities are denoted by numbers next to the points, and frequencies are indicated by colors as shown in the legend. A linear trend is fitted through all data.

unloading. Instead, the load plateaued near Marker 2 in Figure 3.13 and then increased with increasing velocity. For this particular crushing cycle, due to the high minimum velocity, some microcracks were observed forming near grain boundaries, but their appearance did not result in any change in the behavior of the load pattern during non-brittle behavior (see Figure 3.14). Interestingly, from Marker 1 to Marker 3, stress-induced change in interference colors and/or deformation at grain boundaries showed clearly in the difference between video frames. This clarity was lost once the large fracture at Marker 4 appeared to dissipate the deformation at the grain boundaries.

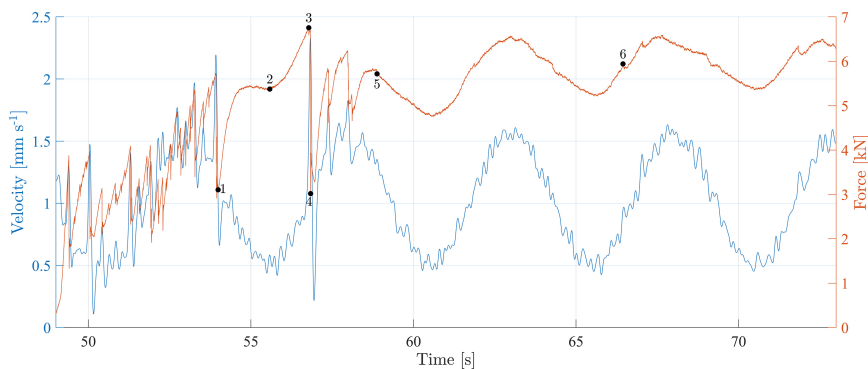


Figure 3.13: Time series of indenter plate velocity and load from the results of Test #10. The Markers 1–4 correspond to the video frames in Figure 3.14, and the Markers 5–6 correspond to the video frames in Figure 3.15

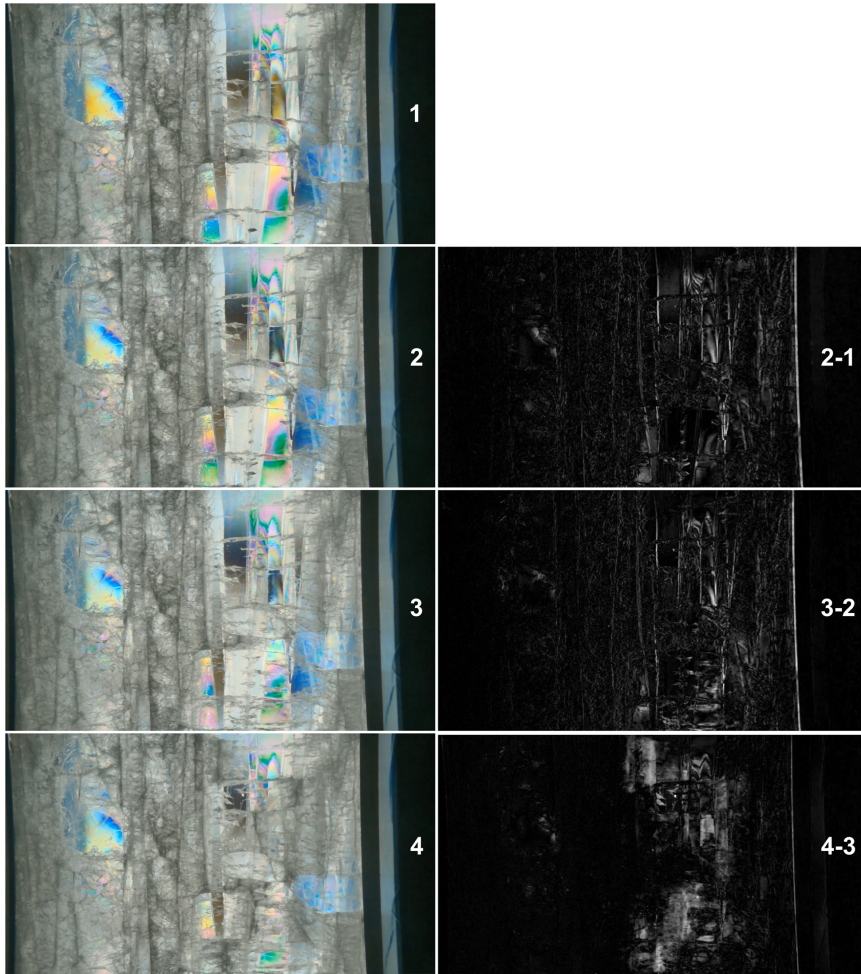


Figure 3.14: Left column: video frames (1–4) from Test #10, corresponding to the markers in Figure 3.13. Right column: greyscale difference between the video frames (e.g. 2–1 means frame 2 minus frame 1).

Curiously, after Marker 5 in Figure 3.13, the load behavior exhibited a smooth pattern following the velocity of the indenter plate, with no significant fracturing visible in the load signal. Upon inspection of the videos, it was observed that such significant damage accumulated in the ice specimen that the deformation behavior no longer showed globally brittle failure (see Figure 3.15).

It should be noted that the loads for Test #10 were higher in general than those from Test #2, but the reason for the disparity could not be clearly identified. Nevertheless, it was found that the critical deformation between Marker 1 and 3 was 2.0 mm and failure occurred at 1.6 mm s^{-1} . Comparing Test #10 to Test #2, preliminary results showed that the critical deformation was greater and fracture occurred at a higher velocity in the case

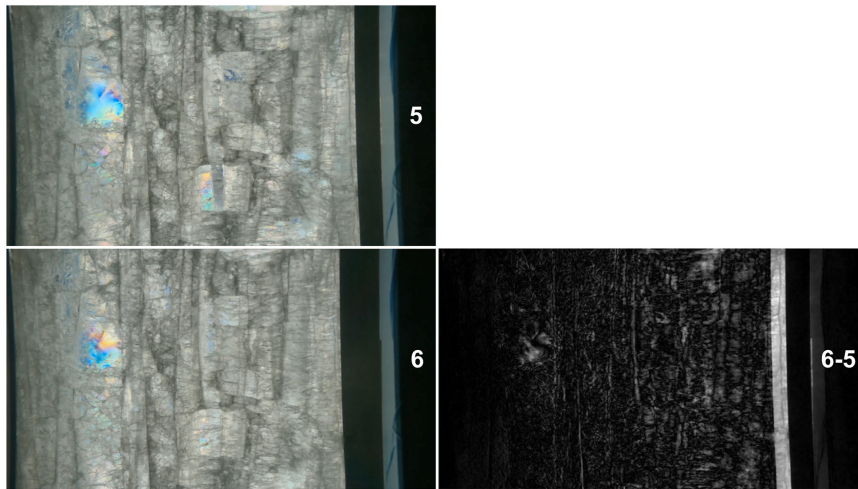


Figure 3.15: Left column: video frames (5–6) from Test #10, corresponding to the markers in Figure 3.13. Right column: greyscale difference between the video frames (e.g. 6–5 means frame 6 minus frame 5).

that the minimum velocity did not reach zero and unloading was inhibited. However, more tests are required to further address these observations and determine reliable trends.

3.5. DISCUSSION

The results shown in the present study demonstrated a dichotomy in confined, freshwater columnar ice specimen deformation behavior as a function of imposed velocity and frequency: brittle at high velocity and non-brittle at low velocity. The sawtooth-like load pattern at high velocity appeared very similar to the results from other freshwater ice crushing experiments under similar conditions (Gagnon and Bugden, 2008; Tuhkuri, 1995). As for the non-brittle behavior at low velocity, small-scale ice penetration experiments with sufficiently compliant structures (Sodhi, 1991b; van den Berg *et al.*, 2022; Yap, 2011) and controlled-oscillation experiments (Hendrikse and Metrikine, 2016) showed similar load patterns. However, according to the knowledge of the author, no other ice crushing experiments have been performed that varied the deformation rate by many orders of magnitude during a single test. Constant-rate crushing experiments, even at low velocities or strain rates, may not expose the change in ice behavior, especially the load peak-velocity hysteresis, that has been demonstrated in the present study. It should be emphasized again that the test setup was not completely rigid, which had implications for the results obtained in the present study, as discussed next.

3.5.1. EFFECT OF LACK OF TEST SETUP STIFFNESS ON RESULTS

Although the test setup was relatively rigid, this rigidity was not maintained when significant load drops occurred as previously mentioned. The major consequence of this lack of stiffness was observed in the velocity signals, which were derived from the displacement measurements. Small transient vibrations in the displacement measurements after large load drops resulted in large velocity fluctuations. These velocity fluctuations were not experienced by the ice specimen as confirmed by the absence of fluctuations in the load signals, and significant low-pass filtering was needed to clearly identify the velocity of the indenter plate after large load drops. The critical deformation values, which were calculated from the filtered velocity signals, were sensitive to the transient vibrations and the type and magnitude of filtering. The transient vibrations were superimposed on the indenter plate velocity, which occasionally led to over- or underestimations of the critical deformation between peaks (e.g. see Figure 3.11c). Given the uncertainty caused by the test setup flexibility in the velocity signals, quantitative observations from a single test were provided about the critical deformations but were not compared across tests. While the test setup was relatively compliant due to large load drops, the results showed the ice behavior to be consistent across a range of speeds and frequencies. Next, the results from the present study were compared with model-scale controlled-oscillation ice tank tests to demonstrate consistency of ice behavior for a different ice type (ethanol-doped granular model ice) and loading scenario (penetration of a pile through a floating ice sheet).

3.5.2. COMPARISON TO CONTROLLED-OSCILLATION IN MODEL-SCALE ICE TANK TESTS

In order to relate the experiments of the present study to ice-induced vibrations of offshore structures, model-scale experiments investigating ice-induced vibrations are presented and the results are compared to those of the present study. Model-scale ice tank tests with controlled oscillation of a rigid, vertically sided aluminum pile penetrated through floating ethanol ice at an air temperature of $-11\text{ }^{\circ}\text{C}$ were performed at various ice drift speeds, frequencies, and amplitudes of oscillation (Hendrikse *et al.*, 2022b). Figure 3.16 presents a sample time series of test ID 428 in which the frequency of oscillation was 0.154 Hz, the amplitude of oscillation was 11 mm, and the ice drift speed was 10 mm s^{-1} . It can be clearly seen that brittle behavior of the ice occurred at high velocity and high load peaks developed during periods of low relative velocity. Additionally, some minor stress relaxation can be seen to occur in a few cycles prior to the high load peak and global ice failure. No evidence of hysteresis can be discerned from the load signal, in comparison to the results of the present study. Nonetheless, the load pattern is surprisingly similar between the present study and the controlled oscillation in the model ice and wave tank. It should be emphasized that the model ethanol ice was rather different in microstructure and temperature profile, yet yielded such qualitatively similar load patterns, albeit at an order of magnitude higher velocity than the results from larger-grained freshwater ice.

3.5.3. REFLECTION ON LITERATURE AND ANELASTICITY OF ICE

While the observations of brittle ice behavior at high velocity and non-brittle at low velocity align with the ductile-to-brittle transitional behavior phenomenon, this phenomenon

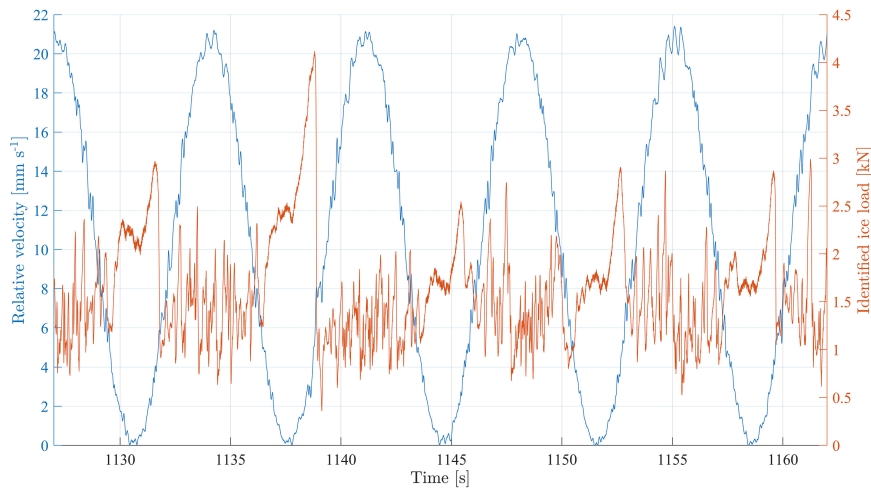


Figure 3.16: Sample time series of relative velocity and identified ice load from controlled oscillation ice tank test ID 428 (Hendrikse *et al.*, 2022b). The controlled oscillation frequency was 0.154 Hz, the amplitude of oscillation was 11 mm, and the carriage velocity was 10 mm s^{-1} .

was founded on uniaxial compression and indentation tests, each at a constant stress or strain rate of sufficient duration to expose steady-state deformation or failure behavior (Michel and Toussaint, 1977). Additionally, the experiments were generally performed on undamaged specimens and subjected to monotonic stress-controlled deformation, as opposed to the crushing cycles of the present study as a result of the haversine velocity waveform, i.e. displacement-rate-varying displacement-controlled deformation. Strain-controlled cyclic compression of ice was performed by Heijkoop *et al.* (2018), but without significant final strain or failure of the specimens. Additionally, numerous studies on uniaxial and confined, stress-controlled cyclic compression have been performed (Cole *et al.*, 1998; Cole and Durell, 1995; Iliescu and Schulson, 2002; Wei *et al.*, 2020; Wei *et al.*, 2022). However, such tests cannot be performed beyond catastrophic failure of the specimen as the stress cannot be controlled upon failure. Moreover, strain-controlled, not stress-controlled, experiments better represent the loading scenario associated with frequency lock-in vibrations. In summary, previous experiments focused on constitutive modeling of ice have not adequately captured the strain-controlled continuous crushing and cyclic failure needed for investigating the ice mechanics in frequency lock-in, and are thus unable to be directly compared to the present study.

Regarding the failure modes of the confined ice specimens in the present study, splitting in the direction of loading was suppressed and faulting became more prevalent with the added confinement of the acrylic plates, as similarly found in the literature (Wachter *et al.*, 2009). Compression experiments with cylindrical freshwater ice specimens displayed various failure modes depending on the temperature, stress state, and strain rate scenarios. For triaxial conditions, ductile-type flow developed for higher temperatures, higher confinement pressures, and lower strain rates, and shear fracturing or faulting

occurred for lower temperatures, higher confinement pressures and higher strain rates. Axial splitting occurred for lower temperatures, the lowest confinement pressures, and higher strain rates (Barrette and Jordaan, 2001; Meglis *et al.*, 1999; Rist and Murrell, 1994; Stone *et al.*, 1997). For uniaxial conditions, axial splitting dominated as the main failure mode at higher strain rates when end zones of the specimen were constrained, and shear faulting otherwise, and ductile-type flow developed at lower strain rates (Hawkes and Mellor, 1972; Jordaan *et al.*, 1992; Mellor and Cole, 1983; Schulson *et al.*, 1989; Schulson, 1990).

3

Based on the videos obtained in the present body of work, no evidence of dynamic recrystallization in the ice specimen was observed. Whether dynamic recrystallization played a role in high-pressure zones at the ice-indentor interface could not be discerned from the results as contact area, confinement, and detailed high-speed video were not available for measurements. However, it was unlikely that sufficient pressures and confinement were present to cause recrystallization as observed in triaxial compression studies (Barrette and Jordaan, 2003; Jordaan, 2001; Meglis *et al.*, 1999; Melanson *et al.*, 1999).

The mechanism of creep or viscous straining generally refers to deformation at time scales on the order of 10^3 s (Cole, 2001), which would not be relevant for the tests performed in the present study. The prospect of accelerated or enhanced creep in the tertiary regime from microcracking at high homologous temperatures (Jordaan *et al.*, 1992; Sinha, 1989) might aid in explaining whether creep in the ductile-to-brittle transition can participate at time scales relevant for frequency lock-in vibrations of structures with natural periods on the order of 1 s.

Due to stresses and the significant damage in the ice during the experiments, and especially at high homologous temperature ($T_H = 0.97T_{mp}$ in the present study, where T_{mp} is the melting point of freshwater ice), cohesion and the possibility of rapid crack healing via sintering may be involved (Murdza *et al.*, 2022; Szabo and Schneebeli, 2007). However, it was not possible to accurately measure temperature changes throughout the specimens in the present study.

In the present study, a hysteresis was observed in the load behavior, which appeared to develop in the ice as a result of the duration at low velocity, followed by rapidly increasing the velocity. This load peak-velocity hysteresis, and the dichotomy in ice behavior, might be explainable using a framework of dislocation-based mechanics (Cole, 2021; Schulson *et al.*, 2019). The load-history effect, and possible strengthening, may relate to back stresses as observed in cyclic flexure of ice beams (Murdza *et al.*, 2020; Murdza *et al.*, 2021b) and developing as a result of high stress and stress rate during the unloading and reloading in the non-brittle period. Evidence for higher stresses upon reloading in a roughly similar manner as in the present study have been observed in a yield phenomenon in cold single crystals of metals (Haasen and Kelly, 1957) and in dynamic strain aging of polycrystalline metals (Ren *et al.*, 2017).

The dichotomy in ice behavior might be explained by anelastic ice properties of dislocation and/or grain boundary relaxations competing rapidly (< 2.5 s) in time at crack tips to delay fracture when sufficient time and stress are present to produce and mobilize dislocations and/or cause grain boundary sliding (Cole, 1995; Cole, 2020). Although this mechanism is described by Schulson and Duval (2009) as the competition between creep

and fracture in the ductile-to-brittle transition, the term creep connotes large time scales which are not applicable in this context. Thus, it is clarified here that anelasticity (as a function of nontrivial permanent strain), not creep, manifests in the competition with fracture.

3.5.4. APPLICATION TO THE FREQUENCY LOCK-IN REGIME

The crushing regime of ice-induced vibrations called frequency lock-in, at least for a single-degree-of-freedom oscillator, is characterized by a near-sinusoidal structural response. In frequency lock-in, during the period of low relative velocity between ice drift and structure, the global ice load typically shows a peak greater than those during high relative velocity. Moreover, the brittle load pattern at high relative velocity is mostly absent from the period of low relative velocity (van den Berg *et al.*, 2022). It is speculated that the results from the present study and the observations of frequency lock-in vibrations from small-scale experiments may be governed by the same mechanism: dislocation mechanics. The dislocation mechanics are involved in anelasticity and back stress, which are responsible for the change in ice behavior during the period of low relative velocity between ice and structure and the subsequent high peak load. The global load during low relative velocity can transfer more energy to the structure in that part of the cycle than can be extracted during brittle crushing in the rest of the cycle. This mechanism can sustain frequency lock-in vibrations, but is self-limiting in terms of the structural velocity. When more energy is transferred to the structure than is needed to sustain the near-harmonic response, the structural velocity greatly exceeds the ice drift speed, which causes unloading of the structure as the structure loses contact with the intact ice sheet. As long as the structural velocity does not greatly exceed the ice drift speed, the ice conditions remain stable, and the duration of low relative velocity is sufficiently long to delay fracture and cause a following high load peak, sustained vibrations can develop. While this description follows the established frequency lock-in velocity relation (Toyama *et al.*, 1983), it again implicitly suggests the inclusion of a duration component which depends on the natural frequency of the structure (Hendrikse and Metrikine, 2016). Finally, the hysteresis of the load increase after a duration of low relative velocity could be considered in research on ice-induced vibrations of vertically sided structures, a critical observation which should be further studied.

The new results in the present study are significant because they demonstrate that the ice-induced vibrations problem, and specifically frequency lock-in, requires ice to be treated as a loading-history, and thus time-dependent, material at short time scales, which contradicts the assumptions of some numerical ice models (Gagnon, 2022; Matlock *et al.*, 1969) and dimensional analyses (Korzhasin, 1962; Palmer *et al.*, 2010). The implications in practice for these results are that such numerical ice models and dimensional analyses may yield inaccurate predictions of the development of ice-induced vibrations, and only models which consider ice as a loading-history-dependent material at short time scales may be able to grant accurate predictions (Hendrikse *et al.*, 2018; Huang and Liu, 2009; Kärnä *et al.*, 1999).

The present study and the research on anelasticity would suggest that some of the processes involved in the development of ice-induced vibrations occur at scales smaller than the grain. This finding is encouraging for further research in dislocation mechanics

during cyclic compressive loading of ice. The scaling of loads and motions in ice-induced vibrations could benefit from the findings with further investigation of viscosity in ice and dislocation-based mechanics.

3.6. CONCLUSION

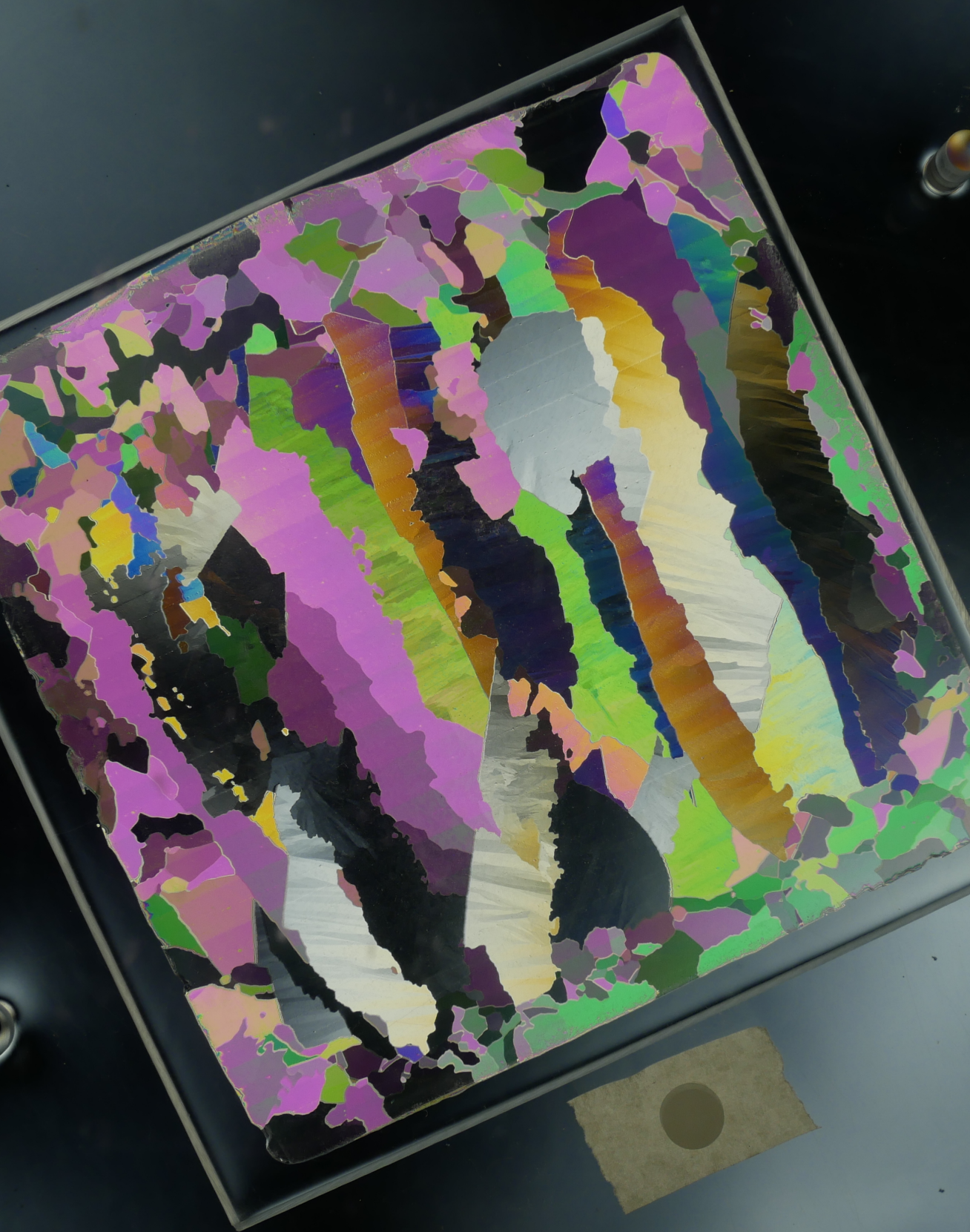
Cyclic crushing experiments with a haversine velocity waveform were performed on passively confined, freshwater columnar ice specimens for a variety of mean velocities (0.4 to 10 mm s⁻¹) and frequencies (0.2 to 2 Hz). The aim of the experiments was to study the ice deformation and failure behavior in crushing when loaded at a prescribed displacement pattern closely resembling the frequency lock-in regime of ice-induced vibrations. The focus of the experiments was on the development of load and ice deformation behavior at the grain and ice specimen scales during each cycle. To this end, the deformation and failure of the ice were observed with crossed-polarized light to highlight the microstructure in-situ during cyclic crushing.

Based on the results presented in this study, the following conclusions can be made:

1. The cyclic crushing of confined, freshwater columnar ice demonstrated dichotomous deformation behavior: brittle at high velocity and non-brittle at low velocity.
2. At low velocity, ice fracture was interrupted and stress relaxation occurred until the velocity began increasing in the cycle. The stress relaxation in the load was accompanied by stress-optic effects in the ice.
3. A load peak-velocity hysteresis developed in each crushing cycle: peak loads following the non-brittle behavior were temporarily higher than the peak loads of the brittle behavior.
4. The temporary load peak enhancement tended to increase with increasing duration of stress relaxation, i.e. the peak enhancement tended to increase with decreasing mean velocity and frequency. Negligible peak enhancement and stress relaxation duration were observed for the highest frequency and mean velocity tested of 2 Hz and 10 mm s⁻¹, respectively.
5. For tests with a minimum velocity of 1 mm s⁻¹, no stress relaxation was observed in the load measurement.
6. Preliminary results from the experiments with a deviating haversine velocity waveform, by increasing the minimum velocity, showed that the stress relaxation duration decreased, but the non-brittle peak load did not decrease.
7. It is speculated that anelastic ice behavior (as a function of accumulated microstructural damage) could account for the rapid stress relaxation at low velocity.
8. It is unclear what causes the hysteresis, although it is speculated that dynamic strain aging might play a role.¹

¹It was later found that dynamic strain aging does not occur in ice (Weiss, 2019).

9. The change in ice behavior during the experiments demonstrates a mechanism which develops rapidly and might therefore incite the development of the frequency lock-in regime of ice-induced vibrations of vertically sided structures.



4

PEAK LOADS DURING DYNAMIC ICE-STRUCTURE INTERACTION CAUSED BY RAPID ICE STRENGTHENING AT NEAR-ZERO RELATIVE VELOCITY

In this chapter, results are presented from a series of ice penetration tests in an ice tank with a rigid structure, with controlled oscillation, and with a single-degree-of-freedom structure which were used to investigate the peak load-velocity dependence for ethanol-doped model ice. It was found that a rapid strengthening of the ice developed at low relative velocity and carried over to high relative velocity until the ice failure dissipated the strengthening effect. The strengthening effect, observed in the rigid structure and controlled-oscillation tests, was also observed during frequency lock-in and intermittent crushing in the single-degree-of-freedom structure test. The results from the controlled-oscillation tests and frequency lock-in of the single-degree-of-freedom structure test strongly resembled the experimental results from Chapter 3. Specifically, stress relaxation at low relative velocity and a subsequent high load peak, referred to as strengthening, were observed in both the laboratory and ice tank settings. The similarity in findings across ice types and loading scenarios gives support to the postulation that common mechanisms operate within the ice which govern the development of ice-induced vibrations.

ABSTRACT

A series of ice penetration tests with a rigid structure, with controlled oscillation, and with a single-degree-of-freedom structure was performed to investigate the peak load-velocity dependence for ethanol-doped model ice during a test campaign at the Aalto Ice and Wave Tank. For the rigid structure and controlled-oscillation tests, the ice drift speed ranged between 1 and 150 mm s⁻¹. In the controlled-oscillation tests, amplitudes of oscillation between 0.40 and 15.90 mm and frequencies of oscillation between 0.143 and 4 Hz were prescribed such that the relative velocity between ice and structure never became negative. A constant ice drift deceleration experiment with a single-degree-of-freedom structure was performed to investigate the development of frequency lock-in and intermittent crushing in the model ice and compare the results with the rigid structure and controlled-oscillation tests. It was found that the peak load-velocity dependence identified in the rigid structure tests was not always uniquely defined as identified in the controlled-oscillation tests because the loading history affected the peak load at ice failure. A rapid strengthening of the ice developed at low relative velocity and carried over to high relative velocity until the ice failure dissipated the strengthening effect. The strengthening effect, observed in the rigid structure and controlled-oscillation tests, was also observed during frequency lock-in and intermittent crushing in the single-degree-of-freedom structure test. The observations in the present study indicate that the so-called velocity and compliance effects in ice-structure interaction originate from the same strengthening effect. It then follows that peak loads on compliant structures cannot exceed peak loads on rigid structures in the same ice conditions, with the only difference being that the peak loads on compliant structures occur at apparently higher far-field ice drift speeds due to the change in relative velocity.

4.1. INTRODUCTION

The magnitude of ice loads during indentation is known to be dependent on the relative velocity between ice and structure, or rate of loading, of the ice. This ‘velocity effect’ has been observed in experimental campaigns (Izumiyama *et al.*, 1994; Kamesaki *et al.*, 1996; Kärnä *et al.*, 2008; Määttänen, 1981; Singh *et al.*, 1990; Sodhi, 2001; Tsuchiya *et al.*, 1985) and in full-scale as first shown by Peyton (1968) and later summarized by Jefferies *et al.* (2008) for multiple offshore structures. It has also been proposed that there exists a ‘compliance effect,’ related to the observation that loads during intermittent crushing on a flexible structure are typically higher than the loads on a rigid structure for the same far-field velocity (Kamesaki *et al.*, 1996; Kärnä *et al.*, 2008). A typical peak load-velocity curve as presented in Singh *et al.* (1990) is shown in Figure 4.1, demonstrating both the velocity effect and the compliance effect.

The negative slope in the peak load-velocity dependence is often interpreted as a source of ‘negative damping’ and related to the development of ice-induced vibrations of compliant structures. Models for prediction of ice-induced vibrations sometimes assume a one-to-one (bijective) relation between peak load and velocity (Hetmanczyk *et al.*, 2011; Kärnä, 1992; Määttänen, 1998; Withalm and Hoffmann, 2010). The definition of this relation is somewhat challenging though, given that the compliance effect requires the curve to be shifted with velocity for changes in mass, natural frequency, and damping of the structure. In modeling this is, for example, accounted for by shifting the position of the negative gradient along the velocity axis based on natural frequency of the structure (Huang and Liu, 2009). Ultimately, the question remains whether the peak load-relative-

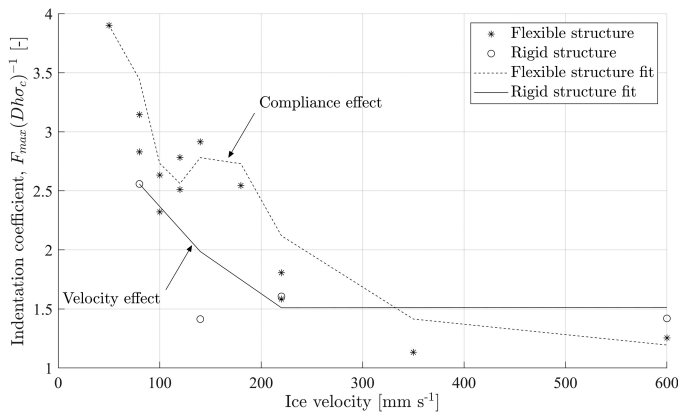


Figure 4.1: Data replotted from Singh *et al.* (1990) showing the ‘velocity effect’ and ‘compliance effect.’ The indentation coefficient is defined as maximum excitation force F_{max} divided by width D , thickness h , and (uniaxial) compressive strength σ_c . The fitting is performed by applying a moving average, with window of two data points, using the mean indentation coefficient at each ice velocity.

velocity relation in ice-structure interaction has a linear dependence on the stress-strain-rate relation as observed in uniaxial compression of ice.

Even when accounting for the compliance effect in defining the peak load-velocity dependence, there is a question if a bijective relation between peak loads and velocity is correct. Controlled-oscillation experiments (Hendrikse and Metrikine, 2016) showed indications that the loading history affects peak loads, though challenges with control and the absence of rigid penetration experiments did not allow firm conclusions to be drawn. Another question of relevance is if peak loads on a compliant structure can exceed those at the lowest speeds on rigid structures, or if the compliance effect is merely a different manifestation of the same effect responsible for the velocity effect as seen for rigid structures.

In the present study, results are introduced from ice penetration tests with a rigid structure and with controlled oscillation which were performed with the aim to answer two questions. First, does a load-history dependence exist for the peak load-velocity relation during ice penetration? Second, do the velocity effect and compliance effect originate from the same effect? Experiments with a single-degree-of-freedom (SDOF) structure were also conducted to investigate ice-induced vibrations in the same model ice as the rigid and controlled-oscillation tests. The results from the penetration experiments performed with the rigid structure, controlled oscillation, and SDOF structure in the present study show that peak loads depend on the amount of time spent at low relative velocities where a strengthening of the ice can develop. The term ice strengthening is herein defined as the consistent increase in mean and peak global ice-induced loads due to loading history.

The present study is structured as follows. Section 4.2 introduces the test campaign with a focus on the hybrid test setup used, the model ice properties, and the different

types of tests conducted. Section 4.3 establishes the peak load-velocity dependence for the model ice based on rigid structure ice penetration tests. Section 4.4 establishes the peak load-velocity dependence from controlled-oscillation experiments and investigates the load-history effect. Section 4.5 shows the results from constant deceleration tests with a SDOF structure where the load-history effect appears during frequency lock-in (FLI) and intermittent crushing (ICR). The discussion, in Section 4.6, focusses on the effect of compliance on the load-velocity dependence, an explanation for the strengthening effect from the literature, and the representativeness of model ice as a substitute for naturally occurring or full-scale sea ice.

4.2. TEST CAMPAIGN DESCRIPTION

4

The experiments analyzed in the present study were part of a large test campaign in the SHIVER project conducted at the Aalto Ice and Wave Tank. The tank is a 40 m by 40 m indoor facility where experiments with floating freshwater and ethanol-doped ice can be conducted. In the SHIVER campaign, which included the tests analyzed herein, ethanol-doped ice was used. Hendrikse *et al.* (2022b) give a detailed description of the experimental design, and materials and methods. The following sections summarize the most relevant information for the analysis in the present study.

4.2.1. TEST SETUP

The real-time hybrid test setup combined mechanical and numerical components to allow for tests with a rigid structure, controlled-oscillation tests, and simulation of structural models in real-time (e.g. Hammer *et al.*, 2022; Hammer *et al.*, 2021; Hammer *et al.*, 2023; Hendrikse *et al.*, 2022a; Hendrikse *et al.*, 2022b; van den Berg *et al.*, 2022). Figure 4.2 shows a photograph of the setup during testing and gives a schematic overview of the setup components. A rigid, cylindrical aluminum pile with a diameter of 200 mm penetrated the ice sheet. Ice-induced loads were identified from pile strains, which were measured with strain gauges located above the ice action point. The structural displacement at the ice action point was applied to the pile by bi-directional linear actuators. The pile displacements matched either the prescribed displacements of controlled oscillation or the calculated displacements of a simulated structure at the ice action point. In the case of a SDOF structure test, the response of the simulated structure to the measured ice-induced loads was numerically simulated on a microcontroller. The pile displacements were measured by displacement sensors. In the tests described in the present study, only pile displacement in the ice drift direction was modeled (y-direction as indicated in Figure 4.2; cross-drift or x-direction was immobilized).

The real-time hybrid test setup was mounted to a carriage. The carriage was mounted to a bridge spanning the ice tank. The bridge was stationary for each test. Ice drift was achieved either 1) by moving the carriage along the bridge with prescribed speeds (5 mm s^{-1} to 150 mm s^{-1}); or 2) by the actuator, with the carriage stationary, for low speeds on the order of 1 mm s^{-1} for the rigid structure tests (1 mm s^{-1} to 10 mm s^{-1} , see Table 4.A.1, Table 4.A.2, and Table 4.A.3). The resulting apparent ice drift was then opposite to the carriage movement direction or the actuator movement direction when the carriage was stationary. In the present study, movement of the carriage, or the actuator

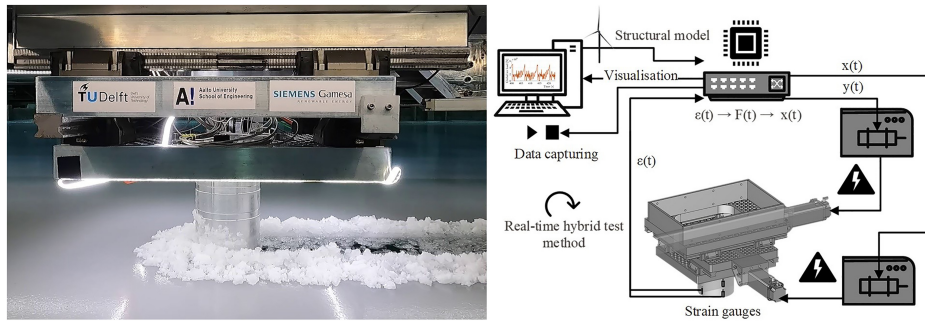


Figure 4.2: Left: Photograph of the real-time hybrid test setup during testing, showing the cylindrical pile interacting with the ice. Right: Schematic overview of the real-time hybrid test setup, with strain in the pile ϵ , identified ice-induced load F , direction of ice drift y , and cross-drift direction x , all as a function of time t (Hammer *et al.*, 2021).

movement when the carriage was stationary for the rigid structure tests, is referred to as ice drift. The real-time hybrid test setup is referred to as the structure. The measured pile displacements relative to the carriage supporting the real-time hybrid test setup are termed the structural displacements.

During the tests, the global ice-induced loads and structural responses were measured with load cells, strain gauges, accelerometers, and displacement sensors. The analyses introduced in the present study use the externally-unfiltered global ice loads as identified by the strain gauges. The reader is referred to Hendrikse *et al.* (2022b) for more information about the real-time hybrid test setup.

4.2.2. MODEL ICE

The model ice was created by spraying a fine mist of a water-ethanol mixture on a thin layer of initial ice, according to the following procedure: 1) Lower the tank temperature to -10 °C. 2) Remove the ice that has formed on the basin surface. 3) Refreeze the water surface for 20 min, forming a smooth, thin layer of ice. 4) Spray mist at -10 °C for 180 min, forming a layer of sprayed ice of 20 mm. 5) Harden the ice at -11 °C for a total of 150 freezing degree hours. The spraying water and the water in the ice tank had an ethanol content of 0.3 %. The spraying process resulted in a fine grain structure that captured the ethanol in small pockets. The mean ice thickness in which the tests were performed was 30 mm.

The ice material properties were measured according to the International Towing Tank Conference recommended procedures and guidelines (ITTC, 2014). The flexural (σ_f) and compressive (σ_c) strengths of the ice were measured at the end of each test day. The effective elastic-strain modulus (E) was only measured on the 17th of June 2021 (only one of the two test days analyzed in this study). Table 4.1 shows the measured material properties. The effective elastic-strain modulus determination is dependent on the measured ice thickness, causing uncertainty in the measured value. The values between parentheses in Table 4.1 show the effective elastic-strain modulus variation

following from an ice thickness change of ± 5 mm. Refer to Hendrikse *et al.* (2022b) for more details on the material property measurements. It is noted that the ice material properties are mentioned here only for relative comparison with previous test campaigns, the values may not reflect the properties during actual testing at different moments during the day. Results from the rigid structure tests and results of continuous crushing from the SDOF structure tests give a good indication of ice strength during testing and, in the view of the authors, provide more relevant information for penetration experiments than the material properties in Table 4.1.

Table 4.1: Material properties of the ice on two of the three test days considered in the present study. The material properties were measured at the end of the test day. The mean values are provided and the range of values measured are given in parentheses.

Ice sheet date	σ_f [kPa]	σ_c [kPa]	E modulus [GPa]
17-6-2021	521 (481-547)	563 (530-578)	13 (7.8–24)
23-6-2021	444 (424-475)	658 (631-678)	–

4

4.2.3. TESTS INCLUDED IN THE ANALYSIS

The present study considers results from three types of tests (see Figure 4.3). The first type concerns a rigid structure aimed at characterizing the velocity effect in ice loads, with ice drift speeds ranging from 1 mm s^{-1} to 150 mm s^{-1} . Table 4.A.1 gives an overview of the tests with a rigid structure considered in the present study. The test IDs represent test identifiers which can be used to obtain the raw test data from the public dataset (Hendrikse *et al.*, 2022b). The run name contains the test date and the run number. A run is a full passing of the carriage from one side of the ice tank to the other side. The runs are numbered consecutively starting from 1 on each test day. All tests with a rigid structure performed on the 17th and 23rd of June are analyzed in the present study.

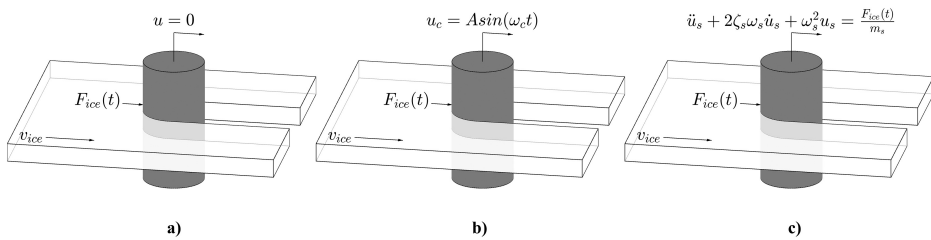


Figure 4.3: Illustration of the three types of tests included in the analysis: **a)** rigid structure; **b)** controlled-oscillation; **c)** single-degree-of-freedom structure. Denoted in the illustrations are the far-field ice drift speed v_{ice} , ice load at the ice action point $F_{ice}(t)$, the structural response u , controlled-oscillation amplitude A and frequency ω_c , and single-degree-of-freedom structural properties of damping as fraction of critical ζ_s , natural frequency ω_s , and mass m_s .

The test data from rigid tests are used as a basis for comparison with the data from

the controlled-oscillation tests. The controlled-oscillation tests employed a prescribed oscillation pattern of the structure resulting in the following structural displacement:

$$u_c(t) = A \sin(\omega_c t) \quad (4.1)$$

with $\omega_c = 2\pi f_c$ where u_c is the controlled displacement of the structure, A is a prescribed amplitude of oscillation (0.40 mm to 15.90 mm), and f_c is a prescribed frequency of oscillation (0.143 Hz to 4 Hz, see Table 4.A.2). For the test, the amplitude and frequency were chosen such that the minimum relative velocity between ice and structure reached zero during a cycle of oscillation:

$$\frac{v_{ice}}{A\omega_c} = 1 \quad (4.2)$$

where v_{ice} is the ice drift speed (constant carriage speed during the controlled-oscillation tests). The controlled-oscillation tests were performed in the same ice sheet as the rigid structure tests, often in the same run. An overview of the controlled-oscillation tests is shown in Table 4.A.2. The test matrix was derived with frequencies of oscillation resembling those of modes of an offshore wind turbine, and by repeating experiments previously conducted in another ice tank (Hendrikse and Metrikine, 2016).

Lastly, results from a constant deceleration test with a SDOF structure are included to investigate the compliance effect for comparison with the observations from the rigid structure and controlled-oscillation tests. Multiple tests have been performed and analyzed by van den Berg *et al.* (2022). Herein, only a single example is included (see Table 4.A.3).

4.3. THE LOAD-VELOCITY DEPENDENCE FROM RIGID STRUCTURE TESTS

The load-velocity dependence from the rigid structure indentation tests on the 17th and 23rd of June are shown in Figure 4.4 and Figure 4.5, respectively. The velocity effect is found in the peak loads at low velocities ($< 3 \text{ mm s}^{-1}$) being higher than those at high velocities ($> 3 \text{ mm s}^{-1}$) by about 50%. For the mean loads, the effect is almost 100%. The higher loads at low rates are mainly due to a higher mean load. This becomes clear when the results per velocity are plotted with the mean load subtracted (see Figure 4.4b and Figure 4.5b). The peak load range as a scatter from the mean seems to be rather independent of velocity on both days. It is interesting to note that, despite the similar ice growth procedure of the model ice, the mean loads on the 17th of June were 50% higher than those on the 23rd of June. The main cause for the disparity in means loads was the difference in freezing degree hours at the moment of the testing during the day. The majority of the testing on the 17th of June occurred about six hours later in the day than on the 23rd of June (see Table 4.A.1). However, the exact air and ice temperature profiles throughout the day were not recorded on those days. When comparing the mean loads to the ice material properties in Table 4.1, it should be clarified that the material property tests were performed at the same time of day, at the end of the test day, on their respective days.

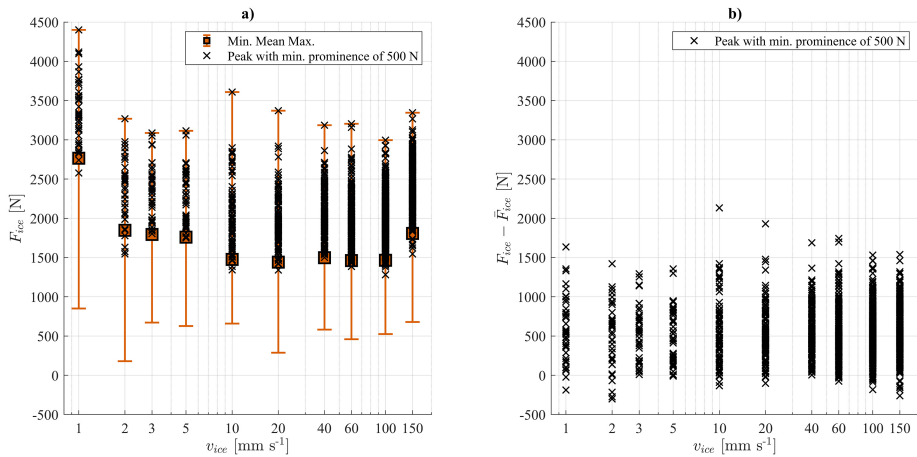


Figure 4.4: a): Load-velocity dependence as obtained from rigid structure tests on the 17th of June. b): Mean load \bar{F}_{ice} per test subtracted from the peaks. Peaks (black crosses) are selected based on a minimum peak prominence of 500 N. The minimum peak prominence is defined as the minimum relative height difference between peaks and determined by the *findpeaks* function in MATLAB.

An examination of the specific time series of the low-speed tests where the velocity effect is observed ($< 3 \text{ mm s}^{-1}$), and in particular at the start of those experiments, it was found that the higher loads were established within seconds. The first high peak load was attained within 1.3 s at 2 mm s^{-1} and within 3.2 s at 1 mm s^{-1} on the 23rd of June (see Figure 4.6). On the 17th of June, for the same test conditions, the peak was achieved in about 2.4 s at 1 mm s^{-1} , though difficult to judge given a malfunction at the start of the test, and 1.8 s at 2 mm s^{-1} . Note that the high peak was not related to a full ice-structure contact upon initial loading as the test sequence was such that low-speed tests always followed a high-speed test. Also, the higher mean load established quickly and then remained constant as the test progressed. Although the exact test procedure is not reported here (see Hendrikse *et al.* (2022b) for more information), two important details are provided. First, the carriage or actuator (see Section 4.2.1) was stopped and the pile was moved away from the ice edge between changes in ice drift speed, with waiting intervals varying between roughly 5 s and 60 s. Second, because the pile was moved away from the ice edge, contact between the ice and pile was lost and zero load was measured between speed changes. Although ice strains were not measured in the experiments, these conditions likely had some effect on strain recovery in the ice sheet. By alternating between high- and low-speed tests in the procedure, an attempt was made to minimize damage and time-dependent strain related effects on the ice load behavior from one test to another.

The consistent observation of higher mean and peak loads as a result of the loading history, specifically for low velocities in the case of the rigid structure tests, is henceforth referred to as an ice strengthening. The fact that this apparent strengthening of the ice manifested itself at the time scale of seconds is relevant for ice-structure interaction where

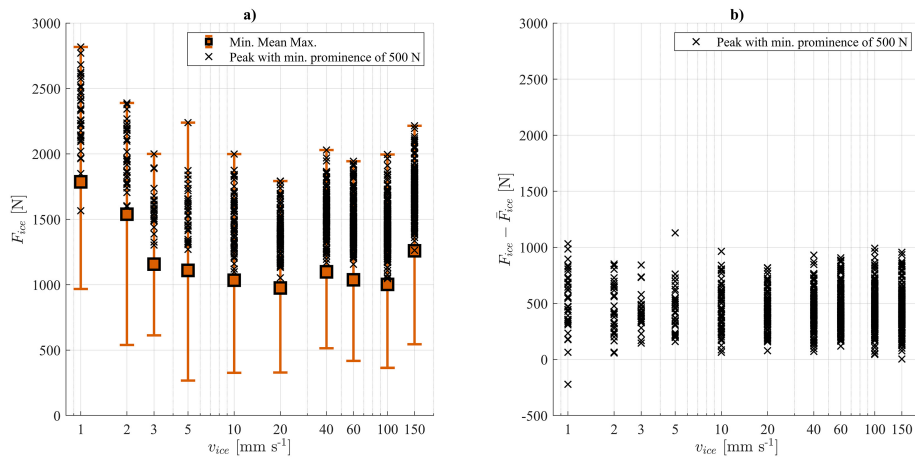


Figure 4.5: a): Load-velocity dependence as obtained from rigid structure tests on the 23rd of June. b): Mean load \bar{F}_{ice} per test subtracted from the peaks. Peaks (black crosses) are selected based on a minimum peak prominence of 500 N. The minimum peak prominence is defined as the minimum relative height difference between peaks and determined by the *findpeaks* function in MATLAB.

the relevant time scales are governed by the natural periods of structures, often on the order of tenths of a second to several seconds. The compatibility between the time scales of ice strengthening and natural periods of structures indicates that a strengthening could develop during a cycle of interaction for such structures when the velocity of loading of the ice becomes sufficiently low. This compatibility in time scales in terms of rapid ice strengthening is relevant in assessing whether the mechanism causing the velocity effect on rigid structures is the same as that responsible for the compliance effect on flexible structures, which is further treated in Section 4.6. In the next section, the results from the controlled-oscillation tests are analyzed and compared to those in this section to investigate the dependence of the load-velocity relation on loading history.

4.4. THE PEAK LOAD-VELOCITY DEPENDENCE FROM CONTROLLED-OSCILLATION TESTS

During the controlled-oscillation tests the relative velocity between ice and structure is not constant, but varies throughout the cycle of oscillation of the structure. This results in load peaks which occur within a range of relative velocities between ice and structure during each cycle of structural oscillation. Figure 4.7 and Figure 4.8 show the identified peak loads (using a minimum peak prominence of 500 N as determined by the *findpeaks* function in MATLAB) for the tests conducted on the 17th and 23rd of June, respectively. The arrows in Figure 4.7 and Figure 4.8 indicate if the relative velocity at the moment of failure was increasing (red color, rightward arrow) or decreasing (blue color, leftward arrow), defined as the sign of the derivative with respect to time of the relative velocity

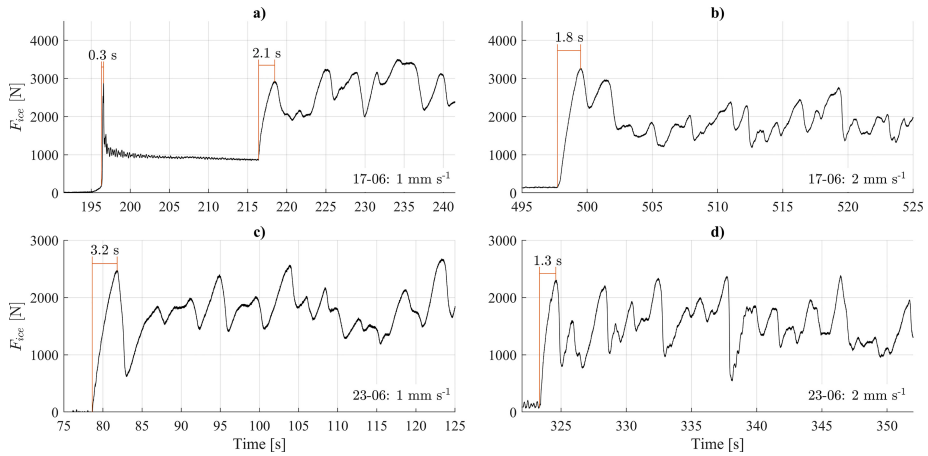


Figure 4.6: Start of rigid structure ice penetration tests at low speed indicating the time to establish the first high peak load: **a)** at 1 mm s^{-1} on the 17th of June; **b)** at 2 mm s^{-1} on the 17th of June; **c)** at 1 mm s^{-1} on the 23rd of June; and **d)** at 2 mm s^{-1} on the 23rd of June.

between ice and structure: $\text{signum} \left(\frac{d}{dt} [v_{ice}] - \frac{d^2}{dt^2} [A \sin(\omega_c t)] \right)$. The peaks from the rigid structure tests in the same channel are included in the figures as well.

On both days, at high relative velocities ($> 20 \text{ mm s}^{-1}$), the peak loads found for the controlled-oscillation tests were in the same range as those observed for the rigid structure tests. This holds when the relative velocity is either increasing and decreasing (red and blue arrows, respectively). At lower velocities, in the range of 5 mm s^{-1} to 20 mm s^{-1} , a clear difference is found in the data from the 23rd of June (see Figure 4.8). Peak loads for the controlled-oscillation tests are found to sometimes be higher than those for the rigid structure tests, but only when the loading rate was increasing (red arrows), with a few exceptions. However, the peak loads are not always higher when the relative velocity is increasing, as most red arrows reside in the range of peak loads observed for rigid structures (about 99 % and 93 % on the 17th and 23rd of June, respectively).

It seemed that the time spent, or duration, at a relative velocity in the lowest range, where a strengthening was also observed for the rigid structure, played a role in the higher peak loads. This is best illustrated when looking at both a time series of a test with many peaks exceeding those observed for a rigid structure and a time series of a test which follows the observations of a rigid structure as shown in Figure 4.9. The tests both had an oscillation from 0 to 40 mm s^{-1} relative velocity, but the difference was in the frequency of oscillation. For the 4 Hz oscillation, the load pattern seemed to be mostly stochastic (see Figure 4.9a). For the 0.5 Hz oscillation, however, the load pattern showed a clear periodicity (see Figure 4.9b). Many cycles showed a high peak load after the moment when the zero relative velocity was reached. The main cause for the difference between the results seemed to be the amount of time spent at the low relative velocity. For the 0.5 Hz test, combined with a far-field constant ice drift speed of 20 mm s^{-1} , this was about 0.35 s below 3 mm s^{-1} . At 4 Hz and 20 mm s^{-1} constant far-field ice drift speed, this was about 0.04 s which appeared to be insufficient time to result in a significant increase in

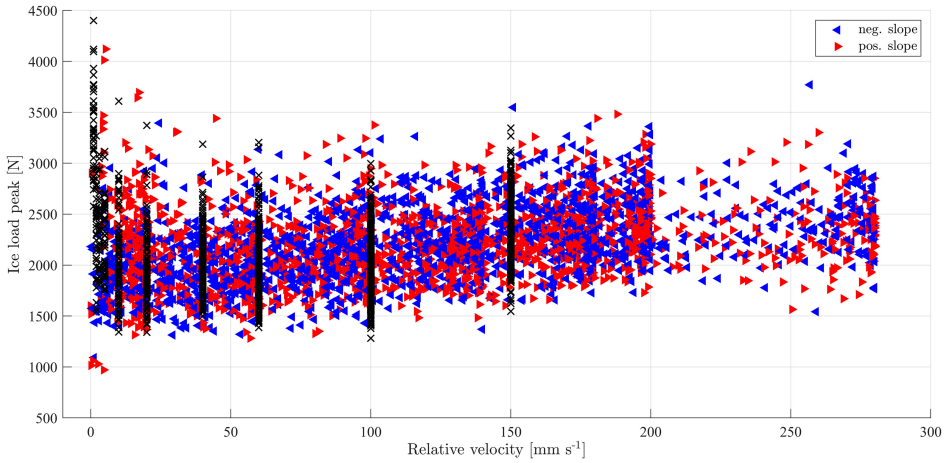


Figure 4.7: Comparison of peak loads from controlled-oscillation tests (red and blue arrows, selected based on a minimum peak prominence of 500 N) and rigid structure tests (black crosses, see Figure 4.4a) on the 17th of June. Arrows indicate the slope of relative velocity at the moment of failure: red, rightward arrows show positive slope; blue, leftward arrows show negative slope.

peak loads upon failure following the period of low relative velocity.

Referring again to Figure 4.7, the results from the 17th of June did not appear to show this duration effect very strongly. This can be explained based on the test matrix of that day. Most controlled-oscillation tests were conducted at high far-field ice drift speeds and for high frequencies. In those cases, the time spent at low relative velocity was minimal.

For each test, the time spent at low relative velocity which can result in a strength increase can be estimated by means of a threshold velocity from the rigid structure experiments v_{thres} of 3 mm s^{-1} . The following equation then applies (Hendrikse and Metrikine, 2016):

$$\Delta t = \frac{1}{(2\pi f)} \left(2 \arcsin \left(-1 + \frac{v_{thres}}{v_{ice}} \right) \right) \quad (4.3)$$

In Figure 4.10, the values of Δt for each of the controlled-oscillation tests are shown. On the 17th of June (left cluster in Figure 4.10), two of the tests (ID 428 and 429) with the highest values of Δt are indicated and their time series are shown in Figure 4.11. By inspecting each of the time series, the strengthening effect is indeed observed, though only significantly in test ID 428 (see Figure 4.11a). For the controlled-oscillation tests with Δt below a threshold of about 0.3 s, the strengthening effect was no longer observed, which corresponds to the minimum time required for an observable strengthening effect from the rigid structure tests.

To summarize, a minimum duration seemed to be required at low relative velocity for mean and peak loads to surpass high-speed ice crushing loads, referred to as the ice strengthening effect, for the controlled-oscillation tests. For high ice drift speeds and high frequencies, the strengthening effect was not readily observed, which is consistent

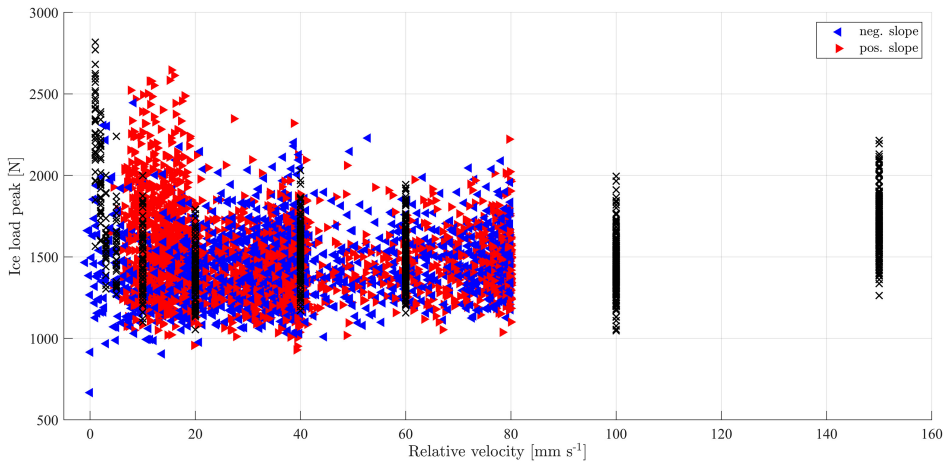


Figure 4.8: Comparison of peak loads from controlled-oscillation tests (red and blue arrows, selected based on a minimum peak prominence of 500 N) and rigid structure tests (black crosses, see Figure 4.5a) on the 23rd of June. Arrows indicate the slope of relative velocity at the moment of failure: red, rightward arrows show positive slope; blue, leftward arrows show negative slope.

with the results of Equation (4.3) in terms of little time spent at near-zero relative velocity. The strengthening in the controlled-oscillation tests resulted in the observation of peak loads which exceeded those for a rigid structure at the same far-field ice drift speeds. This matches with the definition of the compliance effect as shown in Figure 4.1. In terms of far-field ice drift speeds, it is hence found that the peak load-velocity relation is load-history dependent and cannot be uniquely defined¹ for ice penetration scenarios where the relative velocity enters the low-rate regime for a sufficient duration to cause a strengthening of the ice. In other words, the maximum peak load during brittle ice crushing is not a function of the far-field ice drift speed, but instead is a function of the relative velocity, which can then vary during the loading and therefore influence the maximum peak load.

The strengthening effect in the controlled-oscillation tests showed similarity to that observed for the rigid structure when considering the dependence on relative velocity instead of the far-field ice drift speed at the moment of the peak load. The reason for this is because the velocity experienced by the ice undergoing failure at the ice action point in the rigid structure tests is approximately equal to the far-field ice drift speed. Alternatively, in the controlled-oscillation tests, the velocity experienced by the ice undergoing failure is relative velocity. It thus follows that the velocity effect and compliance effect seem to originate from the same strengthening effect when relative velocity and not far-field ice drift speed is considered. To further substantiate this claim with respect to ice-induced vibrations, a SDOF structure test is analyzed in the next section, demonstrating that the strengthening effect indeed occurs during frequency lock-in and intermittent crushing.

¹The term *uniquely defined* refers to a one-to-one correspondence between far-field ice velocity and maximum peak load.

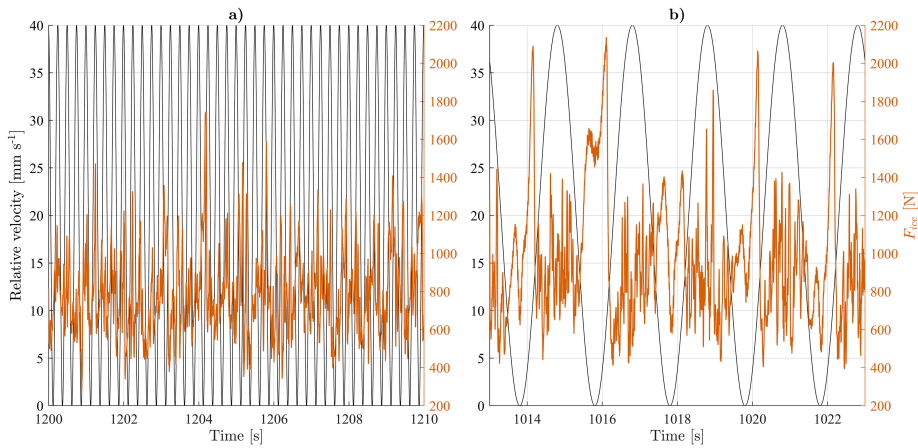


Figure 4.9: Example results on the 23rd of June from **a)** controlled-oscillation test (ID 504) showing peak loads in the same range as the rigid structure tests for the relative velocities included; and from **b)** controlled-oscillation test (ID 501) showing peak loads exceeding those on the rigid structure tests for the relative velocities included.

4.5. THE VELOCITY AND COMPLIANCE EFFECT DURING ICE-INDUCED VIBRATIONS

Figure 4.12 shows results from a constant deceleration experiment with a SDOF structure. This type of experiment was designed to resemble an ice floe slowing down and arresting against a flexible structure which in full-scale has been observed to result in frequency lock-in and intermittent crushing (Jefferies *et al.*, 2008; Peyton, 1968). At high far-field ice drift speeds the relative velocity remains high and continuous brittle crushing is observed.

Frequency lock-in developed for the far-field speed range between 25 and 30 mm s^{-1} approximately, though only for a few consecutive cycles at a time (see Figure 4.13). This type of interaction was accompanied by a duration of low, or even negative relative velocity. The strengthening effect clearly developed during the cycles of oscillation of the structure where high load peaks were observed after some duration of low relative velocity on the order of tenths of a second. Long sustained periods of frequency lock-in were typically only observed in tests with nearly constant far-field ice drift speed (van den Berg *et al.*, 2022) as overly rapid constant deceleration tests resulted in a very brief transition from continuous brittle crushing to intermittent crushing.

For lower ice drift speeds ($< 15 \text{ mm s}^{-1}$), intermittent crushing clearly developed (see Figure 4.14). Here, the relative velocity remained low until failure during the load build-up phase and the strengthening effect developed similarly to that of the rigid structure tests under constant far-field ice drift speed. In this comparison, the far-field ice drift speed of the rigid structure test was equal to the relative velocity of the SDOF structure test. Upon global failure and unloading, the relative velocity increased rapidly, typically by orders of magnitude, and the strengthening dissipated. At high relative velocity, multiple failures via brittle crushing ensued with peak loads much lower than those during the end of the load build-up phase. At the end of the test, the ice drift speed approached zero slowly

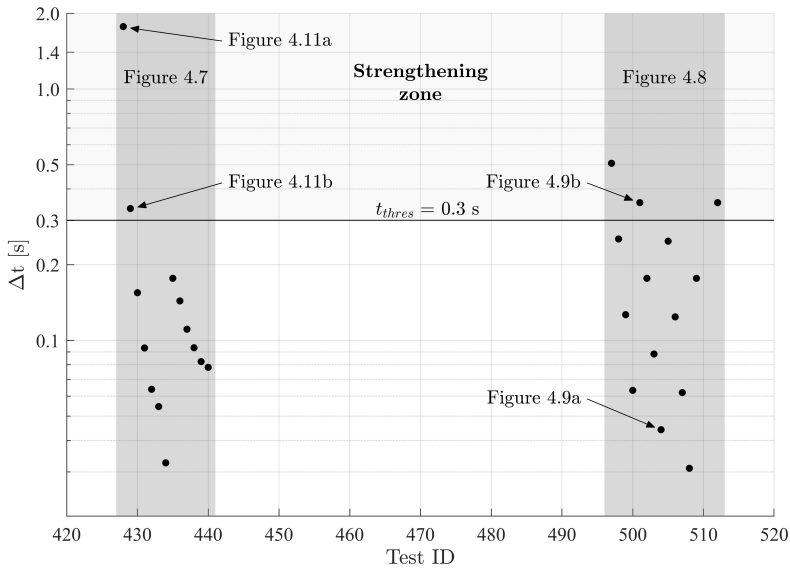


Figure 4.10: The Δt for each of the controlled-oscillation tests. The estimated minimum time t_{thres} required for an observable strengthening effect from the rigid structure tests is indicated by the horizontal line.

and the ice load increased to > 4 kN which is in accordance with that observed for the lowest speed tested for the rigid structure in Figure 4.4.

Figure 4.15 shows the peak loads from the SDOF structure test as a function of relative velocity as plotted in the same way as the controlled-oscillation test results in the previous section. It can be seen that the SDOF structure results show a similar load-history effect in peak loads as those from the controlled-oscillation tests. Higher peaks were observed for relative velocities in the range up to 10 mm s^{-1} when compared to a constant far-field ice drift speed for a rigid structure test. These peaks developed only after a period of loading (≥ 0.3 s) of the ice at near-zero relative velocity and are associated with the events of frequency lock-in and intermittent crushing as shown in Figure 4.13 and Figure 4.14, respectively.

Figure 4.15b shows the SDOF structure test results plotted, not for the relative velocity at the moment of peak load, but rather for the constant far-field ice drift speed. The comparison between Figure 4.15a and Figure 4.15b demonstrates how the effect of structural compliance could be mis-associated with too high velocities when using this more common way of plotting peak loads against velocity as illustrated, for example, in Figure 4.1. It should be noted that the peak loads exceeding those of the rigid structure tests (remaining red arrows) in Figure 4.15 that do not correspond to the cases of frequency lock-in and intermittent crushing instead correspond to the peak loads before or between the two selected time series in Figure 4.12 (between 20 s and 220 s, and between 250 s and 280 s).

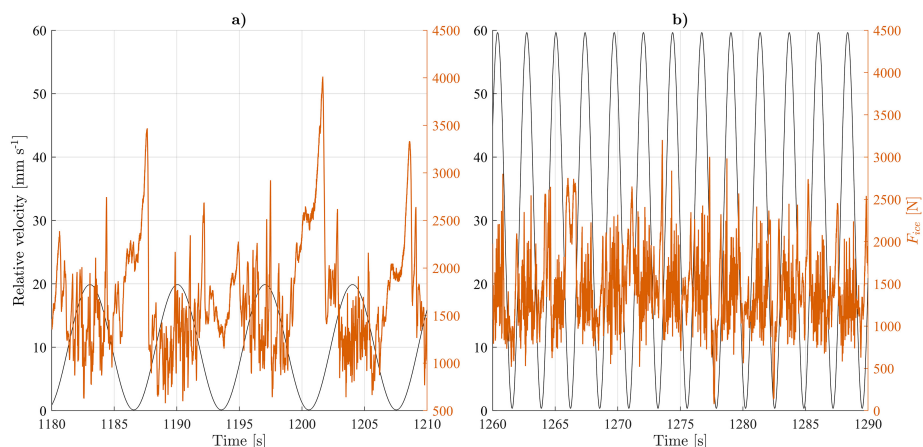


Figure 4.11: Strengthening effect developing in the controlled-oscillation tests of a) test ID 428 on the 17th of June; and b) to a lesser extent in test ID 429 on the 17th of June.

4.6. DISCUSSION

4.6.1. THE PEAK LOAD-VELOCITY DEPENDENCE DURING PENETRATION AND ICE-INDUCED VIBRATIONS

The foregoing observations and analysis indicate that the peak load-velocity dependence during ice penetration was found to be loading-history dependent. In cases where the relative velocity was constant, e.g. for rigid structures, the peak load-velocity dependence appeared to be uniquely defined. A velocity effect was observed as a rapid strengthening, within seconds, at low relative velocities. For cases where the relative velocity varied, but the time spent at low relative velocity was too short to activate the strengthening effect, the dependence remained uniquely defined; i.e. at the same far-field ice drift speed, the peak loads from the controlled-oscillation tests with high frequency and/or high ice drift speed did not exceed the peak loads from the rigid structure tests. However, when the time spent at low relative velocity was sufficient to activate the strengthening, the peak load-velocity relation showed a strong path dependence (see Figure 4.8 and Figure 4.15).

The strain and strain rate in the ice sheet were not measured in the experiments. Therefore, the dependence of the peak load-relative velocity relation on the stress-strain-rate relation could not be investigated. Nevertheless, a comment can be made about this dependence. Based on the analysis, it seemed that relative velocity and strain rate did not follow a proportional relationship because peak loads from controlled-oscillation tests were occasionally higher than those from the rigid structure tests. The particular path dependence of the peak loads from the controlled-oscillation tests may be related to microstructural damage, strain rate effects in the ductile-to-brittle transition in relatively undamaged ice, or a combination of both.

As there is a minimum amount of time associated with the strengthening effect, there should be a limit in terms of the maximum frequency for which frequency lock-in vibrations can develop. ISO 19906 (2019) refers to field observations of frequency lock-in

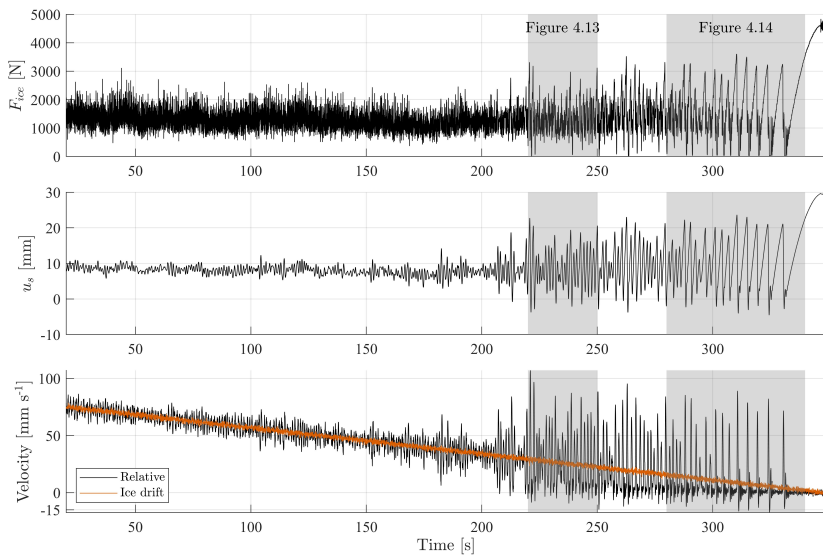


Figure 4.12: Constant deceleration test (ID 445) with a single-degree-of-freedom structure on the 17th of June. Top: Ice load. Middle: Structural displacement. Bottom: Relative velocity and ice drift speed.

up to 10 Hz. It would be of interest to determine the time constant associated with the strengthening process as a function of ice type and temperature. This may allow the definition of a dimensionless number for ice-induced vibrations relating the time at low relative velocity during interaction to a characteristic time as a material property of the ice. This is left for further study.

In terms of modeling of ice-induced vibrations, it is important to note that models adopting a bijective relation between peak load and velocity do not correctly account for the loading history. The implied instantaneous strengthening of the ice occurs in those models (Kärnä, 1992; Määttänen, 1998; Withalm and Hoffmann, 2010) in cases where there is actually not sufficient time for the strengthening to develop. Models where the peak load-velocity relation develops as a result of a time-dependent strengthening effect can account for the load-history dependence (Hendrikse and Nord, 2019).

4.6.2. COMPLIANCE AND VELOCITY EFFECTS IN ICE PEAK LOADS

The results from the penetration experiments performed with the rigid structure, controlled oscillation, and SDOF structure in the present study show that peak loads depend on the amount of time spent at low relative velocities where a strengthening of the ice can develop. Both the velocity and compliance effects describe the scenario in which peak ice loads increase with low relative velocity. The observed compliance effect (see Figure 4.15) likely originates from the same mechanism as the velocity effect seen for rigid structures as demonstrated with the controlled-oscillation tests. As stated previously, for ice acting with any velocity against a rigid structure, the far-field ice drift speed is

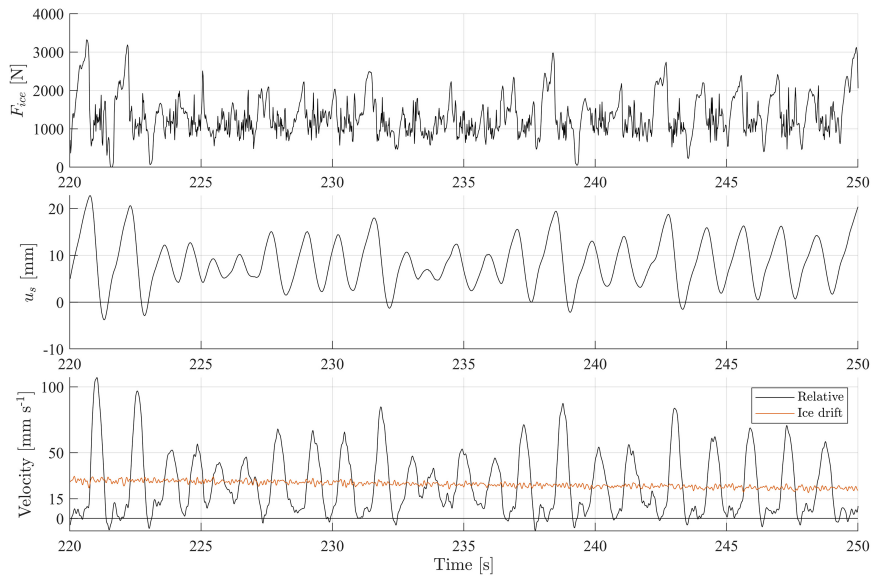


Figure 4.13: Detailed view of frequency lock-in type oscillation occurring in test ID 445 (single-degree-of-freedom structure test). Top: Ice load. Middle: Structural displacement. Bottom: Relative velocity and ice drift speed.

equal to the relative velocity. For a compliant structure, the structural velocity needs to be subtracted from the far-field ice drift speed to result in a relative velocity, which shifts the strengthening effect to lower velocities as highlighted in Figure 4.15. This shift is important with respect to design ice loads. If the effects indeed originate from the same mechanism, then the peak loads on a compliant structure cannot exceed those at the lowest speeds on a rigid structure. Indeed, ISO 19906 (2019) states that the maximum loads on a compliant structure during intermittent crushing can be considered equal to the maximum loads on a rigid structure (Kärnä and Masterson, 2011). Based on our test results, this is a correct approach provided that the value used for C_R accounts for the velocity effect. It is further important to correctly interpret peak loads plotted against the far-field ice drift speed when the compliance effect is investigated since such plots can show peak loads at higher velocities than the actual relative velocity at the moment of failure (see Figure 4.15).

4.6.3. RAPID STRENGTHENING AT LOW RELATIVE VELOCITY AS A PROPERTY OF ICE OR MODEL ICE ONLY

The observed rapid strengthening effect could be a property of model ice only. But since there is little evidence of tests on naturally occurring ice where the relative velocity was varied during penetration in a way as was done during the controlled-oscillation tests, this claim is difficult to confirm. Recent tests on the flexural strength of ice did, however, show a strengthening under cyclic loading which demonstrates that ice can exhibit such

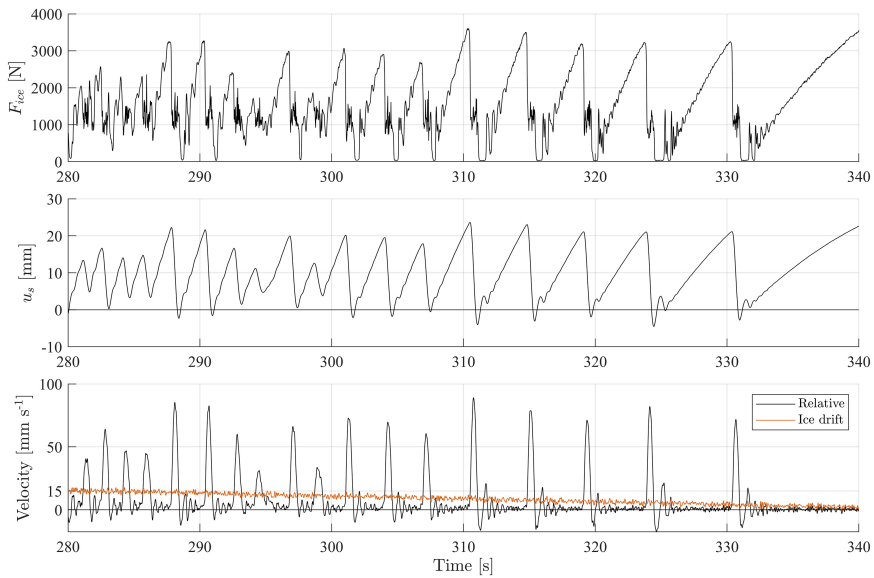


Figure 4.14: Detailed view of intermittent crushing vibrations occurring in test ID 445 (single-degree-of-freedom structure test). Top: Ice load. Middle: Structural displacement. Bottom: Relative velocity and ice drift speed.

type of behavior (Murdza *et al.*, 2020; Murdza *et al.*, 2021b). Similarly, cyclic biaxial compression of freshwater ice demonstrated strengthening by a factor of 1.5 in failure strength when subjected to moderate confinement and progressively higher loads (Iliescu and Schulson, 2002). Besides cyclic ice behavior, so-called damage or pre-straining in ice has shown to shift the ductile-to-brittle transition in ice to higher strain rates, thereby delaying failure in uniaxial compression experiments on both saline and freshwater ice (Snyder *et al.*, 2016). A physical explanation for ice strengthening may be in the form of dislocation pile-ups and grain boundary sliding or back stress development which relaxes over time and is enhanced by microstructural damage. A recent discussion on dislocation and grain boundary behavior in ice by Cole (2021) also showed there may be an explanation found in the low-speed deformation behavior and delayed elasticity of ice. In the past, the authors ascribed the strengthening to result from a change in the contact between ice and structure. A phenomenological model based on this idea has shown to be quite capable of simulating ice-induced vibrations (Hendrikse and Metrikine, 2015). Though the contact area change may be an artifact of the way measurements were made in the past with tactile sensors, as speculated by other researchers, the strengthening effect is real. Furthermore, even if the strengthening effect is related to a different physical mechanism in the ice, one could model it with the same phenomenological approach. Now that it is clearer where to investigate, it may be possible to develop a physics-based model which captures the strengthening, something which will allow for much more accurate prediction of full-scale dynamic ice-structure interaction.

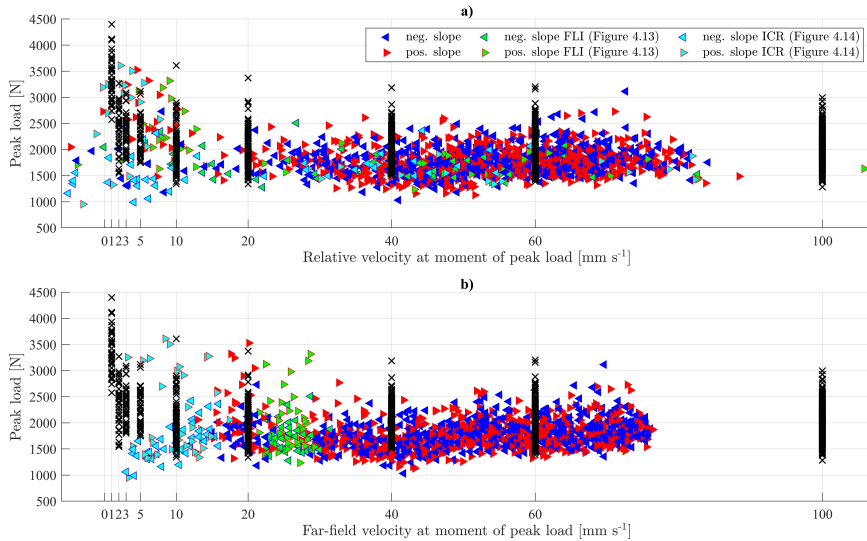


Figure 4.15: Velocity and compliance effect example: **a)** peak loads from test ID 445 identified with a minimum peak prominence of 500 N, as a function of relative velocity at the moment of peak load; **b)** peak loads from test ID 445 (17th of June) identified with a minimum peak prominence of 500 N, as a function of far-field velocity at the moment of peak load. Peak loads from the rigid structure tests on 17th of June are marked by black crosses (see Figure 4.4a). Arrows indicate the slope of relative velocity at the moment of failure: red, rightward arrows show positive slope; blue, leftward arrows show negative slope. The cases of frequency lock-in (FLI) and intermittent crushing (ICR) are identified by the green and cyan colors, respectively.

4.6.4. COMMENT ON SPALLING AS A MECHANISM FOR ICE-INDUCED VIBRATIONS

In the experiments from the present study, ice-induced vibrations were found to develop as a result of strengthening of the ice when loaded for some tenths of a second at low relative velocities. An alternative mechanism for ice-induced vibrations has been proposed in the literature, which is the synchronization between the frequency associated with spalling of the ice and a natural frequency of the structure (Gagnon, 2022). In the experiments from the present study, it is found that multiple events of failure of the ice occur during each cycle of interaction, rather than just a single spalling event. During intermittent crushing, one of the failure events is related to the long load build-up phase with low relative velocity, but it is followed by multiple failure events during the unloading phase when the relative velocity is high (see Figure 4.14). It could be speculated that the full-scale data from the Molikpaq do not show sufficient detail to discern the unloading phase (Owen and Hendrikse, 2021), leading to a misinterpretation that there is only a single failure event per saw-tooth cycle. Though it cannot be excluded based on the experiments in the present study that the spalling mechanism governs ice-induced vibrations in full-scale, it would, in the view of the author, be a most interesting coincidence

if model ice contains a completely different mechanism from sea ice which results in exactly the same complex ice-structure interaction phenomena.

4.7. CONCLUSION

The ice penetration experiments in model ice were performed with a rigid structure, controlled oscillation of the structure, and a SDOF structure. A comparison of results showed that the peak global ice loads depended on the amount of time spent at low relative velocities, regardless of the structural compliance, during which an ice strengthening effect developed. Although the experiments were performed in ethanol-doped model ice of nominally 30 mm thickness with a pile of 200 mm in diameter, the consistency of the results and their similarity with the literature give support to the claim that the ice strengthening effect may be a general property of ice. This has implications for the so-called velocity effect and compliance effect in design of structures subject to dynamic ice-structure interaction.

The main conclusions are summarized as follows:

1. The peak load-velocity dependence for ice penetration was a function of loading history with a critical dependence on the time spent at near-zero relative velocity (≥ 0.3 s).
2. Rapid ice strengthening developed at low relative velocities, which persisted until the relative velocity reach about 20 mm s^{-1} and ice failure dissipated the strengthening effect.
3. The rapid ice strengthening resulted in peak loads, under the conditions of a varying relative velocity, which exceeded those for a constant penetration velocity, but only when the relative velocity increased from near zero to above about 10 mm s^{-1} .
4. The ice strengthening effect was observed during each cycle of ice-induced vibrations, specifically for frequency lock-in and intermittent crushing, thereby causing the high peak loads observed during such interaction.
5. Based on the comparison of the peak loads as a function of relative velocity from the rigid structure tests and tests with controlled oscillation of the structure, the velocity effect and compliance effect during penetration seemed to originate from the same strengthening effect, implying that absolute peak loads on compliant structures would not exceed those for the lowest speeds on rigid structures.
6. It is cautioned that assigning peak loads to the far-field ice drift speed for compliant structures may result in the attribution of high peak loads to velocities exceeding the actual relative velocities at which the peak loads develop.

4.A. EXPERIMENTAL DATA FROM TEST CAMPAIGN

Experimental data for the present study have been selected from Hendrikse *et al.* (2022b) and are listed in Table 4.A.1, Table 4.A.2, and Table 4.A.3 below.

Table 4.A.1: Overview of rigid structure tests considered in the present study.

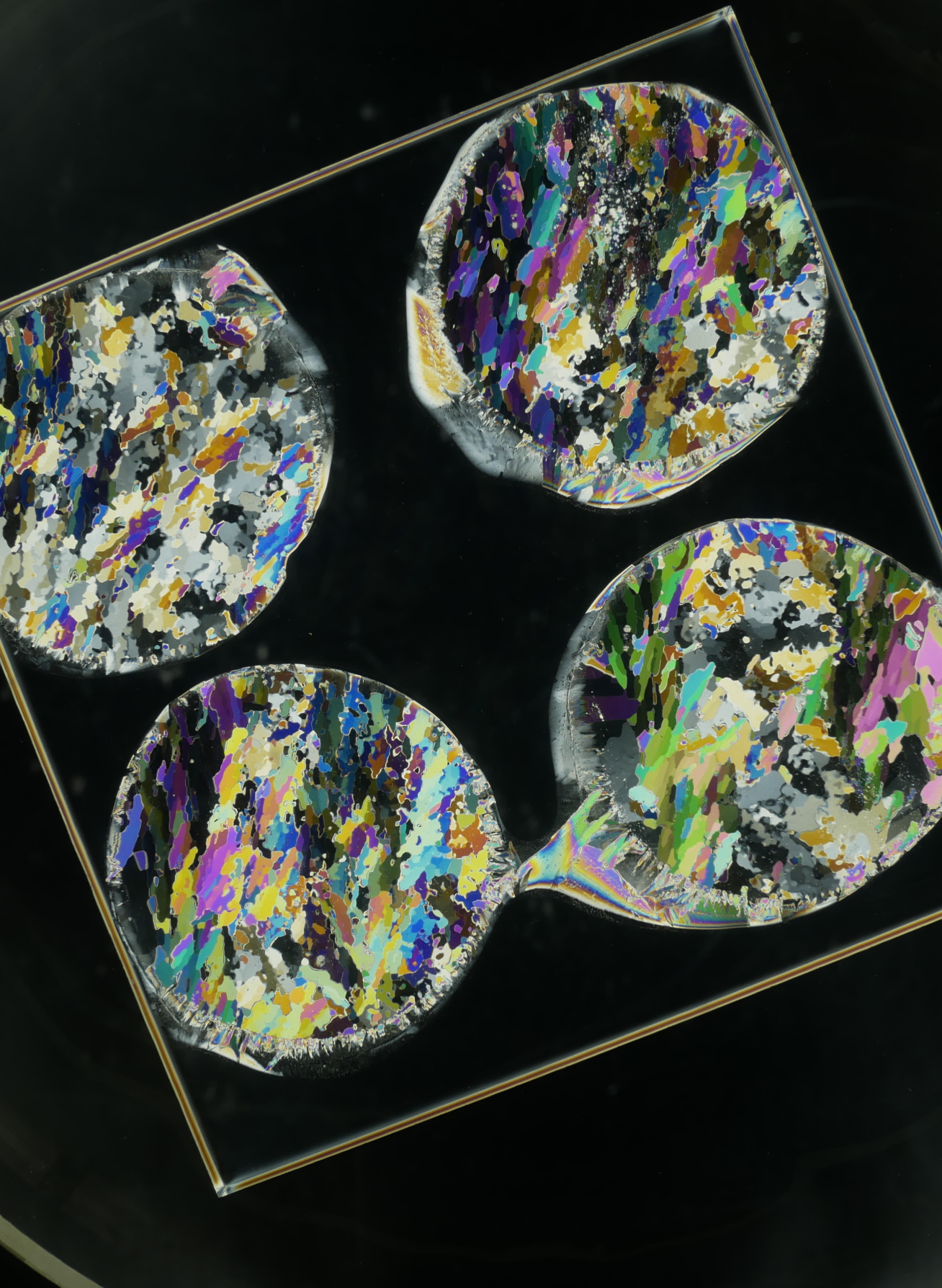
ID	Run name	Speed [mm s ⁻¹]	Duration [s]	Time of day [HH:MM]
487	2306_1	100	19	09:28
488	2306_1	1	193	09:28
489	2306_1	40	21	09:32
490	2306_1	2	99	09:33
491	2306_1	150	11	09:34
492	2306_1	5	40	09:35
493	2306_1	60	21	09:36
494	2306_1	3	67	09:36
495	2306_1	20	31	09:38
496	2306_1	10	40	09:38
418	1706_10	100	21	16:09
419	1706_10	1	197	16:10
420	1706_10	40	21	16:14
421	1706_10	2	100	16:15
422	1706_10	150	10	16:17
423	1706_10	5	41	16:18
424	1706_10	60	21	16:19
425	1706_10	3	67	16:20
426	1706_10	20	31	16:22
427	1706_10	10	42	16:23

Table 4.A.2: Overview of controlled-oscillation tests considered in the present study.

ID	Run name	v_{ice} [mm s ⁻¹]	f_c [Hz]	A [mm]	Time of day [HH:MM]
428	1706_10	10	0.143	11.00	16:25
429	1706_10	30	0.429	11.00	16:27
430	1706_10	50	0.716	11.00	16:29
431	1706_10	70	1.002	11.00	16:30
432	1706_10	90	1.289	11.00	16:30
433	1706_10	100	1.432	11.00	16:31
434	1706_10	140	2.025	11.00	16:32
435	1706_10	20	1.000	3.20	16:33
436	1706_10	30	1.000	4.80	16:34
437	1706_10	50	1.000	7.95	16:35
438	1706_10	70	1.000	11.10	16:36
439	1706_10	90	1.000	14.30	16:37
440	1706_10	100	1.000	15.90	16:37
497	2306_1	10	0.500	3.18	09:39
498	2306_1	10	1.000	1.59	09:40
499	2306_1	10	2.000	0.80	09:42
500	2306_1	10	4.000	0.40	09:43
501	2306_1	20	0.500	6.37	09:44
502	2306_1	20	1.000	3.18	09:45
503	2306_1	20	2.000	1.59	09:46
504	2306_1	20	4.000	0.80	09:47
505	2306_1	40	0.500	12.73	09:48
506	2306_1	40	1.000	6.37	09:49
507	2306_1	40	2.000	3.18	09:50
508	2306_1	40	4.000	1.59	09:51
509	2306_1	20	1.000	3.18	09:52
512	2306_1	20	0.500	6.37	09:55

Table 4.A.3: Overview of single-degree-of-freedom structure tests considered in the present study.

ID	Run name	v_{ice} [mm s ⁻¹]	f_s [Hz]	m_s [kg]	ζ_s [%]	Time of day [HH:MM]
445	1706_11	Ramp	0.889	5020	10.6	17:06



5

DISCUSSION AND CONCLUSION

In this chapter, a discussion is presented which links each journal publication-based chapter to ice mechanics in ice-induced vibrations generally. The discussion is followed by the main conclusions from each journal publication in following with the structure of this thesis. Finally, an outlook on the ice mechanics in ice-induced vibrations is offered for future research.

5.1. DISCUSSION

Based on the research performed in this thesis, the physical mechanisms responsible for ice-induced vibrations of vertically-sided structures remain obscured. However, greater clarity is granted to the problem of the ice mechanics involved in ice-induced vibrations by relating the results in this thesis to the literature. To begin, the ice-induced vibrations problem can be divided into three themes which focus on the ice. The first is the contact process, which entails the means by which load is transferred from the ice to the structure. The second is the constitutive ice behavior, which embodies the continuum mechanics of the ice in terms of stress, strain, and strain rate, or load, deformation, and deformation rate due to the uncertainty of the relevant length dimension from the ice edge. The third theme is fracture mechanics, which refers to crack formation from microcracks on the grain scale to spalling or flaking on the ice sheet scale. There obviously exists overlap between the three themes, especially regarding the topic of damage in the ice, and the involvement of pulverized ice at the ice-structure interface. These themes are addressed next.

5.1.1. CONTACT PROCESSES AT THE ICE-STRUCTURE INTERFACE

The contact processes during ice-induced vibrations, namely contact area variation, were not directly investigated in this thesis. Even so, the contact processes are an integral component of ice-induced vibrations as evidenced by apparent non-simultaneous to simultaneous ice failure on full-scale structures based on load panel measurements (Bjerkås and Skiple, 2005; Jefferies and Wright, 1988) and by tactile sensor measurements on small-scale structures in model ice during ice-induced vibrations (Nord *et al.*, 2015; Ziemer, 2021) and controlled oscillations resembling frequency lock-in vibrations (Hendrikse and Metrikine, 2016). The contact area and local pressures at the ice-structure

interface were not measured during the first SHIVER test campaign (Hendrikse *et al.*, 2022b), but the global ice load patterns during controlled-oscillation tests were remarkably similar between cold ethanol-doped model ice (see Chapter 4) and warm saline model ice (Hendrikse and Metrikine, 2016). From this comparison, it may be inferred that the contact processes may not be unique to any one type of model ice. Most interestingly, the load patterns measured during cyclic crushing of columnar-grained freshwater ice in the laboratory tests in this thesis (see Chapter 3) also qualitatively resembled those from the model ice tests (see Chapter 4). While no direct contact area or pressure measurements were recorded from the laboratory tests, such striking similarities across ice types and loading scenarios gives confidence to similar contact processes resulting in similar load patterns. Consequently, it can be inferred that constitutive ice behavior as a function of deformation and deformation rate significantly contribute to the variation in contact processes which cause the observed load patterns. This alignment of observations supports the contact area variation theory with regards to the ductile or plastic ice deformation at low relative velocity. The stress relaxation load patterns observed in Chapter 3 suggest that not just contact area, but also local pressures varied with deformation and deformation rate. Moreover, given the similarity in load patterns between the laboratory experiments and the ice tank experiments in Chapter 4, it can be inferred that local pressure variation may have also occurred in the ice tank tests. These findings emphasize the importance of understanding the constitutive ice behavior in ice-induced vibrations, which is discussed next.

5.1.2. CONSTITUTIVE ICE BEHAVIOR

The stress-strain relationship and fracture of ice has been a subject of detailed research over roughly the last 70 years (e.g. Gold, 1960; Schulson and Duval, 2009). The constitutive behavior of ice in dynamic ice-structure interaction has received attention as well, considering uniaxial or triaxial stress states and damage in the ice (e.g. Jordaan and Barrette, 2014; Stone *et al.*, 1997). But the application of the constitutive modeling of ice, especially regarding delayed-elasticity, to ice-induced vibrations specifically has not been proposed until recently (Cole, 2021). Most notably, the duration and stress levels associated with delayed-elastic ice behavior align well with the contact area variation theory of ice-induced vibrations. Moreover, the findings in this thesis (see Chapter 3) also suggest that delayed-elastic ice behavior may contribute to the development of frequency lock-in vibrations by allowing stress relaxation at low relative velocity which inhibits fracture. This observation aligns with the explanation for the ductile-to-brittle transition in compression of ice via crack tip blunting (Chauve *et al.*, 2017; Schulson and Duval, 2009). Additionally, uniaxial compression of ice has shown an increase in strain at failure with decreasing strain rates (Cole, 1987; Hawkes and Mellor, 1972; Wu *et al.*, 1976).

In the field of ice mechanics, creep refers to the behavior of ice under constant stress, and typically studied in uniaxial, but also in biaxial and triaxial, stress conditions (e.g. Schulson and Duval, 2009). It is important to highlight the distinction between global creep of an ice sheet against an offshore structure (e.g. Ponter *et al.*, 1983) and creep behavior of ice in a creep test. For the ice sheet at very low and constant drift speeds, deformation is constant at and near the ice-structure interface. But for ice in a creep test, stress is constant and deformation occurs as a function of the constant stress and

microstructural changes in the material at high strains (e.g. Glen, 1955). It is believed that this distinction is significant when considering constitutive modeling of ice for ice-structure interaction modeling: deformation-controlled rather than stress- or load-controlled ice mechanics is a better representation for a dynamic ice-structure interaction scenario.

One last but crucial point to be made about constitutive ice behavior is the role of confinement in the deformation and failure of ice in compression. Biaxial and triaxial compression tests have demonstrated that ice strength and ductility increase with increasing confinement (Schulson and Duval, 2009), findings which are very relevant for ice-induced vibrations wherein the ice being crushed at the ice-structure interface is confined by the surrounding ice and by the structure. While significant research has been done in this field (e.g. Jordaan, 2001; Turner, 2018), the application of multiaxial constitutive ice modeling for prediction of ice-induced vibrations has yet to be realized.

5.1.3. ICE FRACTURE MECHANICS UNDER COMPRESSION

Abundant research has been performed on fracture of ice under compression (e.g. Schulson and Duval, 2009; Tuhkuri, 1995). However, the detailed processes of fracture in ice-induced vibrations require further investigation. Experience with small-scale basin testing in thick freshwater ice (Muhonen, 1996; Muhonen *et al.*, 1992) and thin freshwater ice (Nakazawa and Sodhi, 1990) indicated the presence of cleavage cracks which apparently led to spalling and flaking and subsequent load drops during intermittent crushing. These same cleavage cracks were also observed in the JOIA test campaign (Takeuchi *et al.*, 2001) and in the STRICE campaign (Kärnä, 2010). What is important to emphasize regarding fracture in ice-induced vibrations is that macroscopic fracture, especially at the scale of the ice thickness or greater, is the load-limiting mechanism for brittle ice behavior (as was observed in Chapter 3). Microcracks, or fracture at the grain scale, and their formation under compression during ice-induced vibrations may or may not contribute to the load-limiting mechanism. The accumulation of microcracks observed during small-scale basin tests of ice-induced vibrations resulted in an opaque appearance in thin freshwater ice sheets ahead of the structure (Nakazawa and Sodhi, 1990). The presence of microcracks may lead to macroscopic fracture via coalescence, but this is not necessarily the case because the microcracks may form beyond the zone where spalling and flaking occur. Instead, the microcracks indicate damaged ice, which possesses different mechanical properties from the undamaged parent ice (see Chapter 3).

5.1.4. ICE DAMAGE AND STRENGTHENING

Ice has been shown to radically change its mechanical properties once subjected to permanent deformation, herein referred to as damage, under high stresses, especially under confinement (Barrette and Jordaan, 2003; Meglis *et al.*, 1999; Melanson *et al.*, 1999; Zhou *et al.*, 2016), and for long time periods at low stresses (Duval *et al.*, 1983; Glen, 1955; Mellor and Cole, 1983; Snyder *et al.*, 2016). Due to the large strains, high stresses, and range of strain rates experienced by the ice during ice-induced vibrations, it becomes obvious that ice is a path-dependent material in terms of loads and velocities at and in the

vicinity of the ice-structure interface. One manifestation of this path-dependent behavior is the apparent ice strengthening as described in this thesis (see Chapter 4) and in the literature for compression (Iliescu and Schulson, 2004) and bending (Iliescu *et al.*, 2017; Murdza *et al.*, 2021a; Murdza *et al.*, 2020; Schulson *et al.*, 2019). Another is the increased viscous behavior of damaged ice as compared to undamaged ice as described in this thesis (see Chapter 3) and in the literature (Cole, 2021). The causes for this increased viscous or ductile behavior are multifaceted and not well understood, involving increased dislocation activities (Cole, 2021), microcrack formation and blunting (Schulson and Duval, 2009) or healing (Murdza *et al.*, 2022), dynamic recrystallization (Jordaan, 2001), regelation (Barnes *et al.*, 1971), sintering (Blackford, 2007; Szabo and Schneebeli, 2007), and possibly others. It is quite clear that this topic requires further investigation into the ice mechanics associated with path-dependent behavior.

One final note is made here. The damaged but intact ice at and near the ice-structure interface during ice-induced vibrations most likely has constitutive and strength properties which differ from the undamaged parent ice sheet. Creep and strength testing of the parent ice may not be representative of the ice involved in the interaction process, and models which are founded upon uniaxial compression of ice likely miss the effect of damage on the ice behavior in ice-induced vibrations (Yu and Low, 2022). Some attention has been given to this topic in modeling approaches considering damaged ice (Morsy, 1995; Weiss and Dansereau, 2017), but the approaches have been strictly phenomenological and preclude physical processes. It is the opinion of the author that future research on ice mechanics in ice-induced vibrations should focus on the constitutive and strength behavior of ice under relevant path-dependent stress, strain, and strain rate scenarios.

5.1.5. REFLECTION ON ICE MECHANICS IN ICE MODELING

While the current state-of-the-art ice modeling approach is phenomenological (Hendrikse and Nord, 2019), some evidence from this thesis and from the literature on ice mechanics give support to the assumptions made in the model. First, the stress relaxation observed in Chapter 3 and the findings from Cole (2021) give support to the assumption of delayed-elastic ice behavior in the ice model. Second, the increasing strain at failure in uniaxial compression of ice for decreasing strain rates aligns well with the assumption of rate-dependent local failure length of the ice elements in the phenomenological model. Third, the higher ice load peaks as a consequence of a duration at low relative velocity, as seen to some extent in both Chapter 3 and Chapter 4 indirectly supports the contact area variation theory upon which the model is founded. Since contact area and local pressures were not measured in either set of experiments in this thesis, it can only be inferred that the assumption of viscous deformation in the ice—whether visco-elastic or visco-plastic—at low relative velocity is likely valid, and appears consistent between the results in Chapter 3 and Chapter 4 and the contact area variation theory of ice-induced vibrations. Further experimental research on the relationship between the constitutive ice behavior and the ice-induced structural response could greatly aid in future model development.

5.2. SUMMARY AND CONCLUSIONS

The main objective of the thesis was to experimentally investigate the ice mechanics involved in ice-induced vibrations and, ideally, identify the physical mechanisms governing the development of ice-induced vibrations of vertically-sided offshore structures. To this end, an ice laboratory was developed at Delft University of Technology, within which laboratory-scale experiments of ice mechanics were devised and conducted to investigate whether dynamic recrystallization of ice was either the cause or effect of the development of ice-induced vibrations. In Chapter 2, a method was constructed to identify and assess dynamic recrystallization of ice thin sections based on crossed-polarization transmitted light, with the byproduct of being capable of quantifying ice texture and (quarter) fabrics of thin sections. The laboratory-scale experiments, in Chapter 3, attempted to reproduce the stress and strain states of ice at the ice edge during frequency lock-in vibrations by laterally confining a columnar, freshwater ice plate and compressing the edge of the ice plate with a haversine velocity waveform. The ice plate was confined by glass plates and the ice plate was viewed through the glass with crossed-polarized transmitted light to observe the texture of the ice plate. The results strongly suggested an absence of dynamic recrystallization but the presence of stress relaxation observable in both the load signal and the change in stress-induced birefringence of the ice. Remarkably, the load signal from the laboratory experiments resembled the load signal measured during ice penetration tests with the controlled-oscillation of a rigid model-scale structure at the Aalto Ice and Wave Tank, as described in Chapter 4. This similarity gives support to the finding that viscous ice behavior—with different ice types and loading scenarios—is relevant for the development of frequency lock-in, and of ice-induced vibrations more generally.

Chapter 2 presented a method for identifying ice thin section textures and (quarter) fabrics based on interference coloration theory using crossed-polarized transmitted light. The method required a series of in-plane photographs of the ice thin section rotated azimuthally in the crossed-polarized light on a polariscope. By verifying the approach with laboratory-grown freshwater and lake ice, the accuracy was deemed sufficient for ice texture and fabric analysis in the absence of a Rigsby stage or other specialized equipment. The method has the potential for complete fabric analysis with the addition of extra photographs taken with a wave plate between the ice sample and the upper polarizer. The method was developed with the intention to identify dynamic recrystallization of ice under compressive loading for the dedicated experiments performed in Chapter 3.

To assess whether and how dynamic recrystallization manifested in high-pressure zones at the ice edge during ice-induced vibrations, a dedicated laboratory-scale experimental setup was designed and tests were conducted as presented in Chapter 3. The test setup attempted to reproduce the loading and confinement scenario expected at the ice edge during frequency lock-in vibrations. To this end, a thin columnar freshwater ice plate of ice was laterally confined and then loaded on edge by a steel plate with a haversine velocity waveform. Glass plates provided the lateral confinement and permitted the transmission of crossed-polarized light through the confined ice plate, thereby exposing the grain structure in-situ during loading. The ice plate was then cyclically crushing and the load and displacement on the steel plate were measured along with video recording of the ice plate.

The main conclusions from Chapter 3 are summarized as follows:

- The cyclic crushing of confined, freshwater columnar ice demonstrated dichotomous deformation behavior: brittle at high velocity and non-brittle at low velocity.
- At low velocity, ice fracture was interrupted and stress relaxation occurred until the velocity began increasing in the cycle. The stress relaxation in the load was accompanied by stress-optic effects in the ice.
- A load peak-velocity hysteresis developed in each crushing cycle: peak loads following the non-brittle behavior were temporarily higher than the peak loads of the brittle behavior.
- The temporary load peak enhancement tended to increase with increasing duration of stress relaxation, i.e. the peak enhancement tended to increase with decreasing mean velocity and frequency. Negligible peak enhancement and stress relaxation duration were observed for the highest frequency and mean velocity tested of 2 Hz and 10 mm s^{-1} , respectively.
- For tests with a minimum velocity of 1 mm s^{-1} , no stress relaxation was observed in the load measurement.
- Preliminary results from the experiments with a deviating haversine velocity waveform, by increasing the minimum velocity, showed that the stress relaxation duration decreased, but the non-brittle peak load did not decrease.
- It is speculated that anelastic ice behavior (as a function of accumulated microstructural damage) could account for the rapid stress relaxation at low velocity.
- It is unclear what causes the hysteresis, although it is speculated that dynamic strain aging might play a role.
- The change in ice behavior during the experiments demonstrates a mechanism which develops rapidly and might therefore incite the development of the frequency lock-in regime of ice-induced vibrations of vertically sided structures.

The change in ice behavior during the experiments may be explained by delayed-elastic or viscoelastic behavior being more pronounced at low loading rates. It should be stated here that dynamic strain aging was most likely not involved in any processes related to deformation and failure of ice during frequency lock-in (Weiss, 2019). Similar ice behavior and loading patterns were observed ice penetration tests at the Aalto Ice and Wave Tank during controlled-oscillation with a rigid model-scale structure and single-degree-of-freedom deceleration tests, as explained in Chapter 4.

In Chapter 4, the ice penetration experiments in model ice were performed with a rigid structure, controlled oscillation, and a SDOF structure, and comparison of results showed that the peak global ice loads depended on the amount of time spent at low relative velocities where an ice strengthening effect developed. Although the experiments were performed in ethanol-doped model ice of nominally 30 mm thickness with a pile of 200 mm in diameter, the consistency of the results and their similarity with the literature

give support to the claim that the ice strengthening effect may be a general property of ice. This has implications for the so-called velocity effect and compliance effect in design of structures subject to dynamic ice-structure interaction.

The main conclusions from Chapter 4 are summarized as follows:

- The peak load-velocity dependence for ice penetration was a function of loading history with a critical dependence on the time spent at near-zero relative velocity (≥ 0.3 s).
- Rapid ice strengthening developed at low relative velocities, which persisted until the relative velocity reach about 20 mm s^{-1} and ice failure dissipated the strengthening effect.
- The rapid ice strengthening resulted in peak loads, under the conditions of a varying relative velocity, which exceeded those for a constant penetration velocity, but only when the relative velocity increased from near zero to above about 10 mm s^{-1} .
- The ice strengthening effect was observed during each cycle of ice-induced vibrations, specifically for frequency lock-in and intermittent crushing, thereby causing the high peak loads observed during such interaction.
- Based on the comparison of the peak loads as a function of relative velocity from the rigid structure tests and tests with controlled oscillation of the structure, the velocity effect and compliance effect during penetration seemed to originate from the same strengthening effect, implying that absolute peak loads on compliant structures would not exceed those for the lowest speeds on rigid structures.
- It is cautioned that assigning peak loads to the far-field ice drift speed for compliant structures may result in the attribution of high peak loads to velocities exceeding the actual relative velocities at which the peak loads develop.

Based on the ice tank tests, it was not possible to discern whether contact area variation, strengthening of the ice, or a combination thereof were responsible for the rapid ice strengthening. However, the delayed-elastic response of ice suggested by the results in both Chapter 3 and Chapter 4 support the finding that contact area variation could be a primary mechanism for the increase in global ice load following a duration of low relative velocity. Moreover, the literature suggests that local strain at failure of ice is rate-dependent as assumed by the phenomenological ice model from Hendrikse and Nord (2019), giving support to the validity of the model on a more physical basis beyond just contact area variation.

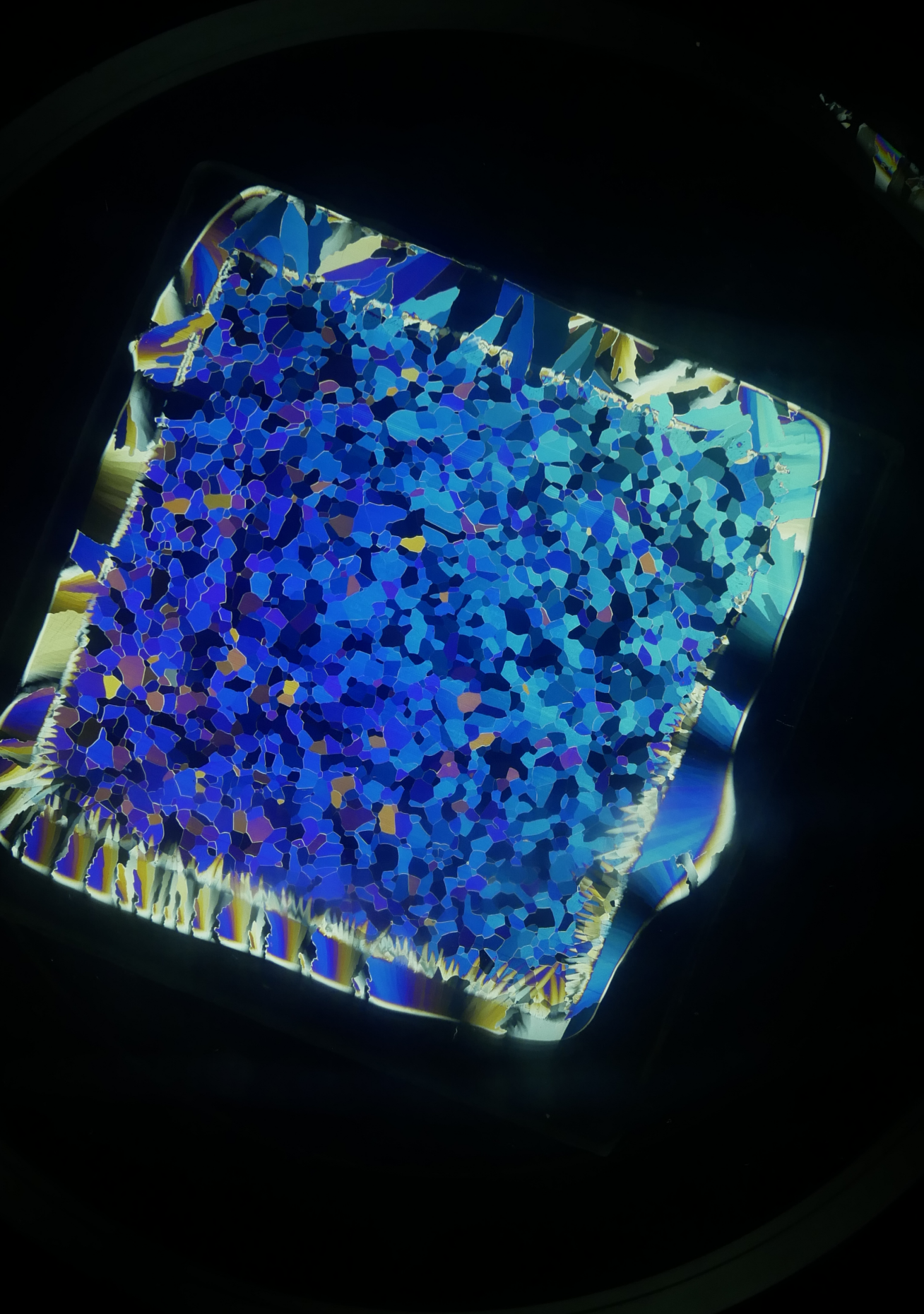
5.3. OUTLOOK

Upon reflection, the experimental findings in this thesis demonstrate a need to conduct more experiments on the constitutive behavior of ice under stress, strain, and strain rate conditions relevant for ice-induced vibrations. A quantification of the visco-elastic or visco-plastic behavior of columnar freshwater and saline ice could be instrumental in

formulating an ice model using mechanical properties of ice as opposed to phenomenological measurements. Further, detailed investigation of dislocation and grain boundary mechanics of ice under cyclic compressive loading would strengthen understanding of the mechanics behind delayed-elasticity and its contribution to the development of ice-induced vibrations. Specifically, application of compressive loading of ice with a haversine velocity waveform would resemble the loading during frequency lock-in and yield valuable results.

In a similar manner, ice penetration tests with a rigid structure ought to be performed as was done at the Aalto Ice and Wave Tank. However, attention should be paid to strain measurements in the ice sheet in proximity to the ice-structure interface. Information about the relationship between the strain and strain rate in the ice sheet and the relative velocity between ice and structure is crucial to more physical modeling and improved prediction of the development of ice-induced vibrations of vertically-sided offshore structures. Most critically, the phase relationship between the load measured on the structure and the strain measured in the ice sheet would be foundational in developing a model of dynamic ice-structure interaction which appropriately incorporates constitutive ice behavior.

There still remains uncertainty about the contact area and local pressure variations at the ice-structure interface during ice-induced vibrations. Detailed pressure mapping measurements at the ice-structure interface ought to accompany the aforementioned experiments. However, care must be taken to apply measurement techniques which respond elastically, such as piezoelectric methods, to avoid rise times and unintentional filtering which have been associated with semi-conductive ink-based tactile sensors.



REFERENCES

- Adobe Systems. (2005). Adobe RGB (1998) Color Image Encoding. *Adobe Systems Inc.*, 2704(05/2005), 1–20.
- Ashby, M. F., Palmer, A. C., Thouless, M., Goodman, D. J., Howard, M., Hallam, S. D., Murrell, S. A. F., Jones, N., Sanderson, T. J. O., & Ponter, A. R. S. (1986). Nonsimultaneous failure and ice loads on arctic structures. *Proceedings of the 18th Annual Offshore Technology Conference*, 399–404. <https://doi.org/10.4043/5127-ms>
- Azuma, N. (1994). A flow law for anisotropic ice and its application to ice sheets. *Earth and Planetary Science Letters*, 128(3-4), 601–614. [https://doi.org/10.1016/0012-821X\(94\)90173-2](https://doi.org/10.1016/0012-821X(94)90173-2)
- Azuma, N. (1995). A flow law for anisotropic polycrystalline ice under uniaxial compressive deformation. *Cold Regions Science and Technology*, 23(2), 137–147. [https://doi.org/10.1016/0165-232X\(94\)00011-L](https://doi.org/10.1016/0165-232X(94)00011-L)
- Barnes, P., Tabor, D., & Walker, J. F. (1971). The friction and creep of polycrystalline ice. *Proceedings of the Royal Society of London. A. Mathematical and Physical Sciences*, 324(1557), 127–155. <https://doi.org/10.1098/rspa.1971.0132>
- Barrette, P., Michel, B., & Stander, E. (1993). On the reproduction of ice from a common seed. *Journal of Crystal Growth*, 131(1-2), 153–156. [https://doi.org/10.1016/0022-0248\(93\)90408-O](https://doi.org/10.1016/0022-0248(93)90408-O)
- Barrette, P. D., & Jordaan, I. J. (2001). Creep of ice and microstructural changes under confining pressure. In S. Murakami & N. Ohno (Eds.), *Proceedings of the iutam symposium on creep in structures* (pp. 479–488). Kluwer Academic Publishers, Springer. https://doi.org/10.1007/978-94-015-9628-2{_}46
- Barrette, P. D., & Jordaan, I. J. (2003). Pressure-temperature effects on the compressive behavior of laboratory-grown and iceberg ice. *Cold Regions Science and Technology*, 36(1-3), 25–36. [https://doi.org/10.1016/S0165-232X\(02\)00077-0](https://doi.org/10.1016/S0165-232X(02)00077-0)
- Bjerkås, M., Lønøy, C., & Gürtner, A. (2013). Ice-induced vibrations and effects of ice temperature. *International Journal of Offshore and Polar Engineering*, 23(1), 9–14.
- Bjerkås, M., & Skiple, A. (2005). Occurrence of continuous and intermittent crushing during ice-structure interaction. *Proceedings of the 18th International Conference on Port and Ocean Engineering under Arctic Conditions*, 3, 1131–1140.
- Björk, B. (1981). *Ice-induced vibration of fixed offshore structures, Part 2: Experience with Baltic lighthouses* (tech. rep.). Marine structures and ships in ice, a joint Norwegian research project.
- Blackford, J. R. (2007). Sintering and microstructure of ice: a review. *Journal of Physics D: Applied Physics*, 40, R355–R385. <https://doi.org/10.1088/0022-3727/40/21/R02>

- Blenkarn, K. A. (1970). Measurement and analysis of ice forces on cook inlet structures. *Proceedings of the Annual Offshore Technology Conference*. <https://doi.org/10.4043/1261-ms>
- Bloss, F. D. (1961). *An introduction to the methods of optical crystallography*. Saunders College Publishing.
- Browne, T., Taylor, R., Jordaan, I., & Gürtner, A. (2013). Small-scale ice indentation tests with variable structural compliance. *Cold Regions Science and Technology*, *88*, 2–9. <https://doi.org/10.1016/j.coldregions.2012.12.006>
- Chauve, T., Montagnat, M., Lachaud, C., Georges, D., & Vacher, P. (2017). Strain field evolution at the ductile-to-brittle transition: A case study on ice. *Solid Earth*, *8*(5), 943–953. <https://doi.org/10.5194/se-8-943-2017>
- Chauve, T., Montagnat, M., & Vacher, P. (2015). Strain field evolution during dynamic recrystallization nucleation; A case study on ice. *Acta Materialia*, *101*, 116–124. <https://doi.org/10.1016/j.actamat.2015.08.033>
- Cole, D. M., Johnson, R. A., & Durell, G. D. (1998). Cyclic loading and creep response of aligned first-year sea ice. *Journal of Geophysical Research: Oceans*, *103*(C10), 21751–21758. <https://doi.org/10.1029/98JC01265>
- Cole, D. M. (1987). Strain-rate and grain-size effects in ice. *Journal of Glaciology*, *33*(115), 274–280. <https://doi.org/https://doi.org/10.3189/S0022143000008844>
- Cole, D. M. (1995). A model for the anelastic straining of saline ice subjected to cyclic loading. *Philosophical Magazine A*, *72*(1), 231–248. <https://doi.org/10.1080/01418619508239592>
- Cole, D. M. (1998). Modeling the cyclic loading response of sea ice. *International Journal of Solids and Structures*, *35*(31-32), 4067–4075. [https://doi.org/10.1016/S0020-7683\(97\)00301-6](https://doi.org/10.1016/S0020-7683(97)00301-6)
- Cole, D. M. (2001). The microstructure of ice and its influence on mechanical properties. *Engineering Fracture Mechanics*, *68*(17-18), 1797–1822. [https://doi.org/10.1016/S0013-7944\(01\)00031-5](https://doi.org/10.1016/S0013-7944(01)00031-5)
- Cole, D. M. (2021). A constitutive model for sea ice: physical basis, formulations, examples and applications. *Proceedings of the 26th International Conference on Port and Ocean Engineering under Arctic Conditions*, 1–12.
- Cole, D. M., & Durell, G. D. (1995). The cyclic loading of saline ice. *Philosophical Magazine A*, *72*(1), 209–229. <https://doi.org/10.1080/01418619508239591>
- Cole, D. (2020). On the physical basis for the creep of ice: the high temperature regime. *Journal of Glaciology*, *66*(257), 401–414. <https://doi.org/10.1017/jog.2020.15>
- Cormeau, A., Maes, M., Jordaan, I. J., & Timco, G. (1986). Analysis of strength reduction caused by Systems of Microcracks in Ice. *Proceedings of the 8th IAHR International Symposium on Ice*, *3*, 179–195.
- Craw, L., Qi, C., Prior, D. J., Goldsby, D. L., & Kim, D. (2018). Mechanics and microstructure of deformed natural anisotropic ice. *Journal of Structural Geology*, *115*(July), 152–166. <https://doi.org/10.1016/j.jsg.2018.07.014>
- Dempsey, J. P., Palmer, A. C., & Sodhi, D. S. (2001). High pressure zone formation during compressive ice failure. *Engineering Fracture Mechanics*, *68*(17-18), 1961–1974. [https://doi.org/10.1016/S0013-7944\(01\)00033-9](https://doi.org/10.1016/S0013-7944(01)00033-9)

- Ditlevsen, P., & Ditlevsen, S. (2023). Warning of a forthcoming collapse of the Atlantic meridional overturning circulation. *Nature Communications*, *14*(1), 4254. <https://doi.org/10.1038/s41467-023-39810-w>
- Durand, G., Gagliardini, O., Thorsteinsson, T., Svensson, A., Kipfstuhl, S., & Dahl-Jensen, D. (2006). Ice microstructure and fabric: an up-to-date approach for measuring textures. *Journal of Glaciology*, *52*(179), 619–630. <https://doi.org/10.3189/172756506781828377>
- Duval, P., Ashby, M. F., & Anderman, I. (1983). Rate-controlling processes in the creep of polycrystalline ice. *Journal of Physical Chemistry*, *87*(21), 4066–4074. <https://doi.org/10.1021/j100244a014>
- Eicken, H. (1993). Automated image analysis of ice thin sections — instrumentation, methods and extraction of stereological and textural parameters. *Journal of Glaciology*, *39*(132), 341–352. <https://doi.org/10.3189/S0022143000016002>
- Engelbrektson, A. (1977). Dynamic ice loads on a lighthouse structure. *Proceedings of the International Conference on Port and Ocean Engineering under Arctic Conditions (POAC)*, 654–663.
- Eranti, E. (1992). *Dynamic ice structure interaction. Theory and applications* (T. R. C. o. F. (VTT), Ed.; Doctoral dissertation). Helsinki University of Technology. Espoo, Finland.
- Eranti, E., Hayes, F. D., Määttänen, M., & Soong, T. T. (1981). Dynamic ice-structure interaction analysis for narrow vertical structures. *Proceedings of the 6th International Conference on Port and Ocean Engineering under Arctic Conditions*, *3*, 472–479.
- Faria, S. H., Weikusat, I., & Azuma, N. (2014). The microstructure of polar ice. Part II: state of the art. *Journal of Structural Geology*, *61*, 21–49. <https://doi.org/10.1016/j.jsg.2013.11.003>
- Forsberg, C. H. (2021). Radiation heat transfer. In *Heat transfer principles and applications* (pp. 343–389). Elsevier. <https://doi.org/10.1016/B978-0-12-802296-2.00009-3>
- Fueten, F., & Goodchild, J. S. (2001). Quartz c-axes orientation determination using the rotating polarizer microscope. *Journal of Structural Geology*, *23*(6-7), 895–902. [https://doi.org/10.1016/S0191-8141\(00\)00161-9](https://doi.org/10.1016/S0191-8141(00)00161-9)
- Gagnon, R. E. (1999). Consistent observations of ice crushing in laboratory tests and field experiments covering three orders of magnitude in scale. *Proceedings of the 15th International Conference on Port and Ocean Engineering under Arctic Conditions*, *2*, 858–869.
- Gagnon, R. E. (2012). An explanation for the Molikpaq May 12, 1986 event. *Cold Regions Science and Technology*, *82*, 75–93. <https://doi.org/10.1016/j.coldregions.2012.05.009>
- Gagnon, R. E., & Bugden, A. (2008). 2-dimensional edge crushing tests on thick sections of ice confined at the section face. *Proceedings of the 19th IAHR International Symposium on Ice*, *2*, 973–991.
- Gagnon, R. (2022). Spallation-based numerical simulations of ice-induced vibration of structures. *Cold Regions Science and Technology*, *194*(September 2021), 103465. <https://doi.org/10.1016/j.coldregions.2021.103465>
- Gay, M., & Weiss, J. (1999). Automatic reconstruction of polycrystalline ice microstructure from image analysis: application to the EPICA ice core at Dome Concordia,

- Antarctica. *Journal of Glaciology*, 45(151), 547–554. <https://doi.org/10.1017/S0022143000001416>
- Georges, D., Saletti, D., Montagnat, M., Forquin, P., & Hagenmuller, P. (2021). Influence of Porosity on Ice Dynamic Tensile Behavior as Assessed by Spalling Tests. *Journal of Dynamic Behavior of Materials*, 7(4), 575–590. <https://doi.org/10.1007/s40870-021-00300-z>
- Gharamti, I., Dempsey, J., Polojärvi, A., & Tuhkuri, J. (2021). Fracture of warm S2 columnar freshwater ice: size and rate effects. *Acta Materialia*, 202, 22–34. <https://doi.org/10.1016/j.actamat.2020.10.031>
- Glen, J. W. (1955). The creep of polycrystalline ice. *Proceedings of the Royal Society of London. Series A. Mathematical and Physical Sciences*, 228(1175), 519–538. <https://doi.org/10.1098/rspa.1955.0066>
- Gold, L. W. (1960). The cracking activity in ice during creep. *Canadian Journal of Physics*, 38(9), 1137–1148. <https://doi.org/10.1139/p60-122>
- Gonzalez, R. C., & Woods, R. E. (2008). *Digital image processing third edition* (3rd).
- Goodchild, J., & Fueten, F. (1998). Edge detection in petrographic images using the rotating polarizer stage. *Computers & Geosciences*, 24(8), 745–751. [https://doi.org/10.1016/S0098-3004\(98\)00054-5](https://doi.org/10.1016/S0098-3004(98)00054-5)
- Grennerat, F., Montagnat, M., Castelnau, O., Vacher, P., Moulinec, H., Suquet, P., & Duval, P. (2012). Experimental characterization of the intragranular strain field in columnar ice during transient creep. *Acta Materialia*, 60(8), 3655–3666. <https://doi.org/10.1016/j.actamat.2012.03.025>
- Gribanov, I., Taylor, R., & Sarracino, R. (2018). Cohesive zone micromechanical model for compressive and tensile failure of polycrystalline ice. *Engineering Fracture Mechanics*, 196(October 2017), 142–156. <https://doi.org/10.1016/j.engfracmech.2018.04.023>
- Guo, F. (2013). Analysis of the key parameters in ice induced frequency lock-in. *Proceedings of the 22nd International Conference on Port and Ocean Engineering under Arctic Conditions, POAC*, (POAC13-33), 10.
- Haapala, J. J., Ronkainen, I., Schmelzer, N., & Sztobryn, M. (2015). Recent Change—Sea Ice. In The BACC II Author Team (Ed.), *Second assessment of climate change for the baltic sea basin* (pp. 145–153). Springer, Cham. https://doi.org/10.1007/978-3-319-16006-1_{_}8
- Haasen, P., & Kelly, A. (1957). A yield phenomenon in face-centered cubic single crystals. *Acta Metallurgica*, 5(4), 192–199. [https://doi.org/10.1016/0001-6160\(57\)90165-7](https://doi.org/10.1016/0001-6160(57)90165-7)
- Habib, K. B., Taylor, R. S., Jordaan, I. J., & Bruneau, S. (2014). Experimental investigation of compressive failure of truncated conical ice specimens. *Proceedings of the ASME 2014 33rd International Conference on Ocean, Offshore and Arctic Engineering*, 1–8. <https://doi.org/https://doi.org/10.1115/OMAE2014-24184>
- Hammer, T. C., Owen, C. C., van den Berg, M., & Hendrikse, H. (2022). Classification of Ice-Induced Vibration Regimes of Offshore Wind Turbines. *Proceedings of the ASME 2022 41st International Conference on Ocean, Offshore and Arctic Engineering*, 6, 1–8. <https://doi.org/10.1115/OMAE2022-78972>
- Hammer, T. C., van Beek, K., Koning, J., & Hendrikse, H. (2021). A 2D test setup for scaled real-time hybrid tests of dynamic ice- structure interaction. *Proceedings*

- of the 26th International Conference on Port and Ocean Engineering under Arctic Conditions, 1–13.
- Hammer, T. C., Willems, T., & Hendrikse, H. (2023). Dynamic ice loads for offshore wind support structure design. *Marine Structures*, 87(November 2022), 103335. <https://doi.org/10.1016/j.marstruc.2022.103335>
- Hansen, D. P., & Wilen, L. A. (2002). Performance and applications of an automated c-axis ice-fabric analyzer. *Journal of Glaciology*, 48(160), 159–170. <https://doi.org/10.3189/172756502781831566>
- Hawkes, I., & Mellor, M. (1972). Deformation and Fracture of Ice Under Uniaxial Stress. *Journal of Glaciology*, 11(61), 103–131. <https://doi.org/10.3189/S002214300002253X>
- Heijkoop, A.-N., Nord, T. S., & Høyland, K. V. (2018). Strain-controlled cyclic compression of sea ice. *Proceedings of the 24th IAHR International Symposium on Ice*, 118–127.
- Heilbronner, R., & Barrett, S. (2014). *Image Analysis in Earth Sciences*. Springer Berlin Heidelberg. <https://doi.org/10.1007/978-3-642-10343-8>
- Heilbronner, R. P., & Pauli, C. (1993). Integrated spatial and orientation analysis of quartz c-axes by computer-aided microscopy. *Journal of Structural Geology*, 15(3-5), 369–382. [https://doi.org/10.1016/0191-8141\(93\)90133-U](https://doi.org/10.1016/0191-8141(93)90133-U)
- Hendrikse, H. (2017). *Ice-induced vibrations of vertically sided offshore structures* (Doctoral dissertation). Delft University of Technology. <https://doi.org/10.4233/uuid:325ebcfb-f920-400c-8ef6-21b2305b6920>
- Hendrikse, H. (2019). Dynamic ice actions in the revision of ISO 19906. *Proceedings of the 25th International Conference on Port and Ocean Engineering under Arctic Conditions, POAC, 2019-June*, 9.
- Hendrikse, H., Hammer, T. C., Owen, C. C., van den Berg, M., van Beek, K., Polojärvi, A., Puolakka, O., & Willems, T. (2022a). Ice Basin Tests for Ice-Induced Vibrations of Offshore Structures in the SHIVER Project. *Proceedings of the ASME 2022 41st International Conference on Ocean, Offshore and Arctic Engineering*, 6, 1–9. <https://doi.org/10.1115/OMAE2022-78507>
- Hendrikse, H., Hammer, T. C., van den Berg, M., Willems, T., Owen, C. C., van Beek, K., Ebben, N. J., Puolakka, O., & Polojärvi, A. (2022b). Experimental data from ice basin tests with vertically sided cylindrical structures. *Data in Brief*, 41, 107877. <https://doi.org/10.1016/j.dib.2022.107877>
- Hendrikse, H., & Koot, J. (2019). Consideration of ice drift in determining the contribution of ice-induced vibrations to structural fatigue. *Proceedings of the 25th International Conference on Port and Ocean Engineering under Arctic Conditions, POAC, 2019-June*, 1–14.
- Hendrikse, H., & Metrikine, A. (2015). Interpretation and prediction of ice induced vibrations based on contact area variation. *International Journal of Solids and Structures*, 75-76, 336–348. <https://doi.org/10.1016/j.ijsolstr.2015.08.023>
- Hendrikse, H., & Metrikine, A. (2016). Edge indentation of ice with a displacement-controlled oscillating cylindrical structure. *Cold Regions Science and Technology*, 121, 100–107. <https://doi.org/10.1016/j.coldregions.2015.10.013>
- Hendrikse, H., Metrikine, A., & Evers, K.-U. (2012). A method to measure the added mass and added damping in dynamic ice-structure interaction: Deciphering

- ice induced vibrations, part 3. In Li & Lu (Eds.), *Proceedings of the 21st iahr international symposium on ice* (pp. 972–984). IAHR.
- Hendrikse, H., & Nord, T. S. (2019). Dynamic response of an offshore structure interacting with an ice floe failing in crushing. *Marine Structures*, 65, 271–290. <https://doi.org/10.1016/j.marstruc.2019.01.012>
- Hendrikse, H., & Owen, C. C. (2023). Application of the suggested ice strength coefficients in ISO 19906 to intermittent crushing. *Proceedings of the 27th International Conference on Port and Ocean Engineering under Arctic Conditions*, 1–13.
- Hendrikse, H., Ziemer, G., & Owen, C. C. (2018). Experimental validation of a model for prediction of dynamic ice-structure interaction. *Cold Regions Science and Technology*, 151, 345–358. <https://doi.org/10.1016/j.coldregions.2018.04.003>
- Hetmanczyk, S., Heinonen, J., & Strobel, M. (2011). Dynamic ice load model in overall simulation of offshore wind turbines. *Proceedings of the 21st International Offshore and Polar Engineering Conference*, 347–352.
- Hill, J., & Lasca, N. (1971). An Improved Method for Determining Ice Fabrics. *Journal of Glaciology*, 10(58), 133–138. <https://doi.org/10.1017/S0022143000013071>
- Hirayama, K.-i., Schwarz, J., & Wu, H.-C. (1974). *An investigation of ice forces on vertical structures* (tech. rep.). Iowa Institute of Hydraulic Research, The University of Iowa. Iowa City, Iowa, USA.
- Hobbs, P. V. (1974). *Ice physics*. Clarendon Press.
- Hossain, R., Taylor, R., & Moro, L. (2018). An assessment of sensitivity of the self-excited modelling approach for simulating dynamic ice-structure interactions to changes in temperature and scale effects. *Ocean Engineering*, 165(May), 410–425. <https://doi.org/10.1016/j.oceaneng.2018.07.029>
- Huang, G., & Liu, P. (2009). A dynamic model for ice-induced vibration of structures. *Journal of Offshore Mechanics and Arctic Engineering*, 131(1), 1–6. <https://doi.org/10.1115/1.2979795>
- Huang, Y., Shi, Q., & Song, A. (2007). Model test study of the interaction between ice and a compliant vertical narrow structure. *Cold Regions Science and Technology*, 49(2), 151–160. <https://doi.org/10.1016/j.coldregions.2007.01.004>
- IEC 61400-3-1. (2019). *Wind energy generation systems - Part 3-1: Design requirements for fixed offshore wind turbines* (61400-3-1, tech. rep.). IEC. Geneva, Switzerland.
- Iliescu, D., & Schulson, E. M. (2002). Brittle compressive failure of ice: Monotonic versus cyclic loading. *Acta Materialia*, 50(8), 2163–2172. [https://doi.org/10.1016/S1359-6454\(02\)00060-5](https://doi.org/10.1016/S1359-6454(02)00060-5)
- Iliescu, D., Baker, I., & Chang, H. (2004). Determining the orientations of ice crystals using electron backscatter patterns. *Microscopy Research and Technique*, 63(4), 183–187. <https://doi.org/10.1002/jemt.20029>
- Iliescu, D., Murdza, A., Schulson, E. M., & Renshaw, C. E. (2017). Strengthening ice through cyclic loading. *Journal of Glaciology*, 63(240), 663–669. <https://doi.org/10.1017/jog.2017.32>
- Iliescu, D., & Schulson, E. M. (2004). The brittle compressive failure of fresh-water columnar ice loaded biaxially. *Acta Materialia*, 52(20), 5723–5735. <https://doi.org/10.1016/j.actamat.2004.07.027>

- IPCC. (2023). *IPCC, 2023: Climate Change 2023: Synthesis Report* (C. W. Team, H. Lee, & J. Romero, Eds.), Intergovernmental Panel on Climate Change. <https://doi.org/10.59327/IPCC/AR6-9789291691647>
- ISO 19906. (2019). *ISO 19906 Petroleum and natural gas industries - Arctic offshore structures* (tech. rep.). International Standard Organization.
- ITTC. (2014). *Test Methods for Model Ice Properties. ITTC Quality system manual, recommended procedures and guidelines* (tech. rep.). ITTC.
- Izumiyama, K., Irani, M. B., & Timco, G. W. (1994). Influence of compliance of structure on ice load. *Proceedings of the 12th IAHR International Symposium on Ice, 1*, 229–238.
- Izumiyama, K., & Uto, S. (1997). Ice loading on a compliant indenter. In H. Yamaguchi, K. Izumiyama, D. S. Sodhi, W. A. Nixon, & H. Kitagawa (Eds.), *Proceedings of the 16th international conference on offshore mechanics and arctic engineering* (pp. 431–436). OMAE.
- Jackson, L. C., Kahana, R., Graham, T., Ringer, M. A., Woollings, T., Mecking, J. V., & Wood, R. A. (2015). Global and European climate impacts of a slowdown of the AMOC in a high resolution GCM. *Climate Dynamics*, 45(11-12), 3299–3316. <https://doi.org/10.1007/s00382-015-2540-2>
- Jefferies, M. G., & Wright, W. H. (1988). Dynamic response of Molikpaq to ice-structure interaction. *Proceedings of the 7th International Conference on Offshore Mechanics and Arctic Engineering*, 4, 201–220.
- Jefferies, M., Kärnä, T., & Løset, S. (2008). Field data on the magnification of ice loads on vertical structures. In M. Jasek (Ed.), *Proceedings of the 19th iaahr international symposium on ice* (pp. 1325–1343). IAHR.
- Jeong, S., & Baddour, N. (2010). Comparison of characteristic failure frequency models for ice induced vibrations. *JP Journal of Solids and Structures*, 4(3), 115–137.
- Jevrejeva, S., Drabkin, V., Kostjukov, J., Lebedev, A., Leppäranta, M., Mironov, Y., Schmelzer, N., & Sztobryn, M. (2004). Baltic Sea ice seasons in the twentieth century. *Climate Research*, 25(3), 217–227. <https://doi.org/10.3354/cr025217>
- Ji, X., Karr, D. G., & Oterkus, E. (2018). A non-simultaneous dynamic ice-structure interaction model. *Ocean Engineering*, 166(August), 278–289. <https://doi.org/10.1016/j.oceaneng.2018.08.032>
- Ji, X., & Oterkus, E. (2016). A dynamic ice-structure interaction model for ice-induced vibrations by using van der pol equation. *Ocean Engineering*, 128(September), 147–152. <https://doi.org/10.1016/j.oceaneng.2016.10.028>
- Jones, S. J. (1997). High Strain-Rate Compression Tests on Ice. *The Journal of Physical Chemistry B*, 101(32), 6099–6101. <https://doi.org/10.1021/jp963162j>
- Jones, S. J. (2007). A review of the strength of iceberg and other freshwater ice and the effect of temperature. *Cold Regions Science and Technology*, 47(3), 256–262. <https://doi.org/10.1016/j.coldregions.2006.10.002>
- Jordaan, I., & Barrette, P. (2014). Mechanics of dynamic ice failure against vertical structures. *Proceedings of the ASME 2014 33rd International Conference on Offshore Mechanics and Arctic Engineering*, 10, 1–7. <https://doi.org/10.1115/OMAE2014-24406>

- Jordaan, I., O'Rourke, B., Turner, J., Moore, P., & Ralph, F. (2016). Estimation of ice loads using mechanics of ice failure in compression. *Arctic Technology Conference 2016*, 1–12. <https://doi.org/10.4043/27387-ms>
- Jordaan, I. J. (2001). Mechanics of ice-structure interaction. *Engineering Fracture Mechanics*, 68(17-18), 1923–1960. [https://doi.org/10.1016/S0013-7944\(01\)00032-7](https://doi.org/10.1016/S0013-7944(01)00032-7)
- Jordaan, I. J., Stone, B. M., McKenna, R. F., & Fuglem, M. K. (1992). Effect of microcracking on the deformation of ice. *Canadian Geotechnical Journal*, 29(1), 143–150. <https://doi.org/10.1139/t92-015>
- Kamb, W. B. (1962). Refraction corrections for universal stage measurements. I. Uniaxial Crystals. *American Mineralogist*, 47(3-4_Part_1), 227–245.
- Kamesaki, K., Tsukuda, H., & Yamauchi, Y. (1997). Indentation test with vertically placed ice sheet. In H. Yamaguchi, K. Izumiyama, D. S. Sodhi, W. A. Nixon, & H. Kitagawa (Eds.), *Proceedings of the 16th international conference on offshore mechanics and arctic engineering and proceedings of the 14th international conference on port and ocean engineering under arctic conditions* (pp. 245–250). ASME, OMAE, POAC.
- Kamesaki, K., Tsukuda, H., & Yamauchi, Y. (1998). Experimental studies on ice flaking characteristics of compliant indentors. *Proceedings of the 8th International Offshore and Polar Engineering Conference*, 2, 381–388.
- Kamesaki, K., Yamauchi, Y., & Kärnä, T. (1996). Ice force as a function of structural compliance. *Proceedings of the 13th IAHR International Symposium on Ice*, 1, 395–402.
- Kärnä, T., Andersen, H., Gürtner, A., Metrikine, A., Sodhi, D. S., Loo, M., Kuiper, G., Gibson, R., Fenz, D., Muggeridge, K., Wallenburg, C., Wu, J.-F., & Jefferies, M. G. (2013). Ice-induced vibrations of offshore structures - looking beyond ISO 19906. *Proceedings of the 22nd International Conference on Port and Ocean Engineering under Arctic Conditions*, 1–12.
- Kärnä, T., Kamesaki, K., & Tsukuda, H. (1999). Numerical model for dynamic ice-structure interaction. *Computers and Structures*, 72(4), 645–658. [https://doi.org/10.1016/S0045-7949\(98\)00337-X](https://doi.org/10.1016/S0045-7949(98)00337-X)
- Kärnä, T. (1992). A procedure for dynamic soil-structure-ice interaction. *Proceedings of the 2nd International Offshore and Polar Engineering Conference*, 2, 764–771.
- Kärnä, T. (2010). *Physical mechanisms in different kinds of ice-induced vibrations*, Ice Induced Vibrations JIP Workshop.
- Kärnä, T. (2011a). *Full-scale data analyses of frequency lock-in*, Ice Induced Vibrations JIP - WP 1.2.
- Kärnä, T. (2011b). *Laboratory and medium scale data analyses*, Ice Induced Vibrations JIP - WP 1.2.
- Kärnä, T., Gravesen, H., Fransson, L., & Løset, S. (2010). Simulation of multi-modal vibrations due to ice actions. *Proceedings of the 20th IAHR International Symposium on Ice*, (June), 1–13.
- Kärnä, T., Guo, F., Løset, S., & Määttänen, M. (2008). Small-scale data on magnification of ice loads on vertical structures. In M. Jasek (Ed.), *Proceedings of the 19th iaahr international symposium on ice* (pp. 1313–1324). IAHR.

- Kärnä, T., & Järvinen, E. (1999). Symmetric and asymmetric flaking process. *Proceedings of the 15th International Conference on Port and Ocean Engineering under Arctic Conditions*, 3, 988–1000.
- Kärnä, T., Jochmann, P., & Kolari, K. (2001). *Observed ice - structure interactions in winters 2000 and 2001*, STRICE.
- Kärnä, T., & Masterson, D. M. (2011). Data for crushing formula. *Proceedings of the 21st International Conference on Port and Ocean Engineering under Arctic Conditions*, 1, 1–12.
- Kavanagh, M. B. (2018). *Time-dependent aspects of fracture in ice* (Doctoral dissertation May). Memorial University of Newfoundland.
- Kolari, K. (2017). A complete three-dimensional continuum model of wing-crack growth in granular brittle solids. *International Journal of Solids and Structures*, 115-116, 27–42. <https://doi.org/10.1016/j.ijsolstr.2017.02.012>
- KorzHAVIN, K. (1962). *Action of Ice on Engineering Structures* (tech. rep.). Siberian Branch of USSR Academy of Sciences.
- Kry, P. R. (1978). A statistical prediction of effective ice crushing stresses on wide structures. *Proceedings of the 5th IAHR International Symposium on Ice*, 1, 33–47.
- Kuiper, G. (2013). Correlation curves for brittle and ductile ice failure based on full-scale data. *Proceedings of the 22nd International Conference on Port and Ocean Engineering under Arctic Conditions*, POAC, (POAC13-133), 1–12.
- Kuutti, J., & Kolari, K. (2013). Simulation of dynamic ice indentation failure. *Proceedings of the International Conference on Port and Ocean Engineering under Arctic Conditions*, POAC, (POAC13_142), 1–15.
- Lange, M. A. (1988). A Computer-Controlled System for Ice-Fabric Analysis on a Rigsby Stage. *Annals of Glaciology*, 10, 92–94. <https://doi.org/10.3189/S0260305500004237>
- Langway, C. C. J. (1958). *Ice Fabrics and the Universal Stage* (tech. rep. August). U.S. Army Snow Ice and Permafrost Research Establishment, Corps of Engineers. Wilmette, Illinois, USA.
- Linge Johnsen, S. A., Bollman, J., Lee, H. W., & Zhou, Y. (2018). Accurate representation of interference colours (Michel-Lévy chart): from rendering to image colour correction. *Journal of Microscopy*, 269(3), 321–337. <https://doi.org/10.1111/jmi.12641>
- Løset, S., Shkhinek, K. N., Gudmestad, O. T., & Høyland, K. V. (2006). *Actions from ice on Arctic offshore and coastal structures* (N. M. Bashakova, N. K. Beliakova, & O. V. Shilkova, Eds.).
- Määttänen, M. (1981). Laboratory tests for dynamic ice-structure interaction. *Engineering Structures*, 3(2), 111–116. [https://doi.org/10.1016/0141-0296\(81\)90037-7](https://doi.org/10.1016/0141-0296(81)90037-7)
- Määttänen, M. (1975). Experience of Ice Forces Against a Steel Lighthouse Mounted on the Seabed and Proposed Construction Refinements. *Proceedings of the 3rd International Conference on Port and Ocean Engineering under Arctic Conditions (POAC'75)*, 2, 857–869.
- Määttänen, M. (1983). *Dynamic ice-structure interaction during continuous crushing* (tech. rep.). U.S. Army Cold Regions Research and Engineering Laboratory. Hanover, New Hampshire, USA.

- Määttänen, M. (1988). Ice-induced vibrations of structures - self-excitation. *Proceedings of the 9th IAHR International Symposium on Ice*, 2, 658–665.
- Määttänen, M. (2008). Ice velocity limit to frequency lock-in vibrations. *Proceedings of the 19th IAHR International Symposium on Ice*, 1265–1276.
- Määttänen, M., Marjavaara, P., Saarinen, S., & Laakso, M. (2011). Ice crushing tests with variable structural flexibility. *Cold Regions Science and Technology*, 67(3), 120–128. <https://doi.org/10.1016/j.coldregions.2011.03.004>
- Määttänen, M. P. (1998). Numerical model for ice-induced vibration load lock-in and synchronization. *Proceedings of the 14th IAHR International Symposium on Ice*, 2, 923–930.
- Matlock, H., Dawkins, W. P., & Panak, J. J. (1969). A model for the prediction of ice-structure interaction. *Proceedings of the Annual Offshore Technology Conference, May*, 687–694. <https://doi.org/10.4043/1066-ms>
- Matsushita, H., Kamio, Z., Sakai, M., Takeuchi, T., Terashima, T., Akagawa, S., Nakazawa, N., & Saeki, H. (2000). Consideration of failure mode of a sea ice sheet. *Proceedings of the 10th International Offshore and Polar Engineering Conference*, 1, 577–582.
- Meglis, I. L., Melanson, P. M., & Jordaan, I. J. (1999). Microstructural change in ice: II. Creep behavior under triaxial stress conditions. *Journal of Glaciology*, 45(151), 438–448. <https://doi.org/10.3189/s0022143000001271>
- Melanson, P. M., Meglis, I. L., Jordaan, I. J., & Stone, B. M. (1999). Microstructural change in ice: I. Constant-deformation-rate tests under triaxial stress conditions. *Journal of Glaciology*, 45(151), 417–422. <https://doi.org/10.3189/s0022143000001271>
- Melgosa, M. (2000). Testing CIELAB-Based Color-Difference Formulas. *Color Research and Application*, 25(1), 49–55. [https://doi.org/10.1002/\(SICI\)1520-6378\(200002\)25:1<49::AID-COL7>3.0.CO;2-4](https://doi.org/10.1002/(SICI)1520-6378(200002)25:1<49::AID-COL7>3.0.CO;2-4)
- Mellor, M., & Cole, D. M. (1983). Stress/strain/time relations for ice under uniaxial compression. *Cold Regions Science and Technology*, 6(3), 207–230. [https://doi.org/10.1016/0165-232X\(83\)90043-5](https://doi.org/10.1016/0165-232X(83)90043-5)
- Michel, B., & Ramseier, R. O. (1971). Classification of river and lake ice. *Canadian Geotechnical Journal*, 8(1), 36–45. <https://doi.org/10.1139/t71-004>
- Michel, B., & Toussaint, N. (1977). Mechanisms and theory of indentation of ice plates. *Journal of Glaciology*, 19(81), 285–300.
- Montagnat, M., Bourcier, M., Philip, A., Bons, P. D., Bauer, C. C., Deconinck, P., & Hereil, P. (2021). Texture characterization of some large hailstones with an automated technique. *Journal of Glaciology*, 67(266), 1190–1204. <https://doi.org/10.1017/jog.2021.66>
- Monz, M. E., Hudleston, P. J., Prior, D. J., Michels, Z., Fan, S., Negrini, M., Langhorne, P. J., & Qi, C. (2021). Full crystallographic orientation (c and a axes) of warm, coarse-grained ice in a shear-dominated setting: a case study, Storglaciären, Sweden. *The Cryosphere*, 15(1), 303–324. <https://doi.org/10.5194/tc-15-303-2021>
- Morgan, V., Davis, E., & Wehrle, E. (1984). A Rigsby stage with remote computer compatible output. *Cold Regions Science and Technology*, 10(1), 89–92. [https://doi.org/10.1016/0165-232X\(84\)90036-3](https://doi.org/10.1016/0165-232X(84)90036-3)

- Morsy, U. A.-E. (1995). *Non-linear finite element modelling of dynamic loads on offshore structures* (Doctoral dissertation). University of Calgary. <https://doi.org/http://dx.doi.org/10.11575/PRISM/15646>
- Muhonen, A. (1996). *Evaluation of three ice-structure interaction models* (Doctoral dissertation). Helsinki University of Technology.
- Muhonen, A., Kärnä, T., Eranti, E., Riska, K., Järvinen, E., & Lehmus, E. (1992). *Laboratory indentation tests with thick freshwater ice, Volume I* (tech. rep.). Technical Research Centre of Finland (VTT). Espoo, Finland.
- Murdza, A., Marchenko, A., Schulson, E. M., & Renshaw, C. E. (2021a). Cyclic strengthening of lake ice. *Journal of Glaciology*, 67(261), 182–185. <https://doi.org/10.1017/jog.2020.86>
- Murdza, A., Schulson, E. M., & Renshaw, C. E. (2020). Strengthening of columnar-grained freshwater ice through cyclic flexural loading. *Journal of Glaciology*, 66(258), 556–566. <https://doi.org/10.1017/jog.2020.31>
- Murdza, A., Schulson, E. M., & Renshaw, C. E. (2021b). Behavior of saline ice under cyclic flexural loading. *The Cryosphere*, 15(5), 2415–2428. <https://doi.org/10.5194/tc-15-2415-2021>
- Murdza, A., Schulson, E. M., Renshaw, C. E., & Polojärvi, A. (2022). Rapid Healing of Thermal Cracks in Ice. *Geophysical Research Letters*, 49(17), 1–6. <https://doi.org/10.1029/2022GL099771>
- Murphy, D. B. (2001). *Fundamentals of light microscopy and electronic imaging* (First edit, Vol. 68). John Wiley & Sons, Inc.
- Nakazawa, N., & Sodhi, D. S. (1990). *Ice forces on flat, vertical indentors pushed through floating ice sheets* (May), U.S. Army Corps of Engineers, Cold Regions Research and Engineering Laboratory.
- Neill, C. R. (1976). Dynamic ice forces on piers and piles. An assessment of design guidelines in the light of recent research. *Canadian Journal of Civil Engineering*, 3(2), 305–341. <https://doi.org/10.1139/l76-030>
- Nord, T. S., Lourens, E. M., Määttänen, M., Øiseth, O., & Høyland, K. V. (2015). Laboratory experiments to study ice-induced vibrations of scaled model structures during their interaction with level ice at different ice velocities. *Cold Regions Science and Technology*, 119, 1–15. <https://doi.org/10.1016/j.coldregions.2015.06.017>
- O'Connor, D., West, B., Haehnel, R., Asenath-Smith, E., & Cole, D. (2020). A viscoelastic integral formulation and numerical implementation of an isotropic constitutive model of saline ice. *Cold Regions Science and Technology*, 171(December 2019), 102983. <https://doi.org/10.1016/j.coldregions.2019.102983>
- O'Rourke, B. J., Jordaan, I. J., Taylor, R. S., & Gürtner, A. (2016). Experimental investigation of oscillation of loads in ice high-pressure zones, part 1: Single indenter system. *Cold Regions Science and Technology*, 124, 25–39. <https://doi.org/10.1016/j.coldregions.2015.12.005>
- Owen, C. C., Hammer, T. C., & Hendrikse, H. (2022). Test setup for compressive loading of confined ice thick sections viewed with in-situ cross-polarization imaging. *Proceedings of the 26th IAHR International Symposium on Ice*, (June), 1–10.
- Owen, C. C., Hammer, T. C., & Hendrikse, H. (2023a). Hysteresis and dichotomous mechanics in cyclic crushing failure of confined freshwater columnar ice. *Cold*

- Regions Science and Technology*, 209(December 2022), 103816. <https://doi.org/10.1016/j.coldregions.2023.103816>
- Owen, C. C., Hammer, T. C., & Hendrikse, H. (2023b). Peak loads during dynamic ice-structure interaction caused by rapid ice strengthening at near-zero relative velocity. *Cold Regions Science and Technology*, 211(April), 103864. <https://doi.org/10.1016/j.coldregions.2023.103864>
- Owen, C. C., & Hendrikse, H. (2021). Simulation and analysis of ice-induced vibrations experienced by Molikpaq during the May 12, 1986 event. *Proceedings of the 26th International Conference on Port and Ocean Engineering under Arctic Conditions, POAC, 2021-June*, 1–14.
- Owen, C. C., & Hendrikse, H. (2023). An initial study of interference coloration for quantifying the texture and fabric of ice. *Cold Regions Science and Technology*, 206, 103735. <https://doi.org/10.1016/j.coldregions.2022.103735>
- Owen, C. C., & Hendrikse, H. (2018). Ice-induced vibrations of model structures with various dynamic properties. *Proceedings of the 24th IAHR International Symposium on Ice*, 376–385.
- Owen, C. C., & Hendrikse, H. (2019). A study of the transition ice speed from intermittent crushing to frequency lock-in vibrations based on model-scale experiments. *Proceedings of the 25th International Conference on Port and Ocean Engineering under Arctic Conditions*, 13.
- Ozersky, T., Bramburger, A. J., Elgin, A. K., Vanderploeg, H. A., Wang, J., Austin, J. A., Carrick, H. J., Chavarie, L., Depew, D. C., Fisk, A. T., Hampton, S. E., Hinchey, E. K., North, R. L., Wells, M. G., Xenopoulos, M. A., Coleman, M. L., Duhaime, M. B., Fujisaki-Manome, A., McKay, R. M., ... Zastepa, A. (2021). The Changing Face of Winter: Lessons and Questions From the Laurentian Great Lakes. *Journal of Geophysical Research: Biogeosciences*, 126(6). <https://doi.org/10.1029/2021JG006247>
- Palmer, A., Qianjin, Y., & Fengwei, G. (2010). Ice-induced vibrations and scaling. *Cold Regions Science and Technology*, 60(3), 189–192. <https://doi.org/10.1016/j.coldregions.2009.11.005>
- Pascale, D. (2003). *A review of RGB color spaces... from xyY to R'G'B'* (tech. rep.). The BabelColor Company. Montréal, Quebec, Canada.
- Pauling, L. (1935). The Structure and Entropy of Ice and of Other Crystals with Some Randomness of Atomic Arrangement. *Journal of the American Chemical Society*, 57(12), 2680–2684. <https://doi.org/https://doi.org/10.3189/S0022143000215608>
- Perey, F. G. J., & Pounder, E. R. (1958). Crystal orientation in ice sheets. *Canadian Journal of Physics*, 36(4), 494–502. <https://doi.org/10.1139/p58-050>
- Peternell, M., Russell-Head, D. S., & Wilson, C. J. L. (2011). A technique for recording polycrystalline structure and orientation during in situ deformation cycles of rock analogues using an automated fabric analyser. *Journal of Microscopy*, 242(2), 181–188. <https://doi.org/10.1111/j.1365-2818.2010.03456.x>
- Peternell, M., Dierckx, M., Wilson, C. J., & Piazzolo, S. (2014). Quantification of the microstructural evolution of polycrystalline fabrics using FAME: Application to in situ deformation of ice. *Journal of Structural Geology*, 61, 109–122. <https://doi.org/10.1016/j.jsg.2013.05.005>

- Petrenko, V. F., & Whitworth, R. W. (1999). *Physics of Ice*. Oxford University Press. <https://doi.org/10.1093/acprof:oso/9780198518945.001.0001>
- Peyton, H. (1968). Sea ice forces. *Proceedings of Conference on Ice Pressures Against Structures*, 117–123.
- Piazolo, S., Bons, P. D., Griera, A., Llorens, M. G., Gomez-Rivas, E., Koehn, D., Wheeler, J., Gardner, R., Godinho, J. R., Evans, L., Lebensohn, R. A., & Jessell, M. W. (2019). A review of numerical modelling of the dynamics of microstructural development in rocks and ice: Past, present and future. *Journal of Structural Geology*, 125(November 2017), 111–123. <https://doi.org/10.1016/j.jsg.2018.05.025>
- Ponter, A., Palmer, A., Goodman, D., Ashby, M., Evans, A., & Hutchinson, J. (1983). The force exerted by a moving ice sheet on an offshore structure Part I. The creep mode. *Cold Regions Science and Technology*, 8(2), 109–118. [https://doi.org/10.1016/0165-232X\(83\)90002-2](https://doi.org/10.1016/0165-232X(83)90002-2)
- Pörtner, H.-O., Roberts, D. C., Masson-Delmotte, V., Zhai, P., Poloczanska, E., Mintenbeck, K., Tignor, M., Alegría, A., Nicolai, M., Okem, A., Petzold, J., Rama, B., & Weyer, N. M. (2019). *IPCC, 2019: Technical Summary*, Intergovernmental Panel on Climate Change. <https://doi.org/10.1017/9781009157964.002>
- Pounder, E. R. (1965). *Physics of ice*. Pergamon Press.
- Price, G. P. (1973). The photometric method in microstructural analysis. *American Journal of Science*, 273(6), 523–537. <https://doi.org/10.2475/ajs.273.6.523>
- Raith, M. M., Raase, P., & Reinhardt, J. (2012). *Guide to thin section microscopy* (Second). Mineral Society of America.
- Ravi-Chandar, K., Adamson, B., Lazo, J., & Dempsey, J. P. (1994). Stress-optic effect in ice. *Applied Physics Letters*, 64(10), 1183–1185. <https://doi.org/10.1063/1.110883>
- Ren, S., Mazière, M., Forest, S., Morgener, T. F., & Rousselier, G. (2017). A constitutive model accounting for strain ageing effects on work-hardening. Application to a C–Mn steel. *Comptes Rendus Mécanique*, 345(12), 908–921. <https://doi.org/10.1016/j.crme.2017.09.005>
- Rigsby, G. P. (1951). Crystal fabric studies on Emmons Glacier Mount Rainier, Washington. *The Journal of Geology*, 59(6), 590–598.
- Riska, K., & Frederking, R. M. W. (1987). Ice load penetration modelling. *Proceedings of the 9th International Conference on Port and Ocean Engineering under Arctic Conditions*, 1, 317–327.
- Riska, K., Baarman, L., & Muhonen, A. (1993). *Modelling of Ice Induced Vibration of Slender Offshore Structures*, Helsinki University of Technology, Arctic Offshore Research Centre.
- Rist, M., & Murrell, S. (1994). Ice triaxial deformation and fracture. *Journal of Glaciology*, 40(135), 305–318. <https://doi.org/10.3189/s002214300007395>
- Saeki, H., Ono, T., Nakazawa, N., Sakai, M., & Tanaka, S. (1986). The coefficient of friction between sea ice and various materials used in offshore structures. *Journal of Energy Resources Technology*, 108(1), 65–71. <https://doi.org/10.1115/1.3231243>
- Saeki, H., Hirayama, K. i., Takeuchi, T., Akagawa, S., Kawamura, M., Nakazawa, N., Terashima, T., Matsushita, H., Sakai, M., & Honda, H. (1998). Medium-scale field indentation test (MSFIT): results of 1997 winter tests. *Proceedings of the 8th International Offshore and Polar Engineering Conference*, 2, 364–369.

- Sakai, M., Aoshima, M., & Saeki, H. (1998). Measurements of ice sheet strain area during ice/vertical sided structure interactions using strain gages in field indentation tests. *Proceedings of the 8th International Offshore and Polar Engineering Conference*, 2, 376–380.
- Sammonds, P., Montagnat, M., Bons, P., & Schneebeli, M. (2017). Ice microstructures and microdynamics. *Philosophical Transactions of the Royal Society A: Mathematical, Physical and Engineering Sciences*, 375(20160438), 5. <https://doi.org/10.1098/rsta.2016.0438>
- Sanderson, T. J. O. (1988). *Ice mechanics: risks to offshore structures*. Graham & Trotman.
- Schulson, E. M., Gies, M. C., Lasonde, G. J., & Nixon, W. A. (1989). The effect of the specimen-platen interface on internal cracking and brittle fracture of ice under compression: high-speed photography. *Journal of Glaciology*, 35(121), 378–382. <https://doi.org/https://doi.org/10.3189/S0022143000009308>
- Schulson, E. (1990). The brittle compressive fracture of ice. *Acta Metallurgica et Materialia*, 38(10), 1963–1976. [https://doi.org/10.1016/0956-7151\(90\)90308-4](https://doi.org/10.1016/0956-7151(90)90308-4)
- Schulson, E. M., & Duval, P. (2009). *Creep and fracture of ice*. Cambridge University Press. <https://doi.org/10.1017/CBO9780511581397>
- Schulson, E. M., Murdza, A., & Renshaw, C. E. (2019). *Mechanisms of Cyclic Strengthening and Recovery of Polycrystalline Ice* (IUTAM, Ed.; Vol. 39). Springer International Publishing. <https://doi.org/10.1007/978-3-030-80439-8>1
- Schwarz, J., & Weeks, W. F. (1977). Engineering Properties of Sea Ice. *Journal of Glaciology*, 19(81), 499–531. <https://doi.org/10.3189/S0022143000029476>
- Schwarz, J. (1994). Low level ice forces. *Proceedings of the 12th IAHR International Symposium on Ice*, 3, 1040–1050.
- Schwarz, J., & Jochmann, P. (2001). Ice force measurements within the LOLEIF-project. *Proceedings of the 16th International Conference on Port and Ocean Engineering under Arctic Conditions (POAC'01)*, 2, 669–682.
- Seidemann, M., Prior, D. J., Golding, N., Durham, W. B., Lilly, K., & Vaughan, M. J. (2020). The role of kink boundaries in the deformation and recrystallisation of polycrystalline ice. *Journal of Structural Geology*, 136(February), 104010. <https://doi.org/10.1016/j.jsg.2020.104010>
- Seymour-Pierce, A., Lishman, B., & Sammonds, P. (2017). Recrystallization and damage of ice in winter sports. *Philosophical Transactions of the Royal Society A: Mathematical, Physical and Engineering Sciences*, 375(2086), 20150353. <https://doi.org/10.1098/rsta.2015.0353>
- Shazly, M., Prakash, V., & Lerch, B. A. (2009). High strain-rate behavior of ice under uniaxial compression. *International Journal of Solids and Structures*, 46(6), 1499–1515. <https://doi.org/10.1016/j.ijsolstr.2008.11.020>
- Shestov, A. (2018). Birefringence in ice crystals. Principles and application in sea ice microstructure studies. In G. Arbatskaia (Ed.), *Proceedings of the 24th iaahr international symposium on ice* (pp. 248–257). IAHR.
- Shkhinek, K. (2010). *Velocity effects in compressive failure of an ice sheet against a vertical structure* (tech. rep.). IIV JIP Workshop on ice mechanics. Oslo, Norway.
- Shokr, M., & Sinha, N. K. (2015). *Sea ice: Physics and remote sensing*. Jogn Wiley & Sons Inc.

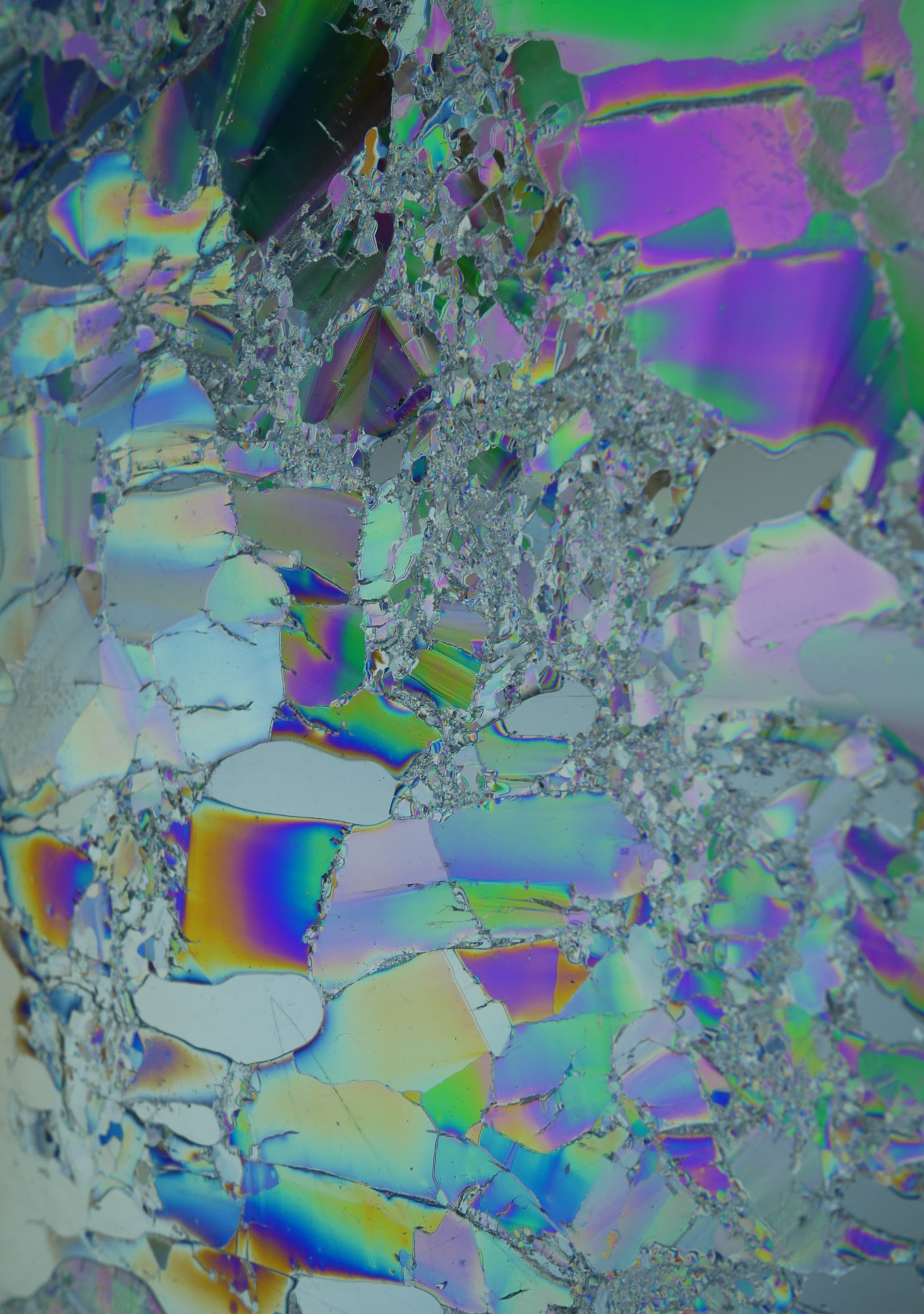
- Singh, S. K., Timco, G. W., Frederking, R. M. W., & Jordaan, I. J. (1990). Tests of ice crushing on a flexible structure. *Proceedings of the 9th Offshore Mechanics and Arctic Engineering Symposium*, 4, 89–94.
- Sinha, N. K. (1989). Microcrack-enhanced creep in polycrystalline material at elevated temperature. *Acta Metallurgica*, 37(11), 3107–3118. [https://doi.org/https://doi.org/10.1016/0001-6160\(89\)90346-5](https://doi.org/https://doi.org/10.1016/0001-6160(89)90346-5)
- Sinha, N. K. (2011). Borehole indenter - A tool for assessing in-situ bulk ice strength and micromechanics. *Cold Regions Science and Technology*, 69(1), 21–38. <https://doi.org/10.1016/j.coldregions.2011.07.009>
- Sinha, N. (1977). Technique for Studying Structure of Sea Ice. *Journal of Glaciology*, 18(79), 315–324. <https://doi.org/10.3189/S0022143000021390>
- Snyder, S. A., Schulson, E. M., & Renshaw, C. E. (2015). The role of damage and recrystallization in the elastic properties of columnar ice. *Journal of Glaciology*, 61(227), 461–480. <https://doi.org/10.3189/2015JoG14J225>
- Snyder, S. A., Schulson, E. M., & Renshaw, C. E. (2016). Effects of prestrain on the ductile-to-brittle transition of ice. *Acta Materialia*, 108, 110–127. <https://doi.org/10.1016/j.actamat.2016.01.062>
- Sodhi, D. S. (1988). Ice-induced vibrations of structures. *Proceedings of the 9th IAHR International Symposium on Ice*, 625–657.
- Sodhi, D. S. (1991a). Effective pressures measured during indentation tests in freshwater ice. *Proceedings of the 6th International Cold Regions Engineering Specialty Conference*, 619–627.
- Sodhi, D. S. (1991b). Ice-structure interaction during indentation tests. In S. Jones, R. F. McKenna, J. Tillotson, & I. Jordaan (Eds.), *Proceedings of the iutam-iahr symposium on ice-structure interaction* (pp. 619–640). Springer-Verlag Berlin Heidelberg. https://doi.org/10.1007/978-3-642-84100-2_{_}31
- Sodhi, D. S. (1995). An ice-structure interaction model. In A. P. S. Selvadurai & M. J. Boulon (Eds.), *Mechanics of geomaterial interfaces* (pp. 57–75). Elsevier Science B.V. [https://doi.org/10.1016/S0922-5382\(06\)80006-1](https://doi.org/10.1016/S0922-5382(06)80006-1)
- Sodhi, D. S. (1998). Nonsimultaneous crushing during edge indentation of freshwater ice sheets. *Cold Regions Science and Technology*, 27(3), 179–195. [https://doi.org/10.1016/S0165-232X\(98\)00010-X](https://doi.org/10.1016/S0165-232X(98)00010-X)
- Sodhi, D. S. (2001). Crushing failure during ice-structure interaction. *Engineering Fracture Mechanics*, 68(17-18), 1889–1921. [https://doi.org/10.1016/S0013-7944\(01\)00038-8](https://doi.org/10.1016/S0013-7944(01)00038-8)
- Sodhi, D. S., & Haehnel, R. B. (2003). Crushing ice forces on structures. *Journal of Cold Regions Engineering*, 17(4), 153–170. [https://doi.org/10.1061/\(ASCE\)0887-381X\(2003\)17:4\(153\)](https://doi.org/10.1061/(ASCE)0887-381X(2003)17:4(153))
- Sodhi, D. S., Takeuchi, T., Nakazawa, N., Akagawa, S., & Saeki, H. (1998). Medium-scale indentation tests on sea ice at various speeds. *Cold Regions Science and Technology*, 28(3), 161–182. [https://doi.org/10.1016/S0165-232X\(98\)00017-2](https://doi.org/10.1016/S0165-232X(98)00017-2)
- Sopper, R. (2016). *Experimental investigation of water, snow and granular ice effects on ice failure processes and impact loads* (Doctoral dissertation May). Memorial University of Newfoundland.

- Sopper, R., Daley, C., Colbourne, B., & Bruneau, S. (2017). The influence of water, snow and granular ice on ice failure processes, ice load magnitude and process pressure. *Cold Regions Science and Technology*, 139(June 2016), 51–64. <https://doi.org/10.1016/j.coldregions.2017.04.006>
- Sørensen, B. E. (2013). A revised Michel-Lévy interference colour chart based on first-principles calculations. *European Journal of Mineralogy*, 25(1), 5–10. <https://doi.org/10.1127/0935-1221/2013/0025-2252>
- Stockman, A., Rider, A., Henning, B., Baabbad, R., Mylonas, D., & Andrikopoulos, P. (2020). CVRL database.
- Stone, B. M., Jordaan, I. J., Xiao, J., & Jones, S. J. (1997). Experiments on the damage process in ice under compressive states of stress. *Journal of Glaciology*, 43(143), 11–25. <https://doi.org/10.1017/S002214300000277X>
- Szabo, D., & Schneebeli, M. (2007). Subsecond sintering of ice. *Applied Physics Letters*, 90(15), 151916. <https://doi.org/10.1063/1.2721391>
- Takeuchi, T., & Saeki, H. (1995). Indentation pressure in ice/vertical structure interaction. *International Journal of Offshore and Polar Engineering*, 5(4), 279–285.
- Takeuchi, T., Sakai, M., Akagawa, S., Nakazawa, N., & Saeki, H. (2001). On the factors influencing the scaling of ice forces. In J. P. Dempsey & H. H. Shen (Eds.), *Proceedings of the iutam symposium on scaling laws in ice mechanics and ice dynamics* (pp. 149–160). IUTAM.
- Taylor, R. S., Richard, M., & Hossain, R. (2019). A probabilistic high-pressure zone model for local and global loads during ice-structure interactions. *Journal of Offshore Mechanics and Arctic Engineering*, 141(5), 1–10. <https://doi.org/10.1115/1.4042386>
- Thorsteinsson, T., Kipfstuhl, J., & Miller, H. (1997). Textures and fabrics in the GRIP ice core. *Journal of Geophysical Research: Oceans*, 102(C12), 26583–26599. <https://doi.org/10.1029/97JC00161>
- Tikanmäki, M., & Heinonen, J. (2022). Estimating extreme level ice and ridge thickness for offshore wind turbine design: Case study Kriegers Flak. *Wind Energy*, 25(4), 639–659. <https://doi.org/10.1002/we.2690>
- Timco, G. W. (1987). Indentation and penetration of edge-loaded freshwater ice sheets in the brittle range. *Journal of Offshore Mechanics and Arctic Engineering*, 109(3), 287–294. <https://doi.org/10.1115/1.3257022>
- Timco, G. W., & Sudom, D. (2013). Revisiting the Sanderson pressure–area curve: Defining parameters that influence ice pressure. *Cold Regions Science and Technology*, 95, 53–66. <https://doi.org/10.1016/j.coldregions.2013.08.005>
- Timco, G. W., & Weeks, W. F. (2010). A review of the engineering properties of sea ice. *Cold Regions Science and Technology*, 60(2), 107–129. <https://doi.org/10.1016/j.coldregions.2009.10.003>
- Toyama, Y., Sensu, T., Minami, M., & Yashima, N. (1983). Model tests on ice-induced self-excited vibration of cylindrical structures. *Proceedings of the International Conference on Port and Ocean Engineering under Arctic Conditions*, 2, 834–844.
- Tsuchiya, M., Kanie, S., Ikejiri, K., Yoshida, A., & Saeki, H. (1985). An experimental study on ice-structure interaction. *Proceedings of the 7th Offshore Technology Conference*, 312–327. <https://doi.org/https://doi.org/10.4043/5055-MS>

- Tuhkuri, J. (1995). Experimental observations of the brittle failure process of ice and ice-structure contact. *Cold Regions Science and Technology*, 23(3), 265–278. [https://doi.org/10.1016/0165-232X\(94\)00018-S](https://doi.org/10.1016/0165-232X(94)00018-S)
- Turner, J. (2018). *Constitutive behaviour of ice under compressive states of stress and its applications to ice-structure interactions* (Doctoral dissertation). Memorial University of Newfoundland.
- van den Berg, M., Owen, C. C., & Hendrikse, H. (2022). Experimental study on ice-structure interaction phenomena of vertically sided structures. *Cold Regions Science and Technology*, 201(June), 103628. <https://doi.org/10.1016/j.coldregions.2022.103628>
- van der Stap, F. L., Nielsen, M. B., Owen, C. C., van der Male, P., & Hendrikse, H. (2023). On the feasibility of monopile foundations for offshore wind in the Baltic Sea. *Proceedings of the 27th International Conference on Port and Ocean Engineering under Arctic Conditions*, 1–15.
- Vihma, T., & Haapala, J. (2009). Geophysics of sea ice in the Baltic Sea: A review. *Progress in Oceanography*, 80(3-4), 129–148. <https://doi.org/10.1016/j.pocean.2009.02.002>
- Wachter, L. M., Renshaw, C. E., & Schulson, E. M. (2009). Transition in brittle failure mode in ice under low confinement. *Acta Materialia*, 57(2), 345–355. <https://doi.org/10.1016/j.actamat.2008.09.021>
- Weeks, W. F., & Hamilton, W. L. (1962). Petrographic characteristics of young sea ice, point barrow, Alaska. *American Mineralogist*, 47(7-8), 945–961.
- Weeks, W., & Hibler III, W. (2010). *On sea ice*. University of Alaska Press.
- Wei, M., Polojärvi, A., Cole, D. M., & Prasanna, M. (2020). Strain response and energy dissipation of floating saline ice under cyclic compressive stress. *The Cryosphere*, 14(9), 2849–2867. <https://doi.org/10.5194/tc-14-2849-2020>
- Wei, M., Prasanna, M., Cole, D. M., & Polojärvi, A. (2022). Response of Dry and Floating Saline Ice to Cyclic Compression. *Geophysical Research Letters*, 49(15), 1–10. <https://doi.org/10.1029/2022GL099457>
- Weiss, J. (2019). Ice: the paradigm of wild plasticity. *Philosophical Transactions of the Royal Society A: Mathematical, Physical and Engineering Sciences*, 377(2146), 20180260. <https://doi.org/10.1098/rsta.2018.0260>
- Weiss, J., & Dansereau, V. (2017). Linking scales in sea ice mechanics. *Philosophical Transactions of the Royal Society A: Mathematical, Physical and Engineering Sciences*, 375(20150352), 17. <https://doi.org/10.1098/rsta.2015.0352>
- Wells, J., Jordaan, I., Derradji-Aouat, A., & Taylor, R. (2011). Small-scale laboratory experiments on the indentation failure of polycrystalline ice in compression: Main results and pressure distribution. *Cold Regions Science and Technology*, 65(3), 314–325. <https://doi.org/10.1016/j.coldregions.2010.11.002>
- Wilén, L. A. (2000). A new technique for ice-fabric analysis. *Journal of Glaciology*, 46(152), 129–139. <https://doi.org/10.3189/172756500781833205>
- Wilén, L., Diprinzio, C., Alley, R., & Azuma, N. (2003). Development, principles, and applications of automated ice fabric analyzers. *Microscopy Research and Technique*, 62(1), 2–18. <https://doi.org/10.1002/jemt.10380>

- Wilson, C. J. L., & Peterzell, M. (2011). Evaluating ice fabrics using fabric analyser techniques in Sørsdal Glacier, East Antarctica. *Journal of Glaciology*, 57(205), 881–894. <https://doi.org/10.3189/002214311798043744>
- WindEurope. (2022). Baltic Sea Countries sign declaration for more cooperation in off-shore wind.
- Withalm, M., & Hoffmann, N. P. (2010). Simulation of full-scale ice-structure-interaction by an extended Matlock-model. *Cold Regions Science and Technology*, 60(2), 130–136. <https://doi.org/10.1016/j.coldregions.2009.09.006>
- Wu, H., Chang, K., & Schwarz, J. (1976). Fracture in the compression of columnar gained ice. *Engineering Fracture Mechanics*, 8(2), 365–370. [https://doi.org/10.1016/0013-7944\(76\)90016-3](https://doi.org/10.1016/0013-7944(76)90016-3)
- Wu, T., & Qiu, W. (2019). A dynamic ice-structure interaction model for prediction of ice-induced vibration. *Periodica Polytechnica Civil Engineering*, 63(2), 550–561. <https://doi.org/10.3311/PPci.13080>
- Xu, N., Yue, Q., Guo, F., & Qu, Y. (2011). Mitigation of ice-induced vibrations by adding cones. *International Journal of Offshore and Polar Engineering*, 21(1), 56–60.
- Xu, Y., Hu, Z., Ringsberg, J. W., & Chen, G. (2019a). Nonlinear viscoelastic-plastic material modelling for the behaviour of ice in ice-structure interactions. *Ocean Engineering*, 173(April 2018), 284–297. <https://doi.org/10.1016/j.oceaneng.2018.12.050>
- Xu, Y., Hu, Z., Ringsberg, J. W., Chen, G., & Meng, X. (2019b). An ice material model for assessment of strain rate, temperature and confining pressure effects using finite element method. *Ships and Offshore Structures*, 14(sup1), 34–44. <https://doi.org/10.1080/17445302.2018.1553134>
- Yadegari, S., Turteltaub, S., Suiker, A. S., & Kok, P. J. (2014). Analysis of banded microstructures in multiphase steels assisted by transformation-induced plasticity. *Computational Materials Science*, 84, 339–349. <https://doi.org/10.1016/j.commatsci.2013.12.002>
- Yan, Y., Uotila, P., Huang, K., & Gu, W. (2020). Variability of sea ice area in the Bohai Sea from 1958 to 2015. *Science of The Total Environment*, 709, 136164. <https://doi.org/10.1016/j.scitotenv.2019.136164>
- Yap, K. T. (2011). *Level ice-vertical structure interaction : Steady-state self-excited vibration of structures* (Doctoral dissertation). National University of Singapore.
- Yap, K. T., & Palmer, A. C. (2013). A model test on ice-induced vibrations: Structure response characteristics and scaling of the lock-in phenomenon. *Proceedings of the 22nd International Conference on Port and Ocean Engineering under Arctic Conditions, POAC*, (109), 11.
- Ye, K., Li, C., Yang, Y., Zhang, W., & Xu, Z. (2019). Research on influence of ice-induced vibration on offshore wind turbines. *Journal of Renewable and Sustainable Energy*, 11(3). <https://doi.org/10.1063/1.5079302>
- Yu, B., & Low, Y. M. (2022). A phenomenological model for simulating ice loads on vertical structures incorporating strain rate-dependent stress-strain characteristics. *Applied Mathematical Modelling*, 101, 132–156. <https://doi.org/10.1016/j.apm.2021.07.021>
- Yue, Q., & Bi, X. (2000). Ice-induced jacket structure vibrations in Bohai Sea. *Journal of Cold Regions Engineering*, 14(2), 81–92.

-
- Yue, Q., & Guo, F. (2012). Physical Mechanism of Ice-Induced Self-Excited Vibration. *Journal of Engineering Mechanics*, 138(7), 784–790. [https://doi.org/10.1061/\(ASCE\)EM.1943-7889.0000378](https://doi.org/10.1061/(ASCE)EM.1943-7889.0000378)
- Yue, Q., Zhang, X., Bi, X., & Shi, Z. (2001). Measurements and analysis of ice induced steady state vibration. *Proceedings of the 16th International Conference on Port and Ocean Engineering under Arctic Conditions (POAC'01)*, 413–420.
- Yun, W., & Azuma, N. (1999). A new automatic ice-fabric analyzer which uses image-analysis techniques. *Annals of Glaciology*, 29(100), 155–162. <https://doi.org/10.3189/172756499781821021>
- Zhang, J., Feng, D., & Pang, S. D. (2019). Bulk constitutive law and its importance in cem simulations of ice-structure interaction. *Proceedings of the 25th International Conference on Port and Ocean Engineering under Arctic Conditions, POAC*, 14.
- Zhou, Z., Ma, W., Zhang, S., Mu, Y., Zhao, S., & Li, G. (2016). Yield surface evolution for columnar ice. *Results in Physics*, 6, 851–859. <https://doi.org/10.1016/j.rinp.2016.10.020>
- Ziemer, G. (2021). *Ice-Induced Vibrations of Vertical Structures* (Doctoral dissertation). Technical University of Hamburg. <https://doi.org/https://doi.org/10.15480/882.4018>
- Ziemer, G., & Hinse, P. (2017). Relation of maximum structural velocity and ice drift speed during frequency lock-in. *Proceedings of the 24th International Conference on Port and Ocean Engineering under Arctic Conditions, POAC*, 12.



ACKNOWLEDGEMENTS

I have had the pleasure of meeting many wonderful people over the last six years, many of whom have inspired me to pursue ice research and follow through with the PhD. To begin, I clearly remember the Arctic Offshore Engineering course by Jeroen Hoving sparking my curiosity, adjoined by the alluring course at UNIS on Svalbard. My sojourn to Longyearbyen plus my later meeting at NTNU with Hayo Hendrikse and sit-in on a SAMCoT meeting solidified by determination to study the topic of dynamic ice-structure interaction. Going through my MSc thesis with Hayo and Gesa Ziemer on the IVOS campaign, I realized I needed to better understand ice-induced vibrations to feel any satisfaction. Thus, my MSc thesis period and later researcher position at TU Delft led me to meeting some fellow ice researchers and also lifelong friends.

CEG room 2.83, this was the place was my first home, gezelligheid, in Europe. Francesca Greco, Mamin Masturi, Valentina Vaniushkina, Vagelis Kementzetzidis, and Marco Vergassola, you showed me dedication to your fields of research, proudly mixed with the importance of work-life balance and diversity of perspectives.

Diving into the ice field, SAMCoT, IAHR 2018, POAC 2019, IAHR 2022, and POAC 2023 exposed me to many young, bright-eyed researchers who knew how to publish and to party: Renate van Vliet, Chris Keijdener, Torodd Nord, Sergiy Sukhorukov, Renat Yulmetov, Åse Ervik, Ekaterina Kim, Wenjun Lu, Evgenii Salganik, Ilija Samardzija, Runa Skarbø, Andrii Murdza, Mikko Suominen, Ida Lemström. Moreover, I am grateful to have met very experienced researchers in ice: Sveinung Løset, Bob Frederking, Kari Kolari, Paul Barrette, Dave M. Cole, John Dempsey, and Erland M. Schulson.

In preparation for furnishing the ice laboratory, I sought inspiration and advice from those at Aalto University right before the pandemic struck: Otto Puolakka, Fang Li, Roman Repin, and Mingdong Wei. Your work in the lab guided my interest and placed me on a path that led me to the content of this thesis. I was mesmerized by ice in crossed-polarized light and befuddled by the lack of explanation for the colors I saw, and from that moment on I knew that that was worth investing time in researching.

In the midst of the COVID-19 pandemic, after numerous rescheduling and flight re-booking attempts, the first SHIVER campaign was underway in the summer of 2021. I will never forget the camaraderie and dedication I witnessed during those months in Finland. May we never 'finish' our drinks, or sink our last red solo cup without a proper goodbye first: Nick Ebbens, Tom Willems, and Marnix van den Berg. Many thanks to the ice tank crew who made the research possible during those incredibly long, cold days in the basin: Teemu Päivärinta and Lasse Turja. A special thanks to Elie Quaireau, who volunteered to make thin sections of the model ice for our Data-in-Brief publication.

My first journal publication could not have been possible without the help from researchers at multiple universities. Thanks to Aleksey Shestov for supporting my visit to UNIS to test my method, and for showing me how cool it is to work in Svalbard during the

ice fieldwork course and via your epic drone videos. Janik John, thank you for sharing your clothes for Pride Day in Longyearbyen, and for sharing your thoughts and experiences in the cold rooms. To Knut V. Høyland and Vegard Hornnes, your kindness, generosity, and keen minds keep drawing me back to Norway whenever I think about where to go next. I cannot express enough gratitude for all of your help and support in the cold rooms at both NTNU and UNIS.

My second journal publication was made possible by the technical support of Jeroen Koning and Kees van Beek, and by the laboratory assistance of Anne Lammertsma. I wish to commiserate here with those whom had the chilling experience of spending extended periods of time in the ice laboratory with me at TU Delft: Anne Lammertsma, Yitao Huang, and Laura van Dijke. Foggy glasses, runny noses, and cold extremities punctuated our sentences in the dungeons downstairs when fiddling with the cold. A special thanks goes to Laura van Dijke for translating my propositions into Dutch.

Although not discussed in this dissertation, the second SHIVER test campaign marked a pivotal point in my research. Besides the acceptance of the third journal publication and the initiation of my time with the Finnish bureaucratic labyrinth for the residence permit application, I had the pleasure of seeing the SHIVER campaign to its effective completion. A great many thanks to Laura van Dijke and Jeffrey Hoek for their unerring positivity and commitment to the campaign.

A shout-out to all those whom I met at TU Delft but have since left the Offshore Engineering Section: Dominik Fallais, Tao Lu, Maxim Segeren, Sergio Sánchez Gómez, Antonio Jarquin Laguna, Tim Raaijmakers, Yang Qu, and João Barbosa.

A shout-out to all those at TU Delft in or associated with the Offshore Engineering Section: Marysa Dunant, Pim van der Male, Eliz-Mari Lourens, Oriol Colomé Gené, George Lavidas, Karel van Dalen, Apostolos Tsouvalas, Andrei Metrikine, Mario Martinelli, Timo Molenkamp, Thanasis Tsetas, Peter Meijers, Stas Verichev, Yuriy Kirichek, Yaxi Peng, Matías Alday González, Ponni Maya, Stavros Panagoulas, Julie Atzampou, Rens van Leijden, Jan Modderman, Shagun Agarwal, Avni Jain, Andrei Faragau, and Vaibhav Raghavan. A special thanks goes to Peter Meijers for translating my summary into Dutch.

A shout-out to my new colleagues at Aalto University: Alice Petry, Marek Muchow, Malith Prasanna, Waqas Ahmad, Sid Oksala, Mohammad Izadi, Pauli Lehto, Peixin Sun, Federica Mancini.

I wish to give a big thanks to Arttu Polojärvi for asking me to join him at Aalto University to continue research on ice. You helped me in a difficult moment in my life, and your support and understanding has brought me to the finish line of my PhD. You, Anna, and Auni have given me a feeling of home in Finland for which I am most grateful.

To Tim C. Hammer, my struggle buddy on this journey. I am so glad to have traveled this PhD with you. So many foolish and profound talks were had in CEG room 3.51, many of which helped crystallize my ideas and challenge my intuitions. Seeing you take control of the SHIVER campaign and fighting with resolve to get your papers through publication was admirable and inspirational beyond words. Whether Castles of Burgundy, Terraforming Mars, or any other game, I know you will be ready to play. Whatever happens next, we will meet to continue the board game nights.

Dear doctor Hendrikse, it has been quite the ride. I could not have been luckier to have had a supervisor like you. You have been a teacher, mentor, friend, opponent, and much

more. You have always given me support, guidance, and time, all while juggling industry projects, other PhDs, educational duties, and raising a family. From "puh-zi-shuns" to "shiver," let us see what comes next.

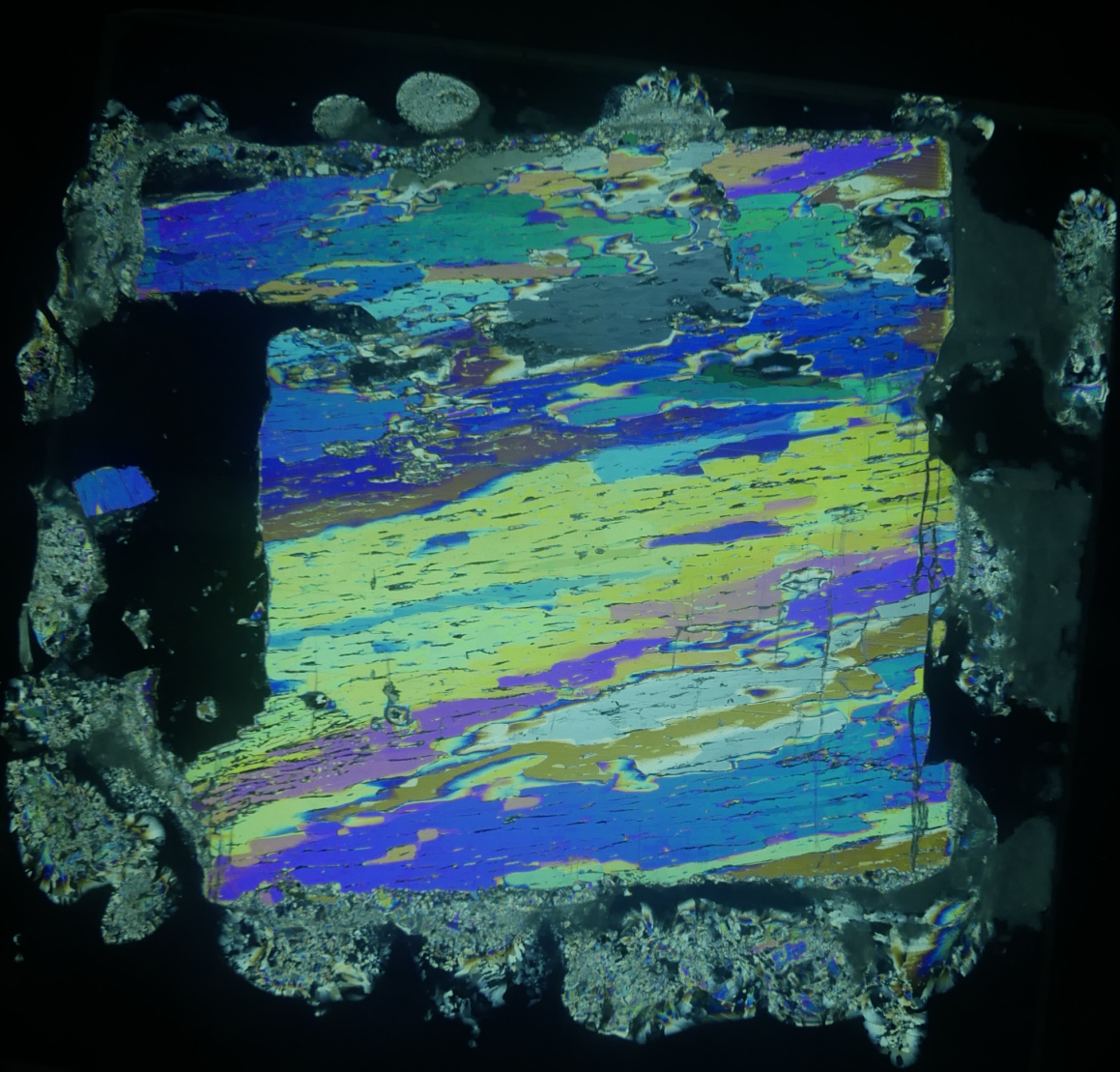
I could have not gotten this far without the love and support from my family. Though many time zones apart, you have always been there for me and welcomed me with open arms when together. To Chris, my brother, thanks for showing me how to be properly nerdy, so uninhibited and pure. To Courtney, my twin and sister, you show incredible resilience, patience, and compassion in your work and with your friends; I aspire to have such heart and courage. To my mother and father, this dissertation has been the summation of all of your hard work and careful parenting. You both have done whatever you could to give me opportunities you never had, and for that I am forever grateful.

Finally, to Bárbara, my partner and my rock. You have supported me through all the ups and downs of the PhD, through all my petulance and impatience. Though I have been living abroad all this time, never have I ever felt more at home than when I am with you. You give me solace, sass, and sweetness that I never thought I deserved. Thank you for everything and more, and I look forward to our future without incessant monologues about ice from my mansplaining mouth.

To the readers who made it this far, I commend you for your zeal.



Progress on all paths,
be it social or scientific.



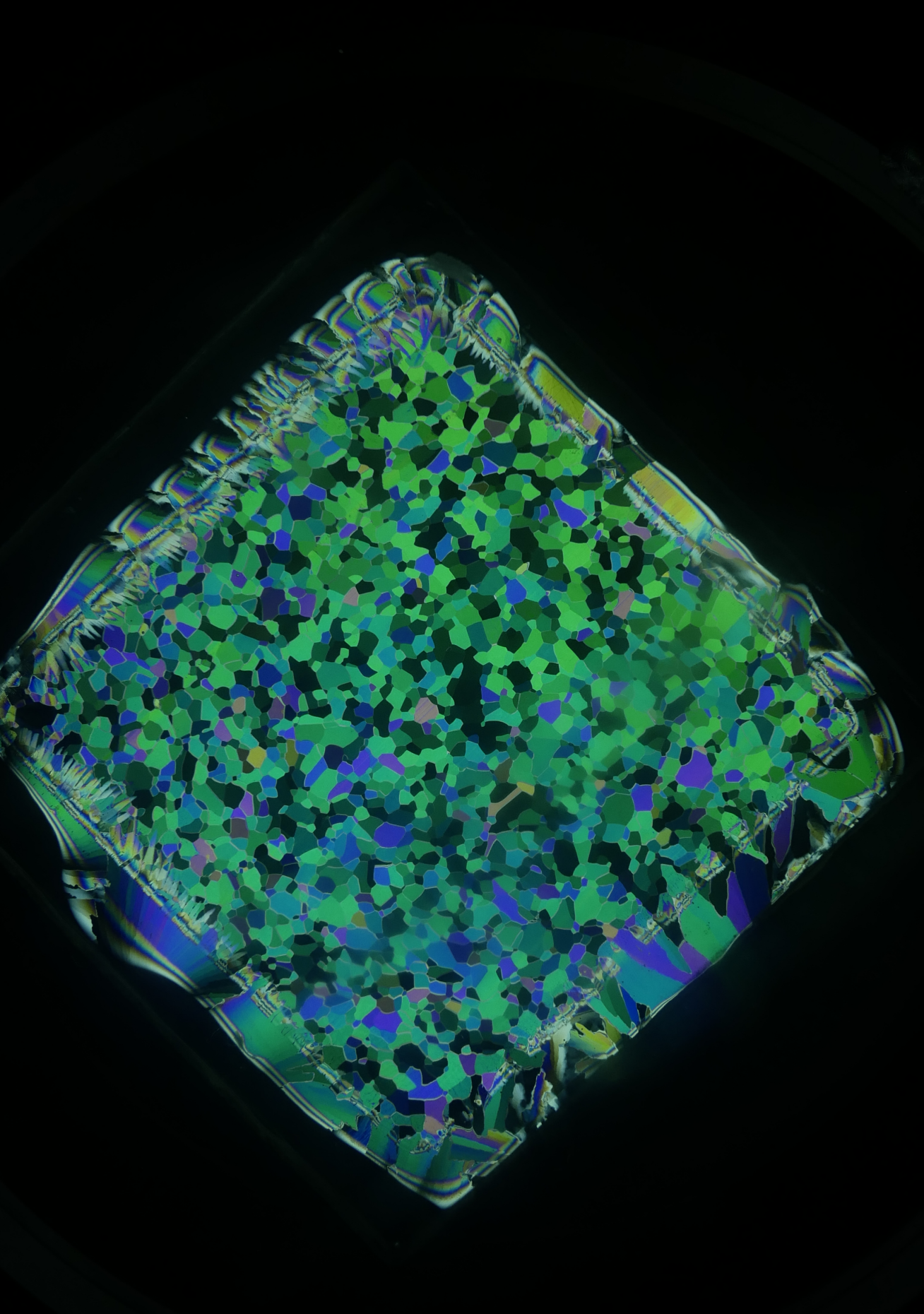
CURRICULUM VITAE

Cody Carlton Owen

13-10-1992 Born in Southampton, New York, United States of America.

EDUCATION

- 2011–2015 Bachelor of Science
Naval Architecture and Marine Engineering
Webb Institute
- 2015–2017 Master of Science
European Wind Energy Master: Offshore Engineering
Offshore and Dredging Engineering
Faculty of Civil Engineering and Geosciences
Delft University of Technology
Wind Energy
Faculty of Information Technology and Electrical Engineering
Norwegian University of Science and Technology
- 2017–2018 Researcher
Dynamic ice-structure interaction
Section of Offshore Engineering
Faculty of Civil Engineering and Geosciences
Delft University of Technology
- 2018–2023 Doctor of Philosophy Research
Ice mechanics in ice-induced vibrations
Section of Offshore Engineering
Faculty of Civil Engineering and Geosciences
Delft University of Technology
- 2023–2024 Postdoctoral Researcher
Ice mechanics in ice-induced vibrations
Marine and Arctic Technology
School of Engineering
Aalto University



LIST OF PUBLICATIONS

JOURNAL PUBLICATIONS

1. **Owen, C. C.**, Hammer, T. C., & Hendrikse, H. (2023b). Peak loads during dynamic ice-structure interaction caused by rapid ice strengthening at near-zero relative velocity. *Cold Regions Science and Technology*, 211(April), 103864. <https://doi.org/10.1016/j.coldregions.2023.103864>
2. **Owen, C. C.**, Hammer, T. C., & Hendrikse, H. (2023a). Hysteresis and dichotomous mechanics in cyclic crushing failure of confined freshwater columnar ice. *Cold Regions Science and Technology*, 209(December 2022), 103816. <https://doi.org/10.1016/j.coldregions.2023.103816>
3. **Owen, C. C.**, & Hendrikse, H. (2023). An initial study of interference coloration for quantifying the texture and fabric of ice. *Cold Regions Science and Technology*, 206, 103735. <https://doi.org/10.1016/j.coldregions.2022.103735>
4. van den Berg, M., **Owen, C. C.**, & Hendrikse, H. (2022). Experimental study on ice-structure interaction phenomena of vertically sided structures. *Cold Regions Science and Technology*, 201(June), 103628. <https://doi.org/10.1016/j.coldregions.2022.103628>
5. Hendrikse, H., Ziemer, G., & **Owen, C. C.** (2018). Experimental validation of a model for prediction of dynamic ice-structure interaction. *Cold Regions Science and Technology*, 151, 345–358. <https://doi.org/10.1016/j.coldregions.2018.04.003>

CONFERENCE PUBLICATIONS

1. van der Stap, F. L., Nielsen, M. B., **Owen, C. C.**, van der Male, P., & Hendrikse, H. (2023). On the feasibility of monopile foundations for offshore wind in the Baltic Sea. *Proceedings of the 27th International Conference on Port and Ocean Engineering under Arctic Conditions*, 1–15
2. Hendrikse, H., & **Owen, C. C.** (2023). Application of the suggested ice strength coefficients in ISO 19906 to intermittent crushing. *Proceedings of the 27th International Conference on Port and Ocean Engineering under Arctic Conditions*, 1–13
3. Hendrikse, H., Hammer, T. C., **Owen, C. C.**, van den Berg, M., van Beek, K., Polojärvi, A., Puolakka, O., & Willems, T. (2022a). Ice Basin Tests for Ice-Induced Vibrations of Offshore Structures in the SHIVER Project. *Proceedings of the ASME 2022 41st International Conference on Ocean, Offshore and Arctic Engineering*, 6, 1–9. <https://doi.org/10.1115/OMAE2022-78507>
4. Hammer, T. C., **Owen, C. C.**, van den Berg, M., & Hendrikse, H. (2022). Classification of Ice-Induced Vibration Regimes of Offshore Wind Turbines. *Proceedings of the ASME 2022 41st International Conference on Ocean, Offshore and Arctic Engineering*, 6, 1–8. <https://doi.org/10.1115/OMAE2022-78972>
5. **Owen, C. C.**, Hammer, T. C., & Hendrikse, H. (2022). Test setup for compressive loading of confined ice thick sections viewed with in-situ cross-polarization imaging. *Proceedings of the 26th IAHR International Symposium on Ice*, (June), 1–10

6. **Owen, C. C., & Hendrikse, H. (2021).** Simulation and analysis of ice-induced vibrations experienced by Molikpaq during the May 12, 1986 event. *Proceedings of the 26th International Conference on Port and Ocean Engineering under Arctic Conditions, POAC, 2021-June*, 1–14
7. **Owen, C. C., & Hendrikse, H. (2019).** A study of the transition ice speed from intermittent crushing to frequency lock-in vibrations based on model-scale experiments. *Proceedings of the 25th International Conference on Port and Ocean Engineering under Arctic Conditions*, 13
8. **Owen, C. C., & Hendrikse, H. (2018).** Ice-induced vibrations of model structures with various dynamic properties. *Proceedings of the 24th IAHR International Symposium on Ice*, 376–385